Available online at www.sciencedirect.com
ScienceDirect
Comput. Methods Appl. Mech. Engrg. 407 (2023) 115913
Computer methods in applied mechanics and engineering
www.elsevier.com/locate/cma

Multiscale modeling of prismatic heterogeneous structures based on a localized hyperreduced-order method

A. Giuliodori[a,b], J.A. Hernández[a,c,*], E. Soudah[a,b,d]

[a] *Centre Internacional de Mètodes Numèrics en Enginyeria (CIMNE), Barcelona, Spain*
[b] *Universitat Politècnica de Catalunya, UPC, Barcelona, Spain*
[c] *E.S. d'Enginyeries Industrial, Aeroespacial i Audiovisual de Terrassa, Technical University of Catalonia, C/ Colom, 11, Terrassa 08222, Spain*
[d] *Mechanical Engineering Department, Faculty of Industrial Engineering of the University of Valladolid, 47011 Valladolid, Spain*

Received 17 October 2022; received in revised form 19 January 2023; accepted 19 January 2023
Available online 9 February 2023

Abstract

This work aims at deriving special types of one-dimensional Finite Elements (1D FE) for efficiently modeling heterogeneous prismatic structures, in the small strains regime, by means of reduced-order modeling (ROM) and domain decomposition techniques. The employed partitioning framework introduces "fictitious" interfaces between contiguous subdomains, leading to a formulation with both subdomain and interface fields. We propose a low-dimensional parameterization at both subdomain and interface levels by using reduced-order bases precomputed in an offline stage by applying the Singular Value Decomposition (SVD) on solution snapshots. In this parameterization, the amplitude of the fictitious interfaces play the role of coarse-scale displacement unknowns. We demonstrate that, with this partitioned framework, it is possible to arrive at a solution strategy that avoids solving the typical nested local/global problem of other similar methods (such as the FE^2 method). Rather, in our approach, the coarse-grid cells can be regarded as special types of finite elements, whose nodes coincides with the centroids of the interfaces, and whose kinematics are dictated by the modes of the "fictitious" interfaces. This means that the kinematics of our coarse-scale FE are not pre-defined by the user, but extracted from the set of "training" computational experiments. Likewise, we demonstrate that the coarse-scale and fine-scale displacements are related by inter-scale operators that can be precomputed in the offline stage. Lastly, a hyperreduced scheme is considered for the evaluation of the internal forces, allowing us to deal with possible material nonlinearities.

Keywords: Multiscale method; Reduced-order modeling; Localized model order reduction; Singular value decomposition; Domain decomposition; Finite element analysis

1. Introduction

It is well known that discretization techniques for partial differential equations (PDE) of complex systems frequently lead to very high-dimensional numerical models with corresponding high demands concerning hardware and computation times. This holds particularly in problems with complex geometries and nonlinear behaviors, where the system of equations to be solved often includes a large number of degrees of freedom (DOFs). Many strategies

* Corresponding author.
E-mail address: jhortega@cimne.upc.edu (J.A. Hernández).

https://doi.org/10.1016/j.cma.2023.115913

have been developed to tackle this issue, allowing us to reduce the number of DOFs of the full-order model with a lower-dimensional representation, whose accuracy must be carefully considered. The particular field of ROM encompasses a broad set of mathematical methods that allow us to generate and evaluate these simplified models [1]. It is worth mentioning that one precedent to this field may be found in the low-dimensional parameterization of systems based on analytical deductions, in which one introduces simplifying assumptions on the system behavior to facilitate its treatment. An illustrative example in this respect is that of classical beam theory, which assumes that cross-sections of a prismatic beam remain planar after deformation, and by doing so, the displacement field of such cross-sections become parameterized in terms of three translations and three rotations. Unfortunately, most engineering problems are not amenable to empirical models or derivations based on first-principles. Consequently, other approaches are used for addressing more complex systems, typically high-dimensional, with underlying dominant patterns that should be properly characterized.

In this regard, one of the most popular approaches is projection-based ROM, which basically restricts the solution space to a smaller subspace spanned by a precomputed reduced-order basis. A widely used method to construct this basis is the Proper Orthogonal Decomposition (POD), firstly introduced in the statistical and turbulence research area [2,3]. POD is based on snapshots of the response of the system of interest, and therefore, it requires accumulating solutions of problems (sampling the input parameter space) using the high-fidelity model [4], during a so-called offline stage. Then, the most statistically dominant patterns of these snapshots are identified by the SVD, obtaining a reduced-order basis that minimizes the projection error of the snapshots [5]. The governing equations are then projected onto the subspace spanned by this reduced-order basis, obtaining a system with far fewer equations than the original one. However, especially for high-dimensional and multiscale problems, projection-based ROM exhibits certain limitations, such as offline high-computational cost, no topological flexibility, and dependency on a large number of input parameters [6]. In this sense, since one cannot afford creating a new reduced model for every change in the parameter values, the desired approach is to generate a parametric reduced model that approximates the original one with high fidelity over a range of parameters [1].

Localized model order reduction methods overcome or significantly mitigate these limitations, exhibiting more flexibility than standard ROM, where the topology of the geometry is fixed. The strategy consists in combining approaches from ROM and domain decomposition with the purpose of building distinct reduced spaces in different parts of the computational domain, and then, accommodating (local) changes of the geometry and the PDE in the online stage [6]. On the one hand, the spatial domain under study is decomposed into substructures, with the aim of splitting the global system of equations into smaller (local) systems (see, e.g. [7,8]). On the other hand, ROM techniques allow us to build local reduced spaces that have only support on each subdomain. Thus, by combining these approaches, one can compute a global approximation (within certain accuracy) by means of a effective coupling of the local spaces [6], achieved by enforcing continuity requirements between adjacent subdomains. Localized ROM was firstly introduced in the context of dynamic analyses with the "Component Mode Synthesis" [9,10], and then it was also applied to a wide range of problems, such as in elastostatics [11–13] and multi-body systems [14,15], among others (see, e.g [16–18]). All these methods have proven that localized ROM offers a effective approach for solving parameterized PDE of high-dimensional systems. Nevertheless, we have to take into account the additional costs and effort of incorporating the coupling conditions that ensure the continuity of the solutions at the interfaces [17]. Indeed, the distinct treatments of this critical issue is what characterizes each different method.

Localized ROM has been further combined with multiscale modeling approaches, enabling the approximation of the solution of problems with complex heterogeneities and large domains. Multiscale problems are usually addressed by hierarchical approaches, where for each material point on the coarse scale, a fine scale Boundary Value Problem (BVP) is solved on a Representative Volume Element (RVE) (or unit cell, for periodic structures) in order to obtain the homogenized macroscopic response. In the specific context of two-scale homogenization, the approximation of the (computationally expensive) fine-scale solutions by projection-based methods has already been explored by several authors (see, e.g. [19–21]). Beyond scale separation, more general hierarchical multiscale techniques have been proposed, such as the multiscale finite element method [22], the localized reduced basis multiscale method [23], the heterogeneous multiscale method [24,25], and the Generalized Multiscale FEM (GMsFEM) [26]. All these methods attempt to approximate the global solution by coupling local (coarse-grid) solutions, which are sought in low-dimensional spaces that reflect (fine-grid) structures in a way consistent with the local property of the differential operator [22]. However, all these methods need to integrate the resulting reduced-order equations in all the fine-grid

integration points, leading to approaches that are only suitable to address BVPs that bear an affine relation with the coarse-grid input parameter (such as the case of linear elasticity, in which the reduced stiffness matrix can be precomputed in the offline stage).

The method proposed in the present work belongs in the same class as the aforementioned general multiscale approaches, but it presents some distinctive features which are described in what follows. Most of these features are generalizations, to the case of general partitions, of the ideas proposed by the second author in Ref. [27] for the particular case of periodic structures. Firstly, the chosen partitioning framework is the Localized Lagrange Multiplier (LLM) method, originally proposed in Ref. [28], which introduces "fictitious" interfaces between contiguous subdomains, whose displacements are assumed independent to the substructures. This partitioning scheme allows us to indirectly enforce continuity conditions between adjacent subdomains, through the fictitious interfaces with the use of localized Lagrange multipliers (for a better understanding of this approach we refer the reader to the works of Park et al. in [28,29]). This partitioning scheme leads to a three-field formulation in terms of subdomain displacements, subdomain reactions and interface displacements. As proposed in Ref. [27], we shall approximate these variables as linear combinations of reduced sets of dominant modes (i.e. reduced-order bases), which are precomputed by applying the SVD over a battery of full-order FE solutions (snapshots) at selected values of the input parameter. Governing equations defined at the subdomain level are, as customary, projected onto the low-dimensional subspaces spanned by these bases. Our multiscale model is then built by assigning a coarse-grid cell to each subdomain, and by splitting the problem unknowns between local and global variables: local variables are defined at the fine-grid subdomain level and global variables are those related to the interfaces, which in turn define our coarse grid. One important ingredient of our method is that element-wise Gauss integration of reduced internal forces is replaced by an efficient integration rule, obtained by means of the Empirical Cubature Method (ECM) [27,30], which selects a subset of integration points among all the fine-grid Gauss points of the subdomain. This efficient integration rule is tailored to the physics of the cell problem, and it can be regarded as a second step of reduction (hence the name "hyperreduction") of the (possibly nonlinear) internal force term in the subdomains equilibrium equation. It should be remarked that, thanks to this hyperreduction step, the overall computational cost of the method depends only on the number of subdomains in the partition as well as the number of reduced integration points (yet not on the complexity of the underlying finite element discretization of each subdomain).

Another remarkable feature of the proposed approach is that, in order to avoid having to solve the nested local/global problems (characteristic of most multiscale approaches), we introduce constraints in the construction of our coarse-scale model in such a way that all subdomain variables can be expressed in terms of interface variables. This particular feature results in a coarse-scale equilibrium equation posed solely in terms of interface variables, or, stated another way, we replace the standard hierarchical approach by an inter-scale strategy, in which the displacements of the interfaces are the only primary unknowns (more specifically, the amplitude of the displacement modes of such interfaces). As a consequence of using this inter-scale approach, our methodology can be easily implemented in a FE package, since the coarse-grid cells can be regarded as special types of finite elements, whose nodes coincides with the centroids of the interfaces, and which have associated inter-scale operators (e.g. shape functions) accounting for the influence of the underlying subdomain. Note that these particular inter-scale operators are built based on computational experiments performed in the offline stage.

The generalization to the case of general partitions (including non-periodic cases) implies that, for each distinct cell, a reduced-order basis should be computed based on a set of snapshots that includes information about the specific cell configuration. Consequently, the offline computational cost increases with the number of distinct subdomains in the partition. In order to overcome this issue, we propose here a strategy aimed at dealing with many different cell configurations at a reasonable computational cost. Firstly, in this strategy, the training structures (i.e. geometries to be used in the training tests built by an arrangement of cells) may be designed taking into account combinations of distinct cells, so that we can extract patterns of deformation for many subdomains using a few number of training tests. Secondly, we propose to leverage the manifold interpolation scheme advocated by Amsallem et al. in Ref. [31]; this scheme will allow us to adapt the precomputed reduced-order bases to changes in physical/modeling parameters. This strategy is particularly useful in cases in which the subdomains are amenable to geometric parameterization. In such cases, we can build parametric reduced-order bases for a subset of cells, and then, interpolate for new configurations, allowing us to enlarge our library of reduced bases without the need of testing each distinct subdomain.

The computational cost invested in the offline stage is amply repaid by the low computational cost associated to the online stage. Indeed, the key feature of using a localized ROM is that we can build many different coarse-scale

models by combining the cells in diverse geometrical configurations, and rapidly analyze them under different boundary conditions and external loads.

As mentioned at the outset, the scope of the proposed strategy is limited to the case of subdomains with two interface boundaries. If the structure is prismatic, and the partition is made by planes normal to the midlines (so that the subdomains are "slices"), then the resulting coarse-scale model is akin to that of classical FE structural beam theories, in which the DOFs of the nodes encapsulate the displacements of the interfaces. The simplest model arising from this conceptualization is that in which the interfaces do not experience deformation, just rigid-body motions (6 DOFs for each interface/node) as in standard beam theories. However, the proposed coarse-scale may have more than 6 DOFs, depending on the complexity of the cross-section, and on the training data. From this perspective, the proposed approach may be regarded as a machine learning tool for deriving special types of one-dimensional FE (two-nodes FE), representing the underlying two-interface cells, whose customized kinematics are based on the deformational patterns of the subdomains sharing the interface. It should be noted, however, that the analysis of prismatic structures by means of cross-sectional modes is not new, and within this context, our approach bears some resemblance to the Generalized Beam Theory (GBT) [32], which has been extensively used for the buckling analysis of open-sectional unbranched thin-walled members. However, as opposed to our approach, the GBT is based on the computation of these modes in an analytical fashion, and besides, it does not offer the possibility of combining slices with different cross-sectional modes.

1.1. Organization of the paper

The remainder of the paper is organized as follows. Section 2 introduces the employed domain decomposition framework, describing the geometric setup and the fine-scale variables. Section 3 presents the parameterized variational principle, as well as the corresponding governing equations. Section 4 describes the offline training stage briefly, while Section 5 explains how to obtain the subdomain coarse-scale variables from the modal expansion of their fine-scale counterparts. Section 6 is concerned with the low-dimensional approximation of fictitious interface displacements and related well-posedness considerations. Section 7 thoroughly describes the coarse-scale model, including details on the construction of many coarse-scale and inter-scale operators. Finally, in Sections 8, 9, and 10, we present the numerical evaluation of the proposed methodology. Section 8 presents a consistency analysis performed on 2 distinct prismatic structures. Section 9, on the other hand, is concerned with the derivation of *characteristic* coarse-scale elements (which solely accounts for the transmission of loads through the subdomain, ignoring any local effect). In the first case, a rectangular cross-section beam is analyzed, and then, the derived coarse-scale element is compared against Timoshenko-based beam element. In the second case, we derive a coarse-scale element for a U-shaped cross-section beam, and then we test the performance in unseen scenarios (namely, a longer structure with different boundary conditions). We conclude the numerical assessment in Section 10, applying the methodology to two cases featuring heterogeneous composition, cross-section changes and curved midlines. In the first case, we build a coarse-scale model for a fiber-reinforced tubular structure with 3 *characteristic* subdomains, while in the second case we analyze a helical structure with variable cross-section, deriving 10 *characteristic* coarse-scale elements. All the test cases are compared against FE solutions, measuring the accuracy and computational cost reduction.

2. Geometric setup

2.1. Coarse and fine partitions

Let $\Omega \subset \mathbb{R}^3$ be the domain occupied by a given body, with boundary $\partial\Omega$, and consider two nested partitions of Ω, referred to as *coarse* and *fine* partitions. The *coarse partition* is formed by M non-overlapping subdomains $\Omega^1, \Omega^2 \dots \Omega^M$ such that each subdomain is in contact with either one or two subdomains, and, furthermore, the interface boundaries are planar and do not intersect with each other. For practical purposes, Ω may be thought of as a curved beam of varying cross-section, and the subdomains as slices arising from cutting out the beam by planes along its axis, as illustrated in Fig. 1 (although it should be stressed that the approach is general and does not presuppose any constraint in the shape and size of the subdomains). For convenience, we assume that the ends of the beam are interface boundaries as well, so that all subdomains have 2 interface boundaries (denoted by $\partial\Omega_1^e$ and

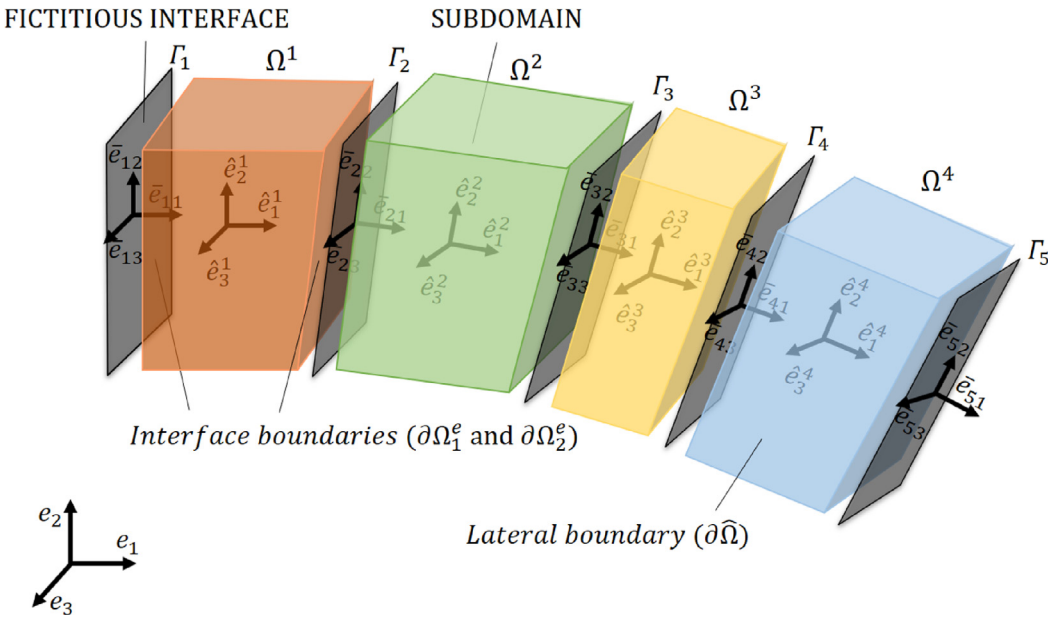

Fig. 1. Prismatic domain decomposed following the Localized Lagrange Multiplier method, in which fictitious interfaces between contiguous slices are introduced for imposing continuity conditions. Graphical description of global and local reference systems for both fictitious interfaces Γ_I $(I = 1, 2, 3, 4, 5)$ and subdomains Ω^e $(e = 1, 2, 3, 4)$.

$\partial\Omega_2^e$). The remaining part of the boundary of each subdomain is referred to as *lateral boundary*, and it is denoted by $\partial\hat{\Omega}^e$ $(e = 1, 2 \dots M)$.

We place at the centroid of each subdomain a local reference system defined by the triad of unit orthogonal vectors $\{\hat{\boldsymbol{e}}_1^e, \hat{\boldsymbol{e}}_2^e, \hat{\boldsymbol{e}}_3^e\}$ $(e = 1, 2 \dots M)$. The coordinates of this triad relative to the global reference system $\{\boldsymbol{e}_1, \boldsymbol{e}_2, \boldsymbol{e}_3\}$ are given by the matrix:

$$[\hat{\boldsymbol{Q}}^e]_{ij} = \boldsymbol{e}_i^T \hat{\boldsymbol{e}}_j^e, \qquad i, j = 1, 2, 3, \qquad e = 1, 2 \dots M. \tag{1}$$

We adopt the convention of taking $\hat{\boldsymbol{e}}_1^e$ normal to $\partial\Omega_1^e$, and pointing inwards; $\hat{\boldsymbol{e}}_2^e$ and $\hat{\boldsymbol{e}}_3^e$, on the other hand, may be oriented as the principal axes of $\partial\Omega_1^e$. Unless otherwise stated, in the sequel, all variables defined at subdomain level are expressed in this local reference system.

The *fine partition*, on the other hand, is a FE discretization of each subdomain Ω^e into m^e elements $(e = 1, 2 \dots M)$. The vector of nodal displacements, expressed in the local reference frame of $\partial\Omega^e$, is denoted by $\boldsymbol{d}^e \in \mathbb{R}^{3n^e}$, n^e being the number of nodes of the discretization. We split the list of DOFs of the subdomain Ω^e as

$$\{1, 2 \dots 3n^e\} = \mathbf{f}^e \cup \mathbf{s}^e = \mathbf{f}_1^e \cup \mathbf{f}_2^e \cup \mathbf{s}^e \tag{2}$$

where $\mathbf{f}_1^e$ and $\mathbf{f}_2^e$ stand for the DOFs corresponding to $\partial\Omega_1^e$ and $\partial\Omega_2^e$, respectively, whereas $\mathbf{s}^e$ represents the remaining DOFs. The corresponding partition of the vector of nodal displacements reads

$$\boldsymbol{d}^e = \begin{bmatrix} \mathbb{F}^e \boldsymbol{d}^e \\ \mathbb{S}^e \boldsymbol{d}^e \end{bmatrix} = \begin{bmatrix} \boldsymbol{d}_{\mathbf{f}}^e \\ \boldsymbol{d}_{\mathbf{s}}^e \end{bmatrix} = \begin{bmatrix} \boldsymbol{d}_{\mathbf{f}_1}^e \\ \boldsymbol{d}_{\mathbf{f}_2}^e \\ \boldsymbol{d}_{\mathbf{s}}^e \end{bmatrix}. \tag{3}$$

where $\boldsymbol{d}_{\mathbf{f}_1}^e = \mathbb{F}_1^e \boldsymbol{d}^e \in \mathbb{R}^{3l_1^e}$ and $\boldsymbol{d}_{\mathbf{f}_2}^e = \mathbb{F}_2^e \boldsymbol{d}^e \in \mathbb{R}^{3l_2^e}$ are the interface boundary displacements of $\partial\Omega_1^e$ and $\partial\Omega_2^e$, respectively (and $\mathbb{F}_1^e$ and $\mathbb{F}_2^e$ the corresponding Boolean restriction operators). This partition of nodal displacements of the domain is illustrated in Fig. 2a.

The vector of nodal interface forces of subdomain Ω^e is denoted by $\boldsymbol{\lambda}^e$. For convenience in the formulation, we define it at all the nodes of the fine mesh of subdomain Ω^e (thus $\boldsymbol{\lambda}^e \in \mathbb{R}^{3n^e}$), yet it will be only nonzero at the

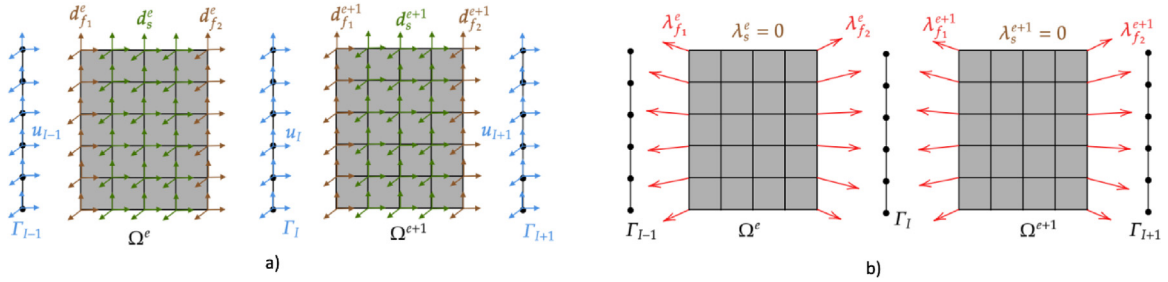

Fig. 2. Fine-scale nodal variables employed by the *Localized Lagrange Multiplier* method. (a) Displacement vectors (for the subdomains, partitioned as indicated in Eq. (3), and for the fictious interfaces, see Eq. (6)). (b) Interface force vector (Lagrange multipliers) for the subdomains (partitioned as indicated in Eq. (4)).

entries corresponding to $\partial\Omega_1^e$ and $\partial\Omega_2^e$, i.e.:

$$\boldsymbol{\lambda}^e = \begin{bmatrix} \boldsymbol{\lambda}_{\mathbf{f}}^e \\ \boldsymbol{\lambda}_{\mathbf{s}}^e \end{bmatrix} = \begin{bmatrix} \boldsymbol{\lambda}_{\mathbf{f_1}}^e \\ \boldsymbol{\lambda}_{\mathbf{f_2}}^e \\ \boldsymbol{\lambda}_{\mathbf{s}}^e \end{bmatrix}, \qquad \text{where } \boldsymbol{\lambda}_{\mathbf{s}}^e = \mathbf{0} \tag{4}$$

(see Fig. 2b).

2.2. Fictitious interfaces

Interface conditions between adjacent subdomains are not established directly but through N *fictitious interfaces* $\Gamma_1, \Gamma_2 \dots \Gamma_N$. Boundary conditions at the ends of the beam are also established through these fictitious interfaces (thus $N = M + 1$). The position of the fictitious interfaces coincides with the position of the interface boundaries of the corresponding subdomains in the undeformed configuration (yet not necessarily after the deformation). The connectivity information is provided by a $M \times 2$ connectivity array $\boldsymbol{\mathcal{T}}$, so that if $I = \boldsymbol{\mathcal{T}}(e,k)$, then $\Gamma_I = \partial\Omega_k^e$. We shall assume that the meshes of contiguous subdomains are conforming, and make therefore the discretization of the corresponding fictitious interface coincident with both meshes (and with the same order of interpolation).

We attach a local coordinate system $\{\bar{\boldsymbol{e}}_{\boldsymbol{I1}}, \bar{\boldsymbol{e}}_{\boldsymbol{I2}}, \bar{\boldsymbol{e}}_{\boldsymbol{I3}}\}$ to the centroid of each fictitious interface Γ_I ($I = 1, 2 \dots N$). If $\Gamma_I = \partial\Omega_1^e$ for some $e \in \{1, 2 \dots M\}$, we align $\{\bar{\boldsymbol{e}}_{\boldsymbol{I1}}, \bar{\boldsymbol{e}}_{\boldsymbol{I2}}, \bar{\boldsymbol{e}}_{\boldsymbol{I3}}\}$ with the corresponding subdomain reference system $\{\hat{\boldsymbol{e}}_{\mathbf{1}}^{\boldsymbol{e}}, \hat{\boldsymbol{e}}_{\mathbf{2}}^{\boldsymbol{e}}, \hat{\boldsymbol{e}}_{\mathbf{3}}^{\boldsymbol{e}}\}$; otherwise, we make $\bar{\boldsymbol{e}}_{\boldsymbol{I1}}$ normal to $\partial\Omega_2^e$ pointing outwards, and orient the tangential vectors $\bar{\boldsymbol{e}}_{\boldsymbol{I2}}$ and $\bar{\boldsymbol{e}}_{\boldsymbol{I3}}$ as the principal axes of $\partial\Omega_2^e$. The coordinates of the interface triad of $\Gamma_I = \partial\Omega_k^e$ in the reference system of Ω^e are stored in the matrix

$$[\boldsymbol{Q}_k^e]_{ij} = \hat{\boldsymbol{e}}_{\boldsymbol{i}}^{\boldsymbol{e}T} \bar{\boldsymbol{e}}_{\boldsymbol{Ij}}, \qquad i, j = 1, 2, 3, \qquad I = \boldsymbol{\mathcal{T}}(e,k). \tag{5}$$

Note that, according to the convention adopted above, $\boldsymbol{Q}_1^e = \boldsymbol{I}$ ($e = 1, 2 \dots M$), $\boldsymbol{I} \in \mathbb{R}^{3\times3}$ being the identity matrix.

We denote by $\boldsymbol{u}_I \in \mathbb{R}^{3l_I}$ the vector of nodal displacements for interface Γ_I (see Fig. 2a), expressed in this case in the reference system of the interface. Likewise, we write the displacement of the fictitious interfaces associated to subdomain Ω^e as

$$\boldsymbol{u}^e := \begin{bmatrix} \boldsymbol{u}_1^e \\ \boldsymbol{u}_2^e \end{bmatrix} = \begin{bmatrix} \boldsymbol{u}_I \\ \boldsymbol{u}_J \end{bmatrix}, \quad \text{where} \quad I = \boldsymbol{\mathcal{T}}(e,1), \quad J = \boldsymbol{\mathcal{T}}(e,2), \quad e = 1, 2 \dots M. \tag{6}$$

Displacements of fictitious interfaces are assumed independent of the associated subdomain displacements; the gap between both variables for a given subdomain Ω^e can be compactly expressed as

$$\Delta\boldsymbol{u}^e = \boldsymbol{d}_{\mathbf{f}}^e - \boldsymbol{D}^e \boldsymbol{u}^e \tag{7}$$

where

$$\boldsymbol{D}^e = \begin{bmatrix} \boldsymbol{D}_1^e & \mathbf{0} \\ \mathbf{0} & \boldsymbol{D}_2^e \end{bmatrix} := \begin{bmatrix} \mathbb{D}_1^e & \mathbf{0} \\ \mathbf{0} & \boldsymbol{\mathcal{Q}}_2^e \mathbb{D}_2^e \end{bmatrix}. \tag{8}$$

Here $\boldsymbol{\mathcal{Q}}_2^e \in \mathbb{R}^{3l_l \times 3l_l}$ is a block diagonal matrix containing l_2^e repetitions of the rotation matrix defined in Eq. (5):

$$\boldsymbol{\mathcal{Q}}_2^e = \text{diag}\,(\boldsymbol{Q}_2^e, \boldsymbol{Q}_2^e, \cdots, \boldsymbol{Q}_2^e), \qquad e = 1, 2 \ldots M; \tag{9}$$

whereas $\mathbb{D}_k^e$ denotes the connection matrix relating the displacements of Γ_I and $\partial\Omega_k^e$. Notice that, as we have assumed that the meshes are conforming, $\mathbb{D}_k^e$ will be a square Boolean matrix.

3. Parameterized variational principle

Consider the following parameterization of surface tractions, body forces and imposed displacements in terms of a set of parameters $\boldsymbol{\mu} \in \mathcal{D} \subset \mathbb{R}^{d_\mu}$:

$$\hat{\boldsymbol{t}}^e\colon \partial\hat{\Omega}^e \times \mathcal{D} \to \mathbb{R}^3, \qquad \boldsymbol{b}^e\colon \Omega^e \times \mathcal{D} \to \mathbb{R}^3, \qquad e = 1, 2 \ldots M \tag{10}$$

$$\bar{\boldsymbol{t}}_I\colon \Gamma_I \times \mathcal{D} \to \mathbb{R}^3, \qquad \bar{\boldsymbol{v}}_K\colon \Gamma_K \times \mathcal{D} \to \mathbb{R}^3, \qquad I \in \boldsymbol{j_l}, \quad K \in \boldsymbol{j_r}. \tag{11}$$

Here $\boldsymbol{b}^e$ represents body forces per unit volume acting on Ω^e, whereas $\hat{\boldsymbol{t}}^e$ are the surface tractions applied on the lateral surface $\partial\hat{\Omega}^e$ ($e = 1, 2 \ldots M$). On the other hand, the mappings defined in Eq. (11) are the boundary conditions[1] on Γ_I ($I \in \boldsymbol{j}$), $\boldsymbol{j}$ being the indexes of the end interfaces[2]; more specifically, $\bar{\boldsymbol{v}}_K$ is the prescribed displacement on Γ_K ($K \in \boldsymbol{j_r} \subseteq \boldsymbol{j}$), whereas $\bar{\boldsymbol{t}}_I$ designates the surface tractions on Γ_I ($I \in \boldsymbol{j_l} \subseteq \boldsymbol{j}$). Both $\bar{\boldsymbol{v}}_K$ and $\bar{\boldsymbol{t}}_I$ are expressed in the local reference frame of each interface. Notice that if $\boldsymbol{j_r} = \boldsymbol{j}$, that is, if displacements are prescribed on both ends, then $\boldsymbol{j_l}$ is empty.

Our goal is to derive a hyperreduced-order model (HROM) able to determine the nodal displacements $\boldsymbol{d}^e$ of each subdomain Ω^e ($e = 1, 2 \ldots M$), as well as other related fine-scale variables, for any value of the input parameter $\boldsymbol{\mu} \in \mathcal{D}$. We shall assume that displacements and strains are small, that loads are applied in a quasi-static manner, yet we place no constraints on the constitutive behavior of the material(s). If the constitutive model(s) are nonlinear, the pseudo-time is included in the set of parameters $\boldsymbol{\mu}$.

Following the approach advocated by the second author in Ref. [27] for periodic structures, we shall derive the desired reduced-order equations from the stationary conditions of the following three-field energy functional:

$$\Pi = \sum_{e=1}^{M} \left(\Pi_{int}^e(\boldsymbol{d}^e) - \Pi_{ext}^e(\boldsymbol{d}^e, \boldsymbol{b}^e, \hat{\boldsymbol{t}}^e) - \pi^e(\boldsymbol{d}^e, \boldsymbol{u}^e, \boldsymbol{\lambda}^e) \right) - \sum_{I \in \boldsymbol{j_l}} \bar{\Pi}_I(\boldsymbol{u}_I, \bar{\boldsymbol{t}}_I). \tag{12}$$

Here, Π_{int}^e stands for the strain energy term, Π_{ext}^e denotes the contribution due to the work done by body forces and surface tractions acting on the lateral surface (for each subdomain Ω^e, $e = 1, 2 \ldots M$), whereas $\bar{\Pi}_I$ ($I \in \boldsymbol{j_l}$) is the part due to surface tractions acting on the end interfaces . The term π^e, on the other hand, is the interface or *dislocation potential* of subdomain Ω^e, defined as the work done by the interaction forces $\boldsymbol{\lambda}_{\mathbf{f}}^e$ over the interface gap introduced in Eq. (7), i.e.:

$$\pi^e = \boldsymbol{\lambda}_{\mathbf{f}}^{eT} (\boldsymbol{d}_{\mathbf{f}}^e - \boldsymbol{D}^e \boldsymbol{u}^e), \qquad e = 1, 2 \ldots M. \tag{13}$$

The stationary condition of Eq. (12) gives

$$\delta\Pi = \sum_{e=1}^{M} \left(\delta\Pi_{int}^e - \delta\Pi_{ext}^e - \delta\pi^e \right) - \sum_{I \in \boldsymbol{j_l}} \delta\bar{\Pi}_I = 0, \tag{14}$$

where

$$\delta\Pi_{int}^e = \delta\boldsymbol{d}^{eT} \boldsymbol{F}_{int}^e, \qquad e = 1, 2 \ldots M \tag{15}$$

$$\delta\Pi_{ext}^e = \delta\boldsymbol{d}^{eT} \boldsymbol{F}_{ext}^e, \qquad e = 1, 2 \ldots M \tag{16}$$

$$\delta\bar{\Pi}_I = \delta\boldsymbol{u}_I^T \bar{\boldsymbol{F}}_I, \qquad I \in \boldsymbol{j_l}. \tag{17}$$

Here, $\boldsymbol{F}_{int}^e \in \mathbb{R}^{3n^e}$ and $\boldsymbol{F}_{ext}^e \in \mathbb{R}^{3n^e}$ are the FE nodal vectors of internal and external forces, respectively (the latter due to body forces and lateral surface tractions, and both expressed in the subdomain reference system), whereas

[1] We consider that each of these end boundaries are either strictly displacement boundaries or traction boundaries.

[2] For instance, if the fictitious interfaces are numbered consecutively, then $\boldsymbol{j} = \{1, N\}$.

$\bar{\boldsymbol{F}}_I \in \mathbb{R}^{3l_I}$ stands for nodal external forces, expressed in the interface reference system, due to the surface tractions applied on the fictitious interfaces at the end of the beam Γ_I ($I \in \boldsymbol{j}_I$). Introducing the preceding equations into Eq. (14), and expanding the variation of the interface potential (13), we get, upon gathering the terms involving variations of the unknowns of the problem ($\delta\boldsymbol{d}^e$, $\delta\boldsymbol{\lambda}^e$, and $\delta\boldsymbol{u}^e$), the following variational equations:

$$\sum_{e=1}^{M} \delta\boldsymbol{d}^{eT} \left(\boldsymbol{F}^e_{\boldsymbol{int}}(\boldsymbol{d}^e) - \boldsymbol{F}^e_{\boldsymbol{ext}} - \boldsymbol{\lambda}^e\right) = 0, \tag{18}$$

$$\sum_{e=1}^{M} \delta\boldsymbol{\lambda}^{eT}_{\mathbf{f}} (\boldsymbol{d}^e_{\mathbf{f}} - \boldsymbol{D}^e\boldsymbol{u}^e) = 0, \tag{19}$$

$$\sum_{e=1}^{M} \delta\boldsymbol{u}^{eT} \boldsymbol{D}^{eT} \boldsymbol{\lambda}^e_{\mathbf{f}} - \sum_{I\in\boldsymbol{j}_I} \delta\boldsymbol{u}_I^T \bar{\boldsymbol{F}}_I = 0, \tag{20}$$

which are to be met for all $\delta\boldsymbol{d}^e$, $\delta\boldsymbol{\lambda}^e_{\mathbf{f}}$, and all $\delta\boldsymbol{u}^e$ and $\delta\boldsymbol{u}_I$ compatible with the Dirichlet boundary conditions. The parenthetical terms in Eq. (18) and Eq. (19) represent equilibrium and compatibility, respectively, at subdomain level, whereas Eq. (20) encapsulates the equations of equilibrium at interface level.

Remark 3.1. The three-field energy functional (12) is based on the Localized Lagrange Multiplier (LLM) method, proposed by Park et al. in Refs. [28,33]. The reasons for favoring this method over other partitioning techniques were laid out by the second author in Ref. [27] for the case of periodic materials — and the same reasons apply to the general case addressed here. First and foremost, the LLM allows one to seamlessly deal with non-conforming partitions (non-conformity here is to be understood in a broader sense, that is, not only as non-matching grids, but also in terms of the spaces spanned by the modes at the common boundaries[3]). Using the LLM approach brings another valuable advantage, which is that, since the displacement of the fictitious interfaces is assumed independent of the displacement of the subdomains, we can introduce an independent modal approximation for the displacement of such interfaces. The amplitude of such modes will become the coarse-scale degrees of freedom of the final reduced-order model (this will be explained in detail in Section 6.1).

4. Offline training stage

As customary in any model reduction endeavor, the first step in the construction of the HROM is the *training stage*, in which the full-order (fine-scale) FE equilibrium equations are solved for a representative sample of the parameter space, denoted by $\mathcal{D}^{train} = \{\boldsymbol{\mu}_1, \boldsymbol{\mu}_2 \dots \boldsymbol{\mu}_P\} \subset \mathcal{D}$. The resulting solutions are stored in *snapshot* matrices, which will be then processed via the SVD in order to determine dominant spatial modes. As opposed to standard reduced-order models, however, here we are not interested in determining *global* modes, but rather in capturing *local* patterns of behavior in terms of displacements and forces, characteristic of each subdomain Ω^e. Accordingly, the solutions for each input parameter are to be stored separately, with *one snapshot matrix per subdomain*. More specifically, three groups of snapshot matrices are required to construct the proposed HROM, namely, nodal displacements:

$$\boldsymbol{A}^e_{\boldsymbol{d}} = \left[\boldsymbol{d}^e(\boldsymbol{\mu}_1) \quad \boldsymbol{d}^e(\boldsymbol{\mu}_2) \quad \cdots \quad \boldsymbol{d}^e(\boldsymbol{\mu}_P)\right], \qquad e = 1, 2 \dots M; \tag{21}$$

stresses at the Gauss points of the mesh:

$$\boldsymbol{A}^e_{\boldsymbol{\sigma}} = \left[\boldsymbol{S}^e(\boldsymbol{\mu}_1) \quad \boldsymbol{S}^e(\boldsymbol{\mu}_2) \quad \cdots \quad \boldsymbol{S}^e(\boldsymbol{\mu}_P)\right], \qquad e = 1, 2 \dots M; \tag{22}$$

and interface forces:

$$\boldsymbol{A}^e_{\boldsymbol{\lambda}} = \left[\boldsymbol{\lambda}^e_{\mathbf{f}}(\boldsymbol{\mu}_1) \quad \boldsymbol{\lambda}^e_{\mathbf{f}}(\boldsymbol{\mu}_2) \quad \cdots \quad \boldsymbol{\lambda}^e_{\mathbf{f}}(\boldsymbol{\mu}_P)\right], \qquad e = 1, 2 \dots M. \tag{23}$$

In Eq. (22), $\boldsymbol{S}^e \in \mathbb{R}^{6m^e_{gs}}$ is the vector formed by gathering in a single column the Cauchy stresses $\boldsymbol{\sigma} \in \mathbb{R}^6$ at all the m^e_{gs} Gauss points of the finite element mesh of Ω^e. Regarding the interface forces in Eq. (23), if the full-scale equations are solved using a standard domain decomposition method, this variable is a natural byproduct of the formulation. If, by contrast, the problem is addressed without exploiting the coarse decomposition, this variable has to be determined from the nodal residual at subdomain level.

[3] In our case, since the modes of each domain are obtained independently from one another, the spaces spanned by the modes of two contiguous subdomains at a common boundary are not guaranteed to coincide, hence the non-conformity.

5. Low-dimensional approximations

5.1. Overview

Once we have at our disposal the snapshot matrices described in the foregoing, the next step in the construction of the HROM is the approximation of the nodal unknowns appearing in the variational Eqs. (18) to (20) (subdomain displacements $\boldsymbol{d}^e$ subdomain interaction forces $\boldsymbol{\lambda}_{\mathbf{f}}^e$ and interface displacements $\boldsymbol{u}_I$) as a linear combination of precomputed global basis vectors or *modes*. In this regard, we adopt and extend, to the case of arbitrary partitions, the approach proposed by the second author in Ref. [27] for periodic structures, according to which each of these variables admits the following linear expansions:

$$\text{Subdomain displacements:} \quad \boldsymbol{d}^e = \boldsymbol{\Phi}^e \boldsymbol{q}^e = \overbrace{\widehat{\boldsymbol{\Phi}}^e \widehat{\boldsymbol{q}}^e}^{\text{Rigid body}} + \overbrace{\widetilde{\boldsymbol{\Phi}}^e \widetilde{\boldsymbol{q}}^e}^{\text{Deformational}}, \qquad e = 1, 2 \dots M \tag{24}$$

$$\text{Subdomain interaction forces:} \quad \boldsymbol{\lambda}_{\mathbf{f}}^e = \boldsymbol{\Psi}_{\mathbf{f}}^e \boldsymbol{r}^e = \overbrace{\widehat{\boldsymbol{\Psi}}_{\mathbf{f}}^e \widehat{\boldsymbol{r}}^e}^{\text{Resultant}} + \overbrace{\widetilde{\boldsymbol{\Psi}}_{\mathbf{f}}^e \widetilde{\boldsymbol{r}}^e}^{\text{Self-equilibrated}}, \qquad e = 1, 2 \dots M \tag{25}$$

$$\text{Interface displacements:} \quad \boldsymbol{u}_I = \boldsymbol{V}_I \boldsymbol{a}_I = \overbrace{\widehat{\boldsymbol{V}}_I \widehat{\boldsymbol{a}}_I}^{\text{Rigid body}} + \overbrace{\widetilde{\boldsymbol{V}}_I \widetilde{\boldsymbol{a}}_I}^{\text{Fluctuations}}, \qquad I = 1, 2 \dots N. \tag{26}$$

Here, $\boldsymbol{\Phi}^e$, $\boldsymbol{\Psi}_{\mathbf{f}}^e$ and $\boldsymbol{V}_I$ are the basis matrices corresponding to domain displacements, interaction forces and interface displacements, respectively, while $\boldsymbol{q}^e$, $\boldsymbol{r}^e$ and $\boldsymbol{a}_I$ are the corresponding amplitudes. Note that each variable is further decomposed into two components, with their corresponding basis matrices and amplitudes. The basis matrices identified by a hat over the corresponding letter are matrices which solely depend on the geometry of the subdomains and the corresponding FE discretizations, namely: the subdomain and interface matrices of *rigid-body modes*, $\widehat{\boldsymbol{\Phi}}^e$ and $\widehat{\boldsymbol{V}}_I$, respectively, and the matrix of *resultant modes* $\widehat{\boldsymbol{\Psi}}_{\mathbf{f}}^e$ (to be defined later). On the other hand, the matrices identified by a tilde over the symbol — namely, the subdomain *deformational modes* $\widetilde{\boldsymbol{\Phi}}^e$, the *interface fluctuation modes* $\widetilde{\boldsymbol{V}}_I$, and the subdomain *self-equilibrated modes* $\widetilde{\boldsymbol{\Psi}}_{\mathbf{f}}^e$ — are empirical matrices, in the sense that they are derived from the data collected during the training stage, more specifically, from the snapshot matrices given in Eqs. (21) and (23), as we shall explain later. We further impose the following *orthogonality* conditions to each decomposition:

$$\widehat{\boldsymbol{\Phi}}^{eT} \boldsymbol{M}^e \widetilde{\boldsymbol{\Phi}}^e = \boldsymbol{0}, \qquad e = 1, 2 \dots M \tag{27}$$

$$\widehat{\boldsymbol{\Psi}}_{\mathbf{f}}^{eT} \boldsymbol{M}_{\mathbf{ff}}^{e-1} \widetilde{\boldsymbol{\Psi}}_{\mathbf{f}}^e = \boldsymbol{0}, \qquad e = 1, 2 \dots M \tag{28}$$

$$\widehat{\boldsymbol{V}}_I^T \bar{\boldsymbol{M}}_I \widetilde{\boldsymbol{V}}_I = \boldsymbol{0}, \qquad I = 1, 2 \dots N, \tag{29}$$

where $\boldsymbol{M}^e \in \mathbb{R}^{3n^e \times 3n^e}$ and $\bar{\boldsymbol{M}}_I \in \mathbb{R}^{3l_I \times 3l_I}$ denote the *geometric* nodal mass matrices[4] of subdomain Ω^e and interface Γ_I, respectively; whereas $\boldsymbol{M}_{\mathbf{ff}}^e$ is defined by

$$\boldsymbol{M}_{\mathbf{ff}}^e = \begin{bmatrix} \boldsymbol{M}_{\mathbf{f}_1\mathbf{f}_1}^e & \boldsymbol{0} \\ \boldsymbol{0} & \boldsymbol{M}_{\mathbf{f}_2\mathbf{f}_2}^e \end{bmatrix}, \qquad e = 1, 2 \dots M, \tag{30}$$

$\boldsymbol{M}_{\mathbf{f}_i\mathbf{f}_i}^e \in \mathbb{R}^{3l_i^e \times 3l_i^e}$ being the block matrix of $\boldsymbol{M}^e$ corresponding to the interface boundary DOFs $\mathbf{f}_i^e$ $(i = 1, 2)$.

Remark 5.1. Orthogonality conditions between nodal displacements, in Eqs. (27) and (29), are established in terms of their corresponding geometric mass matrices because the inner product associated to the geometric mass matrix is the discrete counterpart of the L_2-inner product. A similar reasoning applies to Eq. (28): the L_2 inner product for surface tractions on a given boundary surface translates into a discrete inner product defined in terms of the inverse of the geometric mass matrix. We prove these two statements in Appendix A, Propositions A.1 and A.2.

In what follows, we provide further details on decompositions (24), (25) and (26), with emphasis on how to determine the empirical components of each decomposition from the snapshot matrices introduced in Eqs. (21) and (23).

[4] The definition of $\boldsymbol{M}^e$ is given in Eq. (A.2) of Appendix A.

5.2. Subdomain displacements

Decomposition in Eq. (24) into rigid-body and *deformational or straining* components is a standard one in Localized-Lagrange partition methods, see e.g. [28]. The expression for the rows of the matrix of rigid-body modes $\widehat{\boldsymbol{\Phi}}^e \in \mathbb{R}^{3n^e \times 6}$ corresponding to the jth node reads:

$$[\widehat{\boldsymbol{\Phi}}^e]_j = \begin{bmatrix} 1 & 0 & 0 & 0 & [\boldsymbol{X}_j^e]_3 & -[\boldsymbol{X}_j^e]_2 \\ 0 & 1 & 0 & -[\boldsymbol{X}_j^e]_3 & 0 & [\boldsymbol{X}_j^e]_1 \\ 0 & 0 & 1 & [\boldsymbol{X}_j^e]_2 & -[\boldsymbol{X}_j^e]_1 & 0 \end{bmatrix} \qquad j = 1, 2 \dots n^e; \quad e = 1, 2 \dots M, \tag{31}$$

where $\boldsymbol{X}_j^e \in \mathbb{R}^3$ denotes the coordinates of the node in the local reference system of subdomain Ω^e. Notice that we have placed the translations modes as the first 3 columns of the matrix. Thus, the first 3 entries of $\hat{\boldsymbol{q}}^e \in \mathbb{R}^6$ represent translations along the local axes of domain Ω^e, while the remaining entries represent infinitesimal rotations around its centroid.

The orthogonal projection matrix that maps nodal displacement vectors onto the column space of the rigid body modes $\widehat{\boldsymbol{\Phi}}^e$, denoted by $span(\widehat{\boldsymbol{\Phi}}^e)$, is given by

$$\widehat{\boldsymbol{\mathcal{S}}}^e := \widehat{\boldsymbol{\Phi}}^e (\widehat{\boldsymbol{\Phi}}^{eT} \boldsymbol{M}^e \widehat{\boldsymbol{\Phi}}^e)^{-1} \widehat{\boldsymbol{\Phi}}^{eT} \boldsymbol{M}^e, \qquad e = 1, 2 \dots M \tag{32}$$

(orthogonality is defined in terms of the geometric mass matrix $\boldsymbol{M}^e$, as demanded by condition in Eq. (27)). Accordingly, the operator defined by

$$\widetilde{\boldsymbol{\mathcal{S}}}^e := \boldsymbol{I} - \widehat{\boldsymbol{\mathcal{S}}}^e, \qquad e = 1, 2 \dots M \tag{33}$$

maps displacement vectors onto the orthogonal complement of $span(\widehat{\boldsymbol{\Phi}}^e) \in \mathbb{R}^{n^e}$, which is nothing but the subspace of *deformational displacements* of domain Ω^e. It may be inferred, thus, that the matrix of *deformational* modes appearing in decomposition (24), $\widetilde{\boldsymbol{\Phi}}^e \in \mathbb{R}^{3n^e \times p^e}$, will be a linear combination of the columns of $\widetilde{\boldsymbol{\mathcal{S}}}^e \boldsymbol{A}_{\boldsymbol{d}}^e$, or to put it alternatively, the column space of the desired matrix will be a subspace of the column space of the snapshot matrix:

$$span(\widetilde{\boldsymbol{\Phi}}^e) \subseteq span(\widetilde{\boldsymbol{\mathcal{S}}}^e \boldsymbol{A}_{\boldsymbol{d}}^e), \qquad e = 1, 2 \dots M. \tag{34}$$

However, at this juncture of the discussion, we cannot specify which particular subspace is to be chosen, because the choice depends on the as yet unaddressed self-equilibrated interface force modes $\widetilde{\boldsymbol{\Psi}}^e$. The procedure for finally computing the domain deformational modes $\widetilde{\boldsymbol{\Phi}}^e$ will be explained later on, in Section 5.3.1.

5.3. Interaction forces

The matrix of *resultant modes* $\widehat{\boldsymbol{\Psi}}_{\mathbf{f}}^e \in \mathbb{R}^{3(l_1^e + l_2^e) \times 6}$ appearing in Eq. (25) is defined in terms of the rigid-body modes of the subdomain as

$$\widehat{\boldsymbol{\Psi}}_{\mathbf{f}}^e = \boldsymbol{M}_{\mathbf{ff}}^e \widehat{\boldsymbol{\Phi}}_{\mathbf{f}}^e = \boldsymbol{M}_{\mathbf{f}_1\mathbf{f}_1}^e \widehat{\boldsymbol{\Phi}}_{\mathbf{f}_1}^e + \boldsymbol{M}_{\mathbf{f}_2\mathbf{f}_2}^e \widehat{\boldsymbol{\Phi}}_{\mathbf{f}_2}^e, \qquad e = 1, 2 \dots M. \tag{35}$$

As argued in Ref. [27], enriching the modal basis for interaction forces with these *resultant* modes allows the reduced-order model to exactly capture the transmission between subdomains of the resultants and moment resultants of arbitrary body forces and lateral surface tractions, even if the training sample $\mathcal{D}^{train}$ does not consider such forces.

In analogy to Eqs. (32) and (33), we introduce the orthogonal projection matrices

$$\widehat{\boldsymbol{\mathcal{H}}}^e := \widehat{\boldsymbol{\Psi}}_{\mathbf{f}}^e (\widehat{\boldsymbol{\Psi}}_{\mathbf{f}}^{eT} \boldsymbol{M}_{\mathbf{ff}}^{e^{-1}} \widehat{\boldsymbol{\Psi}}_{\mathbf{f}}^e)^{-1} \widehat{\boldsymbol{\Psi}}_{\mathbf{f}}^{eT} \boldsymbol{M}_{\mathbf{ff}}^{e^{-1}}, \qquad e = 1, 2 \dots M \tag{36}$$

and

$$\widetilde{\boldsymbol{\mathcal{H}}}^e = \boldsymbol{I} - \widehat{\boldsymbol{\mathcal{H}}}^e, \qquad e = 1, 2 \dots M \tag{37}$$

which map nodal interface force vectors onto $span(\widehat{\boldsymbol{\Psi}}_{\mathbf{f}}^e)$ and its orthogonal complement, respectively — orthogonality in this case is defined in terms of the norm induced by $\boldsymbol{M}_{\mathbf{ff}}^{e^{-1}}$, as required by condition (28).

Algorithm 1: Weighted (truncated) Singular Value decomposition (from Ref. [27])

Function $[\boldsymbol{U}, \boldsymbol{S}, \boldsymbol{V}]$ =WSVD$(\boldsymbol{A}, \boldsymbol{M}, TOL)$:
  Data: $\boldsymbol{A} \in \mathbb{R}^{n\times m}$, $\boldsymbol{M} \in \mathbb{R}^{n\times n}$ (positive definite), tolerance $0 \leq TOL \leq 1$
  Result: $\boldsymbol{U} \in \mathbb{R}^{n\times r}$, $\boldsymbol{S} \in \mathbb{R}^{r\times r}$, $\boldsymbol{V} \in \mathbb{R}^{m\times r}$ ($r \leq min(n,m)$), with $\boldsymbol{U}^T\boldsymbol{M}\boldsymbol{U} = \boldsymbol{V}^T\boldsymbol{V} = \boldsymbol{I}_{r\times r}$, $\boldsymbol{S}_{(i+1,i+1)} \geq \boldsymbol{S}_{(i,i)} > 0$, such that $\boldsymbol{A} = \boldsymbol{U}\boldsymbol{S}\boldsymbol{V}^T + \boldsymbol{E}$, $\|\boldsymbol{E}\|_{\boldsymbol{M}} \leq \epsilon\|\boldsymbol{A}\|_{\boldsymbol{M}}$
  $\bar{\boldsymbol{M}} \leftarrow$chol$(\boldsymbol{M})$ // Cholesky decomposition of $\boldsymbol{M}$, i.e. $\boldsymbol{M} = \bar{\boldsymbol{M}}^T\bar{\boldsymbol{M}}$
  $\boldsymbol{A} \leftarrow \bar{\boldsymbol{M}}\boldsymbol{A}$
  $[\bar{\boldsymbol{U}}, \boldsymbol{S}, \boldsymbol{V}] \leftarrow$ SVD$(\boldsymbol{A}, TOL)$ // Truncated SVD of $\boldsymbol{A}$.
  $\boldsymbol{U} \leftarrow \bar{\boldsymbol{M}}^{-1}\bar{\boldsymbol{U}}$

The term "resultant modes" refers to the fact that the resultants and moment resultants (with respect to the centroid of the domain) of a given interface force vector $\boldsymbol{\lambda}_{\mathbf{f}}^e$ and its projection $\widehat{\boldsymbol{\mathcal{H}}}^e\boldsymbol{\lambda}_{\mathbf{f}}^e$ are identical. Indeed, by virtue of Eqs. (35) and (36), we have that[5]:

$$\widehat{\boldsymbol{\Phi}}_{\mathbf{f}}^{e^T}\widehat{\boldsymbol{\mathcal{H}}}^e\boldsymbol{\lambda}_{\mathbf{f}}^e = \widehat{\boldsymbol{\Phi}}_{\mathbf{f}}^{e^T}\boldsymbol{M}_{\mathbf{ff}}^e\widehat{\boldsymbol{\Phi}}_{\mathbf{f}}^e(\widehat{\boldsymbol{\Phi}}_{\mathbf{f}}^{e^T}\boldsymbol{M}_{\mathbf{ff}}^e\widehat{\boldsymbol{\Phi}}_{\mathbf{f}}^e)^{-1}\hat{\boldsymbol{\Phi}}_{\mathbf{f}}^{eT}\boldsymbol{\lambda}_{\mathbf{f}}^e = \widehat{\boldsymbol{\Phi}}_{\mathbf{f}}^{e^T}\boldsymbol{\lambda}_{\mathbf{f}}^e, \qquad e = 1, 2 \dots M. \tag{38}$$

Conversely, the self-equilibrated modes are so named because their resultants and moment resultants with respect to the centroid of the subdomain are zero:

$$\widehat{\boldsymbol{\Phi}}^{e^T}\widetilde{\boldsymbol{\Psi}}^e = \widehat{\boldsymbol{\Phi}}_{\mathbf{f}}^{e^T}\widetilde{\boldsymbol{\Psi}}_{\mathbf{f}}^e = \mathbf{0} \tag{39}$$

(this readily follows from Eqs. (25), (28) and (35)). Thus, operator $\widetilde{\boldsymbol{\mathcal{H}}}^e$ allows one to extract the *self-equilibrated* part of any nodal interface vector. In particular, the matrix of *self-equilibrated modes* $\widetilde{\boldsymbol{\Psi}}_{\mathbf{f}}^e$ appearing in decomposition (25) will be a linear combination of $\widetilde{\boldsymbol{\mathcal{H}}}^e\boldsymbol{A}_{\boldsymbol{\lambda}}^e$ — the self-equilibrated component of the snapshot matrix given in Eq. (23). We may determine this linear combination by means of the weighted SVD (see Algorithm 1):

$$[\widetilde{\boldsymbol{\Psi}}_{\mathbf{f}}^e, \bullet, \bullet] = \texttt{WSVD}(\widetilde{\boldsymbol{\mathcal{H}}}^e\boldsymbol{A}_{\boldsymbol{\lambda}}^e, \boldsymbol{M}_{\mathbf{ff}}^{e^{-1}}, \epsilon_\lambda), \qquad e = 1, 2 \dots M \tag{40}$$

where $0 \leq \epsilon_\lambda \leq 1$ is a user-prescribed tolerance.[6] Alternatively, rather than applying the decomposition to the whole matrix of snapshots, one may calculate the modes corresponding to different blocks of the matrix (for instance, the blocks associated to each training test), and then orthogonalize the set of modes using again the SVD (this is the strategy followed in the numerical example discussed in Section 9.3.2).

5.3.1. Relation between deformational and self-equilibrated modes

Let us calculate the work performed by the self-equilibrated modes $\widetilde{\boldsymbol{\Psi}}^e \in \mathbb{R}^{3n^e\times p^e}$ over a subdomain nodal displacement $\boldsymbol{d}^e$; by using Eq. (24), this work is expressible as

$$\widetilde{\boldsymbol{\Psi}}^{e^T}\boldsymbol{d}^e = \widetilde{\boldsymbol{\Psi}}^{e^T}\left(\widetilde{\boldsymbol{\Phi}}^e\tilde{\boldsymbol{q}}^e + \widehat{\boldsymbol{\Phi}}^e\hat{\boldsymbol{q}}^e\right) = (\widetilde{\boldsymbol{\Psi}}^{e^T}\widetilde{\boldsymbol{\Phi}}^e)\tilde{\boldsymbol{q}}^e, \qquad e = 1, 2 \dots M, \tag{41}$$

where we have exploited the fact that, by virtue of Eq. (39), the term involving rigid-body displacements vanishes. This expression indicates that the deformational modes $\widetilde{\boldsymbol{\Phi}}^e$ are *work conjugate to the self-equilibrated modes*. The matrix appearing in the rightmost term of the above equation will be denoted henceforth by

$$\boldsymbol{H}^e := \widetilde{\boldsymbol{\Psi}}^{e^T}\widetilde{\boldsymbol{\Phi}}^e = \widetilde{\boldsymbol{\Psi}}_{\mathbf{f}_1}^{e^T}\widetilde{\boldsymbol{\Phi}}_{\mathbf{f}_1}^e + \widetilde{\boldsymbol{\Psi}}_{\mathbf{f}_2}^{e^T}\widetilde{\boldsymbol{\Phi}}_{\mathbf{f}_2}^e. \tag{42}$$

In Ref. [27], it is demonstrated that, in order to cast the coarse-scale problem solely in terms of the coarse-scale DOFs $\boldsymbol{a}$ — one of the premises of the present work —, it is necessary that this matrix $\boldsymbol{H}^e$ be invertible. We shall enforce this invertibility condition, as well as condition (34), by following the procedure outlined in Box 5.1. Essentially, it consists in determining $\widetilde{\boldsymbol{\Phi}}^e$ as a linear combination of the deformational component of the displacement snapshots (denoted by $\widetilde{\boldsymbol{A}}_{\boldsymbol{d}}^e$, see step 1), i.e., $\widetilde{\boldsymbol{\Phi}}^e = \widetilde{\boldsymbol{A}}_{\boldsymbol{d}}^e\boldsymbol{c}$. The vector of coefficients $\boldsymbol{c}$, on the other

[5] The resultants and moment resultants of a system of nodal forces are calculated by multiplying the transpose of the rigid-body modes and the vector of nodal forces, see e.g. [27]

[6] Notice that, in using $\boldsymbol{M}_{\mathbf{ff}}^{e^{-1}}$ as weighting matrix, the resulting modes becomes orthogonal in this matrix, that is: $\widetilde{\boldsymbol{\Psi}}_{\mathbf{f}}^{e^T}\boldsymbol{M}_{\mathbf{ff}}^{e^{-1}}\widetilde{\boldsymbol{\Psi}}_{\mathbf{f}}^e = \boldsymbol{I}$.

hand, is obtained from the projection of $\widetilde{\boldsymbol{\Psi}}_{\mathbf{f}}^{e}$ onto $\widetilde{\boldsymbol{A}}_{\boldsymbol{d}}^{e}(\mathbf{f}^{e},:)$ (step 3). Physically, this is equivalent to choose $\widetilde{\boldsymbol{\Phi}}^{e}$ as the deformational displacement modes that *contribute the most to the work done by the interaction forces*. If the dimension of the projected subspace happens to be less than the number of interface deformational displacement modes ($\widetilde{\boldsymbol{\Phi}}_{f}^{e}$), this implies that some of the force patterns in $\widetilde{\boldsymbol{\Psi}}_{\mathbf{f}}^{e}$ does not correspond to any displacement of the interface boundaries; accordingly, in such circumstances, in order to guarantee the invertibility of $\boldsymbol{H}^{e}$, we discard the less significant mode in $\widetilde{\boldsymbol{\Psi}}_{\mathbf{f}}^{e}$ (the one with the smallest singular value, see step 4), and repeat the procedure.

Given $\boldsymbol{A}_{\boldsymbol{d}}^{e}$ (matrix of displacement snapshots, see Eq. (21)) and $\widetilde{\boldsymbol{\Psi}}_{\mathbf{f}}^{e}$ (self-equilibrated modes, computed in expression (40)), find $\widetilde{\boldsymbol{\Phi}}^{e}$ such that $span(\widetilde{\boldsymbol{\Phi}}^{e}) \subseteq span(\widetilde{\boldsymbol{\mathcal{S}}}^{e}\boldsymbol{A}_{\boldsymbol{d}}^{e}))$ and $\boldsymbol{H}^{e} = \widetilde{\boldsymbol{\Psi}}^{e^{T}}\widetilde{\boldsymbol{\Phi}}^{e}$ is invertible.

1. Compute the deformational component of $\boldsymbol{A}_{\boldsymbol{d}}^{e}$:

$$\widetilde{\boldsymbol{A}}_{\boldsymbol{d}}^{e} = \widetilde{\boldsymbol{\mathcal{S}}}^{e}\boldsymbol{A}_{\boldsymbol{d}}^{e} \tag{43}$$

2. Determine the SVD of the row block of $\widetilde{\boldsymbol{A}}_{\boldsymbol{d}}^{e}$ corresponding to the interfaces (DOFs $\mathbf{f}^{e}$)

$$[\boldsymbol{U}_{a}, \boldsymbol{S}_{a}, \boldsymbol{V}_{a}] = \mathtt{SVD}(\widetilde{\boldsymbol{A}}_{\boldsymbol{d}}^{e}(\mathbf{f}^{e},:), 0)$$

3. Obtain the SVD of the coefficients of the projection of $\widetilde{\boldsymbol{\Psi}}_{\mathbf{f}}^{e}$ onto $span(\boldsymbol{U}_{a})$:

$$[\boldsymbol{U}_{u}, \boldsymbol{S}_{u}, \boldsymbol{V}_{u}] = \mathtt{SVD}(\boldsymbol{U}_{a}^{T}\widetilde{\boldsymbol{\Psi}}_{\mathbf{f}}^{e}, 0) \tag{44}$$

4. If $\mathtt{ncol}(\boldsymbol{U}_{u}) = p^{e} = \mathtt{ncol}(\widetilde{\boldsymbol{\Psi}}_{\mathbf{f}}^{e})$ (here $\mathtt{ncol}(\bullet)$ denotes number of columns), then go to step 5; otherwise, make $\widetilde{\boldsymbol{\Psi}}_{\mathbf{f}}^{e} \leftarrow \widetilde{\boldsymbol{\Psi}}_{\mathbf{f}}^{e}(:, 1 : p^{e} - 1)$ and return to step 3.
5. Compute

$$\boldsymbol{B} = \widetilde{\boldsymbol{A}}_{\boldsymbol{d}}^{e}(\boldsymbol{S}_{a}\boldsymbol{V}_{a})\boldsymbol{U}_{u} \tag{45}$$

6. Orthogonalize $\boldsymbol{B}$ with respect to $\boldsymbol{M}^{e}$ by applying the weighted SVD (see Algorithm 1):

$$[\widetilde{\boldsymbol{\Phi}}^{e}, \bullet, \bullet] = \mathtt{WSVD}(\boldsymbol{B}, \boldsymbol{M}^{e}, 0) \tag{46}$$

Box 5.1: Computation of deformational modes $\widetilde{\boldsymbol{\Phi}}^{e}$ (for a given subdomain Ω^{e}, $e = 1, 2 \ldots M$)

6. Fictitious interface displacements

6.1. Coarse-scale DOFs

We focus now on Eq. (26), which is the modal expansion of the fictitious interface displacements. Matrix $\boldsymbol{V}_{I} \in \mathbb{R}^{3l_{I} \times s_{I}}$ in Eq. (26) is the matrix of displacement modes of interface Γ_{I}, whereas $\boldsymbol{a}_{I} \in \mathbb{R}^{s_{I}}$ stands for the corresponding amplitudes ($I = 1, 2 \ldots N$). Following the proposal in Ref. [27], we shall assign to $\boldsymbol{a}_{I}$ the role of *coarse-scale DOFs* (or generalized displacements) associated to the fictitious interface Γ_{I}, whose centroid will be accordingly conceptualized as a *coarse-scale node* (as in a typical beam finite element formulation). Likewise, the global vector of coarse-scale DOFs will be formed by stacking in a single column the coarse-scale DOFs of all interfaces:

$$\boldsymbol{a} = \begin{bmatrix} \boldsymbol{a}_{1} \\ \boldsymbol{a}_{2} \\ \vdots \\ \boldsymbol{a}_{N} \end{bmatrix}. \tag{47}$$

To facilitate the formulation, the fictitious displacements associated to a subdomain Ω^e, see Eq. (6), are written using the following compact notation:

$$\boldsymbol{u}^e = \boldsymbol{V}^e \boldsymbol{a}^e, \qquad e = 1, 2 \dots M \tag{48}$$

where

$$\boldsymbol{V}^e := \begin{bmatrix} \boldsymbol{V}_1^e & \boldsymbol{0} \\ \boldsymbol{0} & \boldsymbol{V}_2^e \end{bmatrix} = \begin{bmatrix} \boldsymbol{V}_I & \boldsymbol{0} \\ \boldsymbol{0} & \boldsymbol{V}_J \end{bmatrix}, \qquad \boldsymbol{a}^e = \begin{bmatrix} \boldsymbol{a}_1^e \\ \boldsymbol{a}_2^e \end{bmatrix} = \begin{bmatrix} \boldsymbol{a}_I \\ \boldsymbol{a}_J \end{bmatrix} \tag{49}$$

with $I = \mathcal{T}(e, 1)$ and $J = \mathcal{T}(e, 2)$ ($e = 1, 2 \dots M$). Lastly, we introduce two Boolean operators $\boldsymbol{L}^e$ and $\bar{\boldsymbol{L}}_I$ relating the global vector of coarse-scale DOFs with the coarse-scale DOFs of domain Ω^e and fictitious interface Γ_I, respectively:

$$\boldsymbol{a}^e = \boldsymbol{L}^e \boldsymbol{a}, \quad (e = 1, 2 \dots M), \qquad \boldsymbol{a}_I = \bar{\boldsymbol{L}}_I \boldsymbol{a}. \quad (I = 1, 2 \dots N). \tag{50}$$

6.2. Interface rigid-body modes

In analogy to the case of subdomain displacements, interface displacements in Eq. (26) are also orthogonally decomposed into a rigid-body component, $\widehat{\boldsymbol{V}}_I \widehat{\boldsymbol{a}}_I$, and a deformational component, $\widetilde{\boldsymbol{V}}_I \tilde{\boldsymbol{a}}_I$. Notice that the latter may be interpreted as *spatial fluctuations* with respect to a hypothetical *plane* cross-section configuration. For this reason, we shall also refer to $\widetilde{\boldsymbol{V}}_I \tilde{\boldsymbol{a}}_I$ as the vector of *interface fluctuations*. The matrix of rigid-body modes $\widehat{\boldsymbol{V}}_I \in \mathbb{R}^{3 l_I \times 6}$ is given by (for a given node j):

$$[\widehat{\boldsymbol{V}}_I]_j = \begin{bmatrix} 1 & 0 & 0 & 0 & [\boldsymbol{Y}_j^e]_3 & -[\boldsymbol{Y}_j^e]_2 \\ 0 & 1 & 0 & -[\boldsymbol{Y}_j^e]_3 & 0 & [\boldsymbol{Y}_j^e]_1 \\ 0 & 0 & 1 & [\boldsymbol{Y}_j^e]_2 & -[\boldsymbol{Y}_j^e]_1 & 0 \end{bmatrix} \qquad j = 1, 2 \dots l_I; \quad I = 1, 2 \dots N \tag{51}$$

where $\boldsymbol{Y}_j^e \in \mathbb{R}^3$ denotes the coordinates of the node in the local reference system attached to the interface Γ_I (which recall it is located at its centroid).

Remark 6.1. The matrix of rigid-body modes $\widehat{\boldsymbol{V}}_I$ is to be invariably included in the modal expansion of fictitious interface displacements, for otherwise pure rigid-body rotations could not be represented exactly. This means that, at the very least, each coarse-scale node has 6 DOFs (as in a typical finite element beam formulation): 3 translations and 3 rotations (the latter referred to the centroid of the fictitious interface).

6.3. Interface fluctuation modes

Let us turn now our attention to the determination of what we have called the matrix of fluctuation (or fluctuating) modes $\widetilde{\boldsymbol{V}}_I$ ($I = 1, 2 \dots N$). The operator that extracts the fluctuating component of a given nodal displacements of Γ_I is defined by

$$\widetilde{\boldsymbol{\mathcal{P}}}_I = \boldsymbol{I} - \widehat{\boldsymbol{\mathcal{P}}}_I, \qquad I = 1, 2 \dots N, \tag{52}$$

where

$$\widehat{\boldsymbol{\mathcal{P}}}_I = \widehat{\boldsymbol{V}}_I (\widehat{\boldsymbol{V}}_I^T \bar{\boldsymbol{M}}_I \widehat{\boldsymbol{V}}_I)^{-1} \widehat{\boldsymbol{V}}_I^T \bar{\boldsymbol{M}}_I, \qquad I = 1, 2 \dots N. \tag{53}$$

Note that $\widetilde{\boldsymbol{\mathcal{P}}}_I$ in Eq. (52) is the interface counterpart of the subdomain operator $\widetilde{\boldsymbol{\mathcal{S}}}^e$, defined in Eq (33), which was used to purge the rigid-body component from the domain displacement snapshots $\boldsymbol{A}_{\boldsymbol{d}}^e$ determined in the training stage. However, in this case, there is no such a thing as a snapshot matrix of interface displacements onto which to apply this operator. Rather, the fluctuation component of a given interface displacement is to be determined from the deformational modes of the subdomains modes sharing the interface, as explained in what follows.

Algorithm 2: Intersection of subspaces

1 **Function** $\boldsymbol{U}$ =INTS($\boldsymbol{A}$, $\boldsymbol{B}$, $\boldsymbol{M}$, ϵ_f):
  Data: Matrices $\boldsymbol{A} \in \mathbb{R}^{n\times m}$, $\boldsymbol{B} \in \mathbb{R}^{n\times p}$, $\boldsymbol{M} \in \mathbb{R}^{n\times n}$ (positive definite). $0 \geq \epsilon_f \geq 1$ (threshold for defining intersection, e.g. $\epsilon_f = 10^{-6}$)
  Result: $\boldsymbol{U} \in \mathbb{R}^{n\times r}$, $r \leq min(m, p)$, with $\boldsymbol{U}^T\boldsymbol{M}\boldsymbol{U} = \boldsymbol{I}$ and $span(\boldsymbol{U}) = span(\boldsymbol{A}) \cap span(\boldsymbol{B})$
2 **if** $\boldsymbol{M} \neq \boldsymbol{I}$ **then** $\boldsymbol{M} \leftarrow$chol($\boldsymbol{M}$) // Cholesky decomposition of $\boldsymbol{M}$
3 $\boldsymbol{A} \leftarrow \boldsymbol{M}\boldsymbol{A}$; $\boldsymbol{B} \leftarrow \boldsymbol{M}\boldsymbol{B}$
4 $[\boldsymbol{Y}_A, \cdot, \cdot] \leftarrow$ SVD($\boldsymbol{A}$) // *Thin* SVD of $\boldsymbol{A}$. $\boldsymbol{Y}_A$ is the matrix of left singular vectors
5 $[\boldsymbol{Y}_B, \cdot, \cdot] \leftarrow$ SVD($\boldsymbol{B}$)
6 $[\boldsymbol{Z}, \boldsymbol{S}, \cdot] \leftarrow$ SVD($\boldsymbol{Y}_A^T\boldsymbol{Y}_B$) // $\boldsymbol{S}$ is a vector containing the singular values, which are the cosines of the principal angles
7 Find r such that $S_{r+1} < 1 - \epsilon_f$.
8 $\boldsymbol{U} \leftarrow \boldsymbol{M}^{-1}\boldsymbol{Y}_A\boldsymbol{Z}(:, 1:r)$ // $\boldsymbol{Z}(:, 1:r)$ is the block matrix of $\boldsymbol{Z}$ formed by columns $1, 2 \ldots r$

Indeed, consider an interface Γ_I shared by two subdomains Ω^e and Ω^g (so that $I = \mathcal{T}(e, 2) = \mathcal{T}(g, 1)$). Suppose that the deformational modes of both subdomains, $\widetilde{\boldsymbol{\Phi}}^e$ and $\widetilde{\boldsymbol{\Phi}}^g$, have been already obtained by the procedure described in Box 5.1. The nodal displacements of $\partial\Omega_2^e$ and $\partial\Omega_1^g$ referred to the mesh of the common fictitious interface Γ_I are given by

$$\boldsymbol{u}_I^- = \boldsymbol{D}_2^{e^{-1}}\boldsymbol{d}_{\mathbf{f}_2}^e, \qquad \boldsymbol{u}_I^+ = \boldsymbol{D}_1^{g^{-1}}\boldsymbol{d}_{\mathbf{f}_1}^g, \tag{54}$$

respectively (matrices $\boldsymbol{D}_2^e$ and $\boldsymbol{D}_1^g$ were defined in Eq. (8)). Furthermore, according to Eq. (24), $\boldsymbol{d}_{\mathbf{f}_2}^e \in span([\widehat{\boldsymbol{\Phi}}_{\mathbf{f}_2}^e, \widetilde{\boldsymbol{\Phi}}_{\mathbf{f}_2}^e])$ and $\boldsymbol{d}_{\mathbf{f}_1}^g \in span([\widehat{\boldsymbol{\Phi}}_{\mathbf{f}_1}^g, \widetilde{\boldsymbol{\Phi}}_{\mathbf{f}_1}^g])$. Since $\widehat{\boldsymbol{\Phi}}_{\mathbf{f}_2}^e$ and $\widehat{\boldsymbol{\Phi}}_{\mathbf{f}_1}^g$ are entries of rigid-body modes, its fluctuating components are zero, and therefore, it follows that

$$\widetilde{\boldsymbol{\mathcal{P}}}_I\boldsymbol{u}_I^- \in span(\breve{\boldsymbol{\Phi}}_I^-), \qquad \text{where} \qquad \breve{\boldsymbol{\Phi}}_I^- := \widetilde{\boldsymbol{\mathcal{P}}}_I(\boldsymbol{D}_2^{e^{-1}}\widetilde{\boldsymbol{\Phi}}_{\mathbf{f}_2}^e), \tag{55}$$

$$\widetilde{\boldsymbol{\mathcal{P}}}_I\boldsymbol{u}_I^+ \in span(\breve{\boldsymbol{\Phi}}_I^+), \qquad \text{where} \qquad \breve{\boldsymbol{\Phi}}_I^+ := \widetilde{\boldsymbol{\mathcal{P}}}_I(\boldsymbol{D}_1^{g^{-1}}\widetilde{\boldsymbol{\Phi}}_{\mathbf{f}_1}^g), \tag{56}$$

that is, the fluctuating components of $\boldsymbol{u}_I^-$ and $\boldsymbol{u}_I^+$ reside in the span of the fluctuating components of the corresponding subdomain deformational modes, denoted by $\breve{\boldsymbol{\Phi}}_I^-$ and $\breve{\boldsymbol{\Phi}}_I^+$, respectively. We seek modes common to both subspaces, or more formally, we seek an orthogonal basis matrix $\widetilde{\boldsymbol{W}}_I$ for the *intersection* of both subspaces:

$$span(\widetilde{\boldsymbol{W}}_I) = span(\breve{\boldsymbol{\Phi}}_I^-) \cap span(\breve{\boldsymbol{\Phi}}_I^+). \tag{57}$$

The operations required for computing a basis matrix for the intersection subspace are represented here by the function

$$\widetilde{\boldsymbol{W}}_I = \text{INTS}(\breve{\boldsymbol{\Phi}}_I^-, \breve{\boldsymbol{\Phi}}_I^+, \bar{\boldsymbol{M}}_I, \epsilon_f), \qquad I = 1, 2 \ldots N \tag{58}$$

described in Algorithm 2. The calculations are based on the concept of *principal angles* between two subspaces [34]. One first computes orthogonal basis matrices for both subspaces (lines 4 and 5 in Algorithm 2), and then determines the SVD of the coefficients of the projection of one subspace onto the other (line 6). As the basis matrices are orthogonal, the resulting SVD has singular values ranging between 0 and 1 — these are the cosines of the principal angles. Strictly speaking, the dimension of the intersection subspace is equal to the number of singular values equal to one. Nevertheless, we relax this condition and consider that the intersection is determined by those singular values above $1 - \epsilon_f$, where $\epsilon_f \approx 0$ is a user-prescribed threshold.

6.3.1. Well-posedness considerations

The reader may have noticed that, although our goal was to determine the basis matrix of fluctuation modes $\widetilde{\boldsymbol{V}}_I$ — the one appearing in the approximation of fictitious interface displacement in Eq. (26) — we have used a different letter ($\widetilde{\boldsymbol{W}}_I$) for representing the output of the intersection operation in expression (58). This has been done in anticipation of the fact that *not all the fluctuation modes common to the domains sharing the interface can be included in the approximation of the fictitious interface displacements*.

The rationale behind this restriction is as follows. Suppose that we have determined, for a given domain Ω^e, the deformational modes $\widetilde{\boldsymbol{\Phi}}^e$ as well as the *candidates* for fluctuation modes of the corresponding fictitious interfaces $\widetilde{\boldsymbol{W}}_1^e = \widetilde{\boldsymbol{W}}_I$ and $\widetilde{\boldsymbol{W}}_2^e = \widetilde{\boldsymbol{W}}_J$, where $I = \mathcal{T}(e,1)$, $J = \mathcal{T}(e,2)$. Let us suppose for the sake of argument that $\texttt{ncol}(\widetilde{\boldsymbol{W}}_1^e) = \texttt{ncol}(\widetilde{\boldsymbol{W}}_2^e) = \texttt{ncol}(\widetilde{\boldsymbol{\Phi}}^e) = p^e$, that is, there are as many fluctuation modes for each interface as deformational modes p^e (empirically, we have found that this is almost always the case). Next suppose we set to zero the rigid-body displacements of the subdomain, as well as the displacements of one of the fictitious interface, say Γ_I. In doing so, the displacement of the other interface boundary $\partial\Omega_2^e$ becomes describable by p^e variables (the amplitude of the subdomain deformational modes, $\tilde{\boldsymbol{q}}^e$), while the displacement of the associated fictitious interface Γ_J becomes parameterized by a total $6+p^e$ (these extra 6 DOFs are associated to the interface rigid-body modes $\widehat{\boldsymbol{V}}_I$). This means the fictitious interface Γ^J has 6 more independent modes than the boundary $\partial\Omega_2^e$ whose displacement it intends to approximate. As a consequence, since the unknowns of the coarse-scale model are the amplitudes of the fictitious interface modes, including all the columns of $\widetilde{\boldsymbol{W}}_J$ in the model would result in a *system of coarse-scale equilibrium equations with more unknowns that linearly independent equations*.

It follows from the foregoing argumentation that a necessary condition for ensuring well-posedness of the coarse-scale model is that *the number of modes for a given fictitious interface cannot be higher than the number of deformational modes of the domains sharing the interface*. This implies that the number of fluctuation modes of interface Γ_I, $\tilde{s}_I := \texttt{ncol}(\widetilde{\boldsymbol{V}}_I)$, shared by subdomains Ω^e and Ω^g is bounded by

$$0 \leq \tilde{s}_I \leq \min(p^e, p^g) - 6, \qquad I = \mathcal{T}(e,2) = \mathcal{T}(g,1). \tag{59}$$

If $\min(p^e, p^g) = 6$, i.e., if one of the domains have only 6 deformational modes, then the fictitious interface sharing the two domains cannot have any fluctuation mode ($\tilde{s}_I = 0$), and will move accordingly as a rigid body — or in other words, the *fictitious interface will remain unstrained* during the deformation of the contiguous subdomains.

For cases in which $\min(p^e, p^g) > 6$, on the other hand, one is confronted with the task of determining a matrix $\widetilde{\boldsymbol{V}}_I$ with $\tilde{s}_I$ columns, and of the form $\widetilde{\boldsymbol{V}}_I = \widetilde{\boldsymbol{W}}_I \boldsymbol{c}$, $\boldsymbol{c}$ being a matrix of coefficients. Not all choices of $\boldsymbol{c}$ are admissible, because, as demonstrated by the second author in Ref. [27] for the case of periodic structures, the column space of $\widetilde{\boldsymbol{V}}_I$ must contribute *effectively* to the work done by the interaction forces of both subdomains; this amounts to state that

$$\texttt{rank}(\widetilde{\boldsymbol{\Psi}}_{\mathbf{f}_2}^{e^T} \boldsymbol{D}_2^e \boldsymbol{V}_I) = \texttt{rank}(\widetilde{\boldsymbol{\Psi}}_{\mathbf{f}_1}^{g^T} \boldsymbol{D}_1^g \boldsymbol{V}_I) = 6 + \tilde{s}_I, \qquad I = \mathcal{T}(e,2) = \mathcal{T}(g,1), \tag{60}$$

where $\boldsymbol{V}_I = [\widehat{\boldsymbol{V}}_I, \widetilde{\boldsymbol{V}}_I]$. To meet the above conditions, we have adapted, to the case of general partitions, the selection method proposed in Ref. [27] for periodic structures; the involved operations for a interface Γ_I shared by subdomains Ω^e and Ω^g (so that $I = \mathcal{T}(e,2) = \mathcal{T}(g,1)$) are synthesized here by the function

$$\widetilde{\boldsymbol{V}}_I = \texttt{FLUCMODES}(\widetilde{\boldsymbol{\Phi}}_{\mathbf{f}_2}^e, \widetilde{\boldsymbol{\Phi}}_{\mathbf{f}_1}^g, \widetilde{\boldsymbol{\Psi}}_{\mathbf{f}_2}^e, \widetilde{\boldsymbol{\Psi}}_{\mathbf{f}_1}^g, \widehat{\boldsymbol{V}}_I, \bar{\boldsymbol{M}}_I, \boldsymbol{D}_2^e, \boldsymbol{D}_1^g, \epsilon_f), \tag{61}$$

described in Algorithm 3. In essence, the procedure parallels that employed in Box 5.1 for determining deformational modes, in the sense that the algorithm computes the fluctuation modes that *contribute the most to the work done by the interaction forces at the interface*. Lines 2 and 3 are the steps already outlined for determining the candidate interface modes $\widetilde{\boldsymbol{W}}_I$. In line 4, we compute the interaction force modes which are identical in both $\partial\Omega_2^e$ and $\partial\Omega_1^g$, and then determine the projection of these interaction modes ($\boldsymbol{U}$) onto the column space of the basis formed by the rigid-body modes $\widehat{\boldsymbol{V}}_I$ and the candidate fluctuation modes $\widetilde{\boldsymbol{W}}_I$ (lines 5, 6 and 7) — line 6 serves the purpose of ensuring that all modes contribute to the work done by the interaction forces, as demanded by conditions (60). Lastly, line 8 determines which is the component of $\boldsymbol{U}$ contained on the $span(\widetilde{\boldsymbol{W}}_I)$, and therewith the desired fluctuation modes matrix $\widetilde{\boldsymbol{V}}_I$.

7. Coarse-scale model

Now that we have at our disposal the basis matrices for rigid-body and deformational displacements, $\widehat{\boldsymbol{\Phi}}^e$ and $\widetilde{\boldsymbol{\Phi}}^e$, the resultant and self-equilibrated force modes, $\widehat{\boldsymbol{\Psi}}^e$ and $\widetilde{\boldsymbol{\Psi}}^e$ ($e = 1, 2 \ldots M$), as well as the displacement modes of each interface $\boldsymbol{V}_I = [\widehat{\boldsymbol{V}}_I, \widetilde{\boldsymbol{V}}_I]$ ($I = 1, 2 \ldots N$), we can proceed to the derivation of the (reduced-order) coarse-scale equations by substituting the modal expansions given in Eqs. (24) to (26), as well as their variations, in the variational Eqs. (18) to (20) . Exploiting the arbitrariness of $\delta\hat{\boldsymbol{q}}^e$, $\delta\tilde{\boldsymbol{q}}^e$, $\delta\hat{\boldsymbol{r}}^e$ and $\delta\tilde{\boldsymbol{r}}^e$, and making use of the variables defined in Eqs. (47) to (50), we obtain:

$$\widetilde{\boldsymbol{\Phi}}^{eT} \boldsymbol{F}_{int}^e(\tilde{\boldsymbol{q}}^e) - \widetilde{\boldsymbol{\Phi}}^{eT} \boldsymbol{F}_{ext}^e - \widetilde{\boldsymbol{\Phi}}^{eT} \left(\widehat{\boldsymbol{\Psi}}^e \hat{\boldsymbol{r}}^e + \widetilde{\boldsymbol{\Psi}}^e \tilde{\boldsymbol{r}}^e \right) = 0, \qquad e = 1, 2 \ldots M \tag{62}$$

Algorithm 3: Fluctuation modes of a given interface Γ_I (shared by domains Ω^e and Ω^g, so that $I = \mathcal{T}(e,2) = \mathcal{T}(g,1)$)

Function $\widetilde{\boldsymbol{V}}_I$ =FLUCMODES($\widetilde{\boldsymbol{\Phi}}^e_{\mathbf{f}_2}$, $\widetilde{\boldsymbol{\Phi}}^g_{\mathbf{f}_1}$, $\widetilde{\boldsymbol{\Psi}}^e_{\mathbf{f}_2}$, $\widetilde{\boldsymbol{\Psi}}^g_{\mathbf{f}_1}$, $\widehat{\boldsymbol{V}}_I$, $\bar{\boldsymbol{M}}_I$, $\boldsymbol{D}^e_2$, $\boldsymbol{D}^g_1$, ϵ_f):

Data: $\widetilde{\boldsymbol{\Phi}}^e_{\mathbf{f}_2}$, $\widetilde{\boldsymbol{\Psi}}^e_{\mathbf{f}_2} \in \mathbb{R}^{3l^e_2 \times p^e}$: deformational displacements and self-equilibrated interaction forces modes at $\partial\Omega^e_2$. $\widetilde{\boldsymbol{\Phi}}^g_{\mathbf{f}_1}$, $\widetilde{\boldsymbol{\Psi}}^g_{\mathbf{f}_1} \in \mathbb{R}^{3l^g_1 \times p^g}$: deformational displacements and self-equilibrated interaction forces modes at $\partial\Omega^g_1$ ($l^g_1 = l^e_2 = l_I$). $\boldsymbol{D}^e_2$, $\boldsymbol{D}^g_1 \in \mathbb{R}^{3l_I \times 3l_I}$: Matrices relating domain DOFs with fictitious interface DOFs (see Eq. (8)). $\widehat{\boldsymbol{V}}_I \in \mathbb{R}^{3l_I \times 6}$: rigid-body modes of Γ_I. $\bar{\boldsymbol{M}}_I \in \mathbb{R}^{3l_I \times 3l_I}$: geometric mass matrix of the interface Γ_I. $0 \le \epsilon_f \le 1$: tolerance for determining intersection of subspaces, typically $\epsilon_f \sim 10^{-3}$)

Result: $\widetilde{\boldsymbol{V}}_I \in \mathbb{R}^{3l_I \times \tilde{s}_I}$: Matrix of fluctuation modes (here $\tilde{s}_I \le \min(p^e, p^g) - 6$).

$\breve{\boldsymbol{\Phi}}^-_I \leftarrow \widetilde{\boldsymbol{\mathcal{P}}}_I \boldsymbol{D}^{e\,-1}_2 \widetilde{\boldsymbol{\Phi}}^e_{\mathbf{f}_2}$; $\breve{\boldsymbol{\Phi}}^+_I \leftarrow \widetilde{\boldsymbol{\mathcal{P}}}_I \boldsymbol{D}^{g\,-1}_1 \widetilde{\boldsymbol{\Phi}}^g_{\mathbf{f}_1}$ // Fluctuating component of deformational modes, see Eqs. (55) and (56). Projection operator $\widetilde{\boldsymbol{\mathcal{P}}}_I = \widetilde{\boldsymbol{\mathcal{P}}}_I(\widehat{\boldsymbol{V}}_I, \bar{\boldsymbol{M}}_I)$ is defined in Eq. (52).

$\widetilde{\boldsymbol{W}}_I \leftarrow$ INTS($\breve{\boldsymbol{\Phi}}^-_I$, $\breve{\boldsymbol{\Phi}}^+_I$, $\bar{\boldsymbol{M}}_I, \epsilon_f$) // Candidates for fluctuation modes (see Eq. (58) and Algorithm 2).

$\boldsymbol{A}_I \leftarrow$ INTS($\boldsymbol{D}^{e\,-1}_2 \widetilde{\boldsymbol{\Psi}}^e_{\mathbf{f}_2}$, $\boldsymbol{D}^{g\,-1}_1 \widetilde{\boldsymbol{\Psi}}^g_{\mathbf{f}_1}$, $\bar{\boldsymbol{M}}^{-1}_I, \epsilon_f$) // Intersection column spaces of interaction forces.

$\boldsymbol{G} \leftarrow [\widehat{\boldsymbol{V}}_I, \widetilde{\boldsymbol{W}}_I]^T \boldsymbol{A}_I$ // Coefficients projection interaction forces onto the column space of $[\widehat{\boldsymbol{V}}_I, \widetilde{\boldsymbol{W}}_I]$

$[\boldsymbol{v}, \bullet, \bullet] \leftarrow$ SVD($\boldsymbol{G}$) // SVD of the coefficients (to filter out modes not contributing to the work done by interaction forces)

$\boldsymbol{U} \leftarrow [\widehat{\boldsymbol{V}}_I, \widetilde{\boldsymbol{W}}_I]\boldsymbol{v}$ // Matrix whose column space is equal to the column space of the desired $\widetilde{\boldsymbol{V}}_I$

$\widetilde{\boldsymbol{V}}_I \leftarrow$ INTS($\boldsymbol{U}, \widetilde{\boldsymbol{W}}_I, \bar{\boldsymbol{M}}_I, \epsilon$) // We seek here the intersection of the column space of $\boldsymbol{U}$ and of the candidate modes $\widetilde{\boldsymbol{W}}_I$. Take $\epsilon \approx 0$ (say $\epsilon = 10^{-6}$), such that $\tilde{s}_I = \text{ncol}(\boldsymbol{A}_I)$.

$$\widehat{\boldsymbol{\Phi}}^{eT} \boldsymbol{F}^e_{int}(\tilde{\boldsymbol{q}}^e) - \widehat{\boldsymbol{\Phi}}^{eT} \boldsymbol{F}^e_{ext} - \widehat{\boldsymbol{\Phi}}^{eT} \left(\widehat{\boldsymbol{\Psi}}^e \hat{\boldsymbol{r}}^e + \widetilde{\boldsymbol{\Psi}}^e \tilde{\boldsymbol{r}}^e \right) = 0, \qquad e = 1, 2 \dots M \tag{63}$$

$$\widetilde{\boldsymbol{\Psi}}^{eT}_{\mathbf{f}} \left(\widehat{\boldsymbol{\Phi}}^e_{\mathbf{f}} \hat{\boldsymbol{q}}^e + \widetilde{\boldsymbol{\Phi}}^e_{\mathbf{f}} \tilde{\boldsymbol{q}}^e \right) - \widetilde{\boldsymbol{\Psi}}^{eT}_{\mathbf{f}} \boldsymbol{D}^e \boldsymbol{V}^e \boldsymbol{a}^e = 0, \qquad e = 1, 2 \dots M \tag{64}$$

$$\widehat{\boldsymbol{\Psi}}^{eT}_{\mathbf{f}} \left(\widehat{\boldsymbol{\Phi}}^e_{\mathbf{f}} \hat{\boldsymbol{q}}^e + \widetilde{\boldsymbol{\Phi}}^e_{\mathbf{f}} \tilde{\boldsymbol{q}}^e \right) - \widehat{\boldsymbol{\Psi}}^{eT}_{\mathbf{f}} \boldsymbol{D}^e \boldsymbol{V}^e \boldsymbol{a}^e = 0, \qquad e = 1, 2 \dots M \tag{65}$$

$$\delta \boldsymbol{a}^T \left(\sum_{e=1}^{M} \boldsymbol{L}^{eT} \boldsymbol{V}^{eT} \boldsymbol{D}^{eT} \left(\widehat{\boldsymbol{\Psi}}^e_{\mathbf{f}} \hat{\boldsymbol{r}}^e + \widetilde{\boldsymbol{\Psi}}^e_{\mathbf{f}} \tilde{\boldsymbol{r}}^e \right) - \sum_{I \in j_l} \bar{\boldsymbol{L}}^T_I \boldsymbol{V}^T_I \bar{\boldsymbol{F}}_I \right) = 0, \qquad \forall\, \delta \boldsymbol{a} \in \mathcal{V}. \tag{66}$$

Eqs. (62) and (63) are the equilibrium equations for each subdomain, while Eqs. (64) and (65) represent compatibility conditions between the subdomain interface boundaries and their corresponding fictitious interfaces. On the other hand, Eq. (66) is the variational equation corresponding to the equilibrium of the fictitious interfaces. Note that the variations of the global vector of coarse-scale DOFs are constrained to lie in an (as yet) unspecified test space $\mathcal{V} \subset \mathbb{R}^s$, where $s := \sum_{I=1}^{N} s_I$ is the total number of coarse-scale DOFs.

For notational compactness, it proves convenient to define the following reduced-order matrices:

$$\widehat{\boldsymbol{H}}^e := \widehat{\boldsymbol{\Psi}}^{eT} \widetilde{\boldsymbol{\Phi}}^e = \widehat{\boldsymbol{\Psi}}^{eT}_{\mathbf{f}_1} \widetilde{\boldsymbol{\Phi}}^e_{\mathbf{f}_1} + \widehat{\boldsymbol{\Psi}}^{eT}_{\mathbf{f}_2} \widetilde{\boldsymbol{\Phi}}^e_{\mathbf{f}_2}, \qquad e = 1, 2 \dots M \tag{67}$$

$$\widehat{\boldsymbol{G}}^e := \widehat{\boldsymbol{\Psi}}^{eT} \widehat{\boldsymbol{\Phi}}^e = \widehat{\boldsymbol{\Psi}}^{eT}_{\mathbf{f}_1} \widehat{\boldsymbol{\Phi}}^e_{\mathbf{f}_1} + \widehat{\boldsymbol{\Psi}}^{eT}_{\mathbf{f}_2} \widehat{\boldsymbol{\Phi}}^e_{\mathbf{f}_2}, \qquad e = 1, 2 \dots M \tag{68}$$

$$\boldsymbol{T}^e := \widetilde{\boldsymbol{\Psi}}^{eT}_{\mathbf{f}} \boldsymbol{D}^e \boldsymbol{V}^e = \begin{bmatrix} \widetilde{\boldsymbol{\Psi}}^{eT}_{\mathbf{f}_1} \boldsymbol{D}^e_1 \boldsymbol{V}^e_1 & \widetilde{\boldsymbol{\Psi}}^{eT}_{\mathbf{f}_2} \boldsymbol{D}^e_2 \boldsymbol{V}^e_2 \end{bmatrix}, \qquad e = 1, 2 \dots M \tag{69}$$

$$\widehat{\boldsymbol{T}}^e := \widehat{\boldsymbol{\Psi}}^{eT}_{\mathbf{f}} \boldsymbol{D}^e \boldsymbol{V}^e = \begin{bmatrix} \widehat{\boldsymbol{\Psi}}^{eT}_{\mathbf{f}_1} \boldsymbol{D}^e_1 \boldsymbol{V}^e_1 & \widehat{\boldsymbol{\Psi}}^{eT}_{\mathbf{f}_2} \boldsymbol{D}^e_2 \boldsymbol{V}^e_2 \end{bmatrix}, \qquad e = 1, 2 \dots M. \tag{70}$$

With these matrices at hand, (along with $\boldsymbol{H}^e$, defined previously in Eq. (42)), and taking into account that $\widehat{\boldsymbol{\Phi}}^{eT} \boldsymbol{F}^e_{int} = \boldsymbol{0}$ (the work done by internal forces over rigid-body displacements is zero) and $\widehat{\boldsymbol{\Phi}}^{eT} \widetilde{\boldsymbol{\Psi}}^e = \boldsymbol{0}$ (condition of self-equilibrating force, see Eq. (39)), Eqs. (62) to (66) adopt the form

$$\widetilde{\boldsymbol{\Phi}}^{eT} \boldsymbol{F}^e_{int}(\tilde{\boldsymbol{q}}^e) - \widetilde{\boldsymbol{\Phi}}^{eT} \boldsymbol{F}^e_{ext} - \left(\widehat{\boldsymbol{H}}^{eT} \hat{\boldsymbol{r}}^e + \boldsymbol{H}^{eT} \tilde{\boldsymbol{r}}^e \right) = 0, \qquad e = 1, 2 \dots M \tag{71}$$

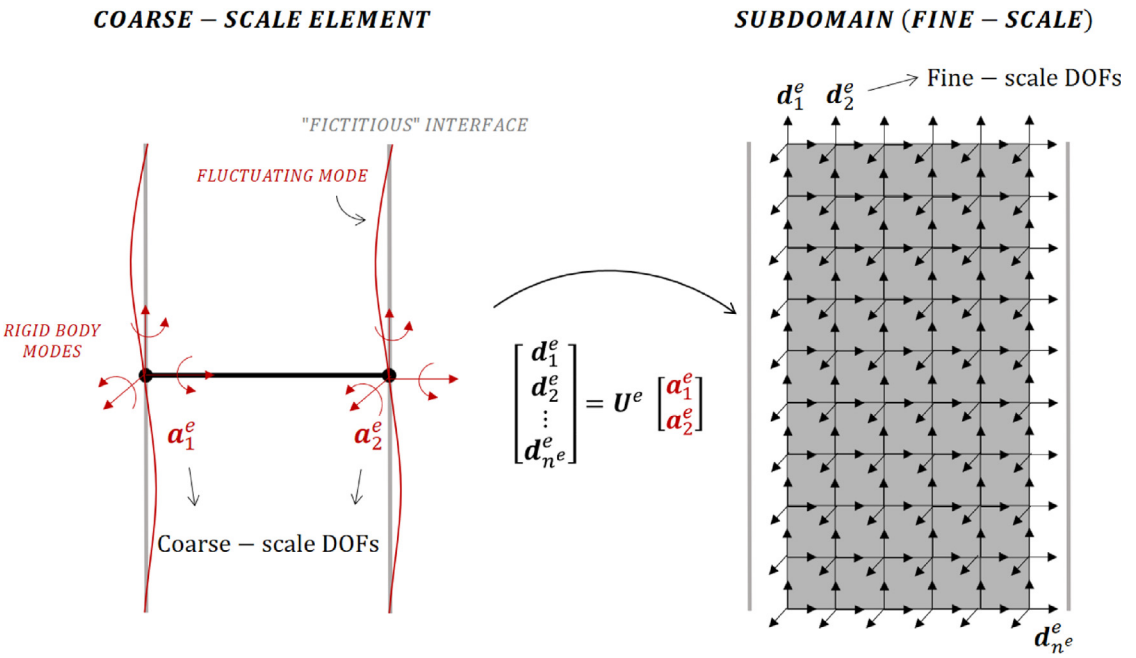

Fig. 3. Graphical description of the downscaling ("coarse-to-fine") matrix $\boldsymbol{U}^e$ of a given subdomain Ω^e (defined in Eq. (80)). This matrix maps the vector of coarse-scale DOFs ($\boldsymbol{a}^e = [\boldsymbol{a}_1^{eT}, \boldsymbol{a}_2^{eT}]^T$) onto its fine-scale counterpart ($\boldsymbol{d}^e = [\boldsymbol{d}_1^{eT}, \boldsymbol{d}_2^{eT}, \dots \boldsymbol{d}_{n^e}^{eT}]^T$), where $\boldsymbol{d}_i^e \in \mathbb{R}^3$ is the nodal displacement at the ith fine-scale node. The transpose of this matrix, $\boldsymbol{U}^{eT}$, on the other hand, acts as upscaling ("fine-to-coarse") operator for external forces, see Eq. (94).

$$-\widehat{\boldsymbol{\Phi}}^{eT}\boldsymbol{F}_{ext}^e - \widehat{\boldsymbol{G}}^{eT}\hat{\boldsymbol{r}}^e = 0, \qquad e = 1, 2 \dots M \tag{72}$$

$$\boldsymbol{H}^e\tilde{\boldsymbol{q}}^e - \boldsymbol{T}^e\boldsymbol{a}^e = 0, \qquad e = 1, 2 \dots M \tag{73}$$

$$\widehat{\boldsymbol{G}}^e\hat{\boldsymbol{q}}^e + \widehat{\boldsymbol{H}}^e\tilde{\boldsymbol{q}}^e - \widehat{\boldsymbol{T}}^e\boldsymbol{a}^e = 0, \qquad e = 1, 2 \dots M \tag{74}$$

$$\delta\boldsymbol{a}^T\left(\sum_{e=1}^{M}\boldsymbol{L}^{eT}\left(\boldsymbol{T}^{eT}\tilde{\boldsymbol{r}}^e + \widehat{\boldsymbol{T}}^{eT}\hat{\boldsymbol{r}}^e\right) - \sum_{I\in j_I}\bar{\boldsymbol{L}}_I^T\boldsymbol{V}_I^T\bar{\boldsymbol{F}}_I\right) = 0, \qquad \forall\,\delta\boldsymbol{a} \in \mathcal{V}. \tag{75}$$

7.1. Downscaling "coarse-to-fine" operator

In the system of Eqs. (71) to (75), there are four set of variables at subdomain level ($\tilde{\boldsymbol{q}}^e$, $\hat{\boldsymbol{q}}^e$, $\tilde{\boldsymbol{r}}^e$, $\hat{\boldsymbol{r}}^e$) and one global variable $\boldsymbol{a} \in \mathbb{R}^s$ (the vector of coarse-scale DOFs). We demonstrate in what follows that, since $\boldsymbol{H}^e \in \mathbb{R}^{p^e\times p^e}$ is invertible by construction for all domains Ω^e (see Box 5.1), it is possible to arrive at a *coarse-scale equilibrium equation* solely in terms of the vector of coarse-scale DOFs $\boldsymbol{a}$.

We begin our demonstration by showing that, for all domains $e = 1, 2 \dots M$, there is a downscaling, "coarse-to-fine" operator $\boldsymbol{U}^e \in \mathbb{R}^{3n^e\times s^e}$, graphically represented in Fig. 3. Indeed, as $\boldsymbol{H}^e$ is invertible, we can solve the compatibility equation (73) for $\tilde{\boldsymbol{q}}^e$:

$$\tilde{\boldsymbol{q}}^e = \boldsymbol{H}^{e^{-1}}\boldsymbol{T}^e\boldsymbol{a}^e, \qquad e = 1, 2 \dots M. \tag{76}$$

If we next replace the preceding equation into the other compatibility expression, see Eq. (74), we get, upon factoring the terms multiplying $\boldsymbol{a}^e$:

$$\widehat{\boldsymbol{G}}^e\hat{\boldsymbol{q}}^e + \left(\widehat{\boldsymbol{H}}^e\boldsymbol{H}^{e^{-1}}\boldsymbol{T}^e - \widehat{\boldsymbol{T}}^e\right)\boldsymbol{a}^e = 0, \qquad e = 1, 2 \dots M. \tag{77}$$

From Eq. (68) and Eq. (35), it follows that $\widehat{\boldsymbol{G}}^e \in \mathbb{R}^{6\times 6}$ is a geometric matrix that depends on the area and moment of inertia of the subdomain interfaces; it can be readily shown that this matrix is invariably invertible, and therefore

Eq. (77) can be solved for $\hat{\boldsymbol{q}}^e$, leading to

$$\hat{\boldsymbol{q}}^e = \widehat{\boldsymbol{G}}^{e-1}\left(\widehat{\boldsymbol{T}}^e - \widehat{\boldsymbol{H}}^e \boldsymbol{H}^{e^{-1}} \boldsymbol{T}^e\right)\boldsymbol{a}^e, \qquad e = 1, 2 \dots M. \tag{78}$$

Inserting Eq. (76) and Eq. (78) into Eq. (24), and factoring out $\boldsymbol{a}^e$, we finally arrive at the desired downscaling operator $\boldsymbol{U}^e$:

$$\boldsymbol{d}^e = \boldsymbol{U}^e \boldsymbol{a}^e = \begin{bmatrix}\boldsymbol{U}_1^e & \boldsymbol{U}_2^e\end{bmatrix}\begin{bmatrix}\boldsymbol{a}_1^e \\ \boldsymbol{a}_2^e\end{bmatrix}, \qquad e = 1, 2 \dots M \tag{79}$$

where

$$\boldsymbol{U}_i^e := \widetilde{\boldsymbol{U}}_i^e + \widehat{\boldsymbol{U}}_i^e, \qquad e = 1, 2 \dots M, \quad i = 1, 2; \tag{80}$$

and

$$\widetilde{\boldsymbol{U}}_i^e = \widetilde{\boldsymbol{\Phi}}^e \widetilde{\boldsymbol{P}}_i^e, \qquad e = 1, 2 \dots M, \quad i = 1, 2, \tag{81}$$

$$\widehat{\boldsymbol{U}}_i^e = \widehat{\boldsymbol{\Phi}}^e \widehat{\boldsymbol{P}}_i^e, \qquad e = 1, 2 \dots M, \quad i = 1, 2, \tag{82}$$

$$\widetilde{\boldsymbol{P}}_i^e = \boldsymbol{H}^{e^{-1}} \boldsymbol{T}_i^e, \qquad e = 1, 2 \dots M, \quad i = 1, 2, \tag{83}$$

$$\widehat{\boldsymbol{P}}_i^e = \widehat{\boldsymbol{G}}^{e-1}\left(\widehat{\boldsymbol{T}}_i^e - \widehat{\boldsymbol{H}}^e \boldsymbol{H}^{e^{-1}} \boldsymbol{T}_i^e\right), \qquad e = 1, 2 \dots M, \quad i = 1, 2. \tag{84}$$

As can be seen in Eq. (80), the downscaling operator $\boldsymbol{U}_i^e$ at the coarse-scale node i (i=1,2) is the sum of two matrices, one corresponding to the deformational component, $\widetilde{\boldsymbol{U}}_i^e$, defined in Eq. (81), and another one corresponding to the rigid-body component, $\widehat{\boldsymbol{U}}_i^e$ defined in Eq. (82). In both cases the operators are the product of the corresponding basis matrix (deformational $\widetilde{\boldsymbol{\Phi}}^e \in \mathbb{R}^{3n^e \times p^e}$ and rigid-body $\widehat{\boldsymbol{\Phi}}^e \in \mathbb{R}^{3n^e \times 6}$), and a reduced-order matrix, independent of the size of the underlying mesh, namely $\widetilde{\boldsymbol{P}}_i^e \in \mathbb{R}^{p^e \times s_i^e}$ in Eq. (83) and $\widehat{\boldsymbol{P}}_i^e \in \mathbb{R}^{6 \times s_i^e}$ in Eq. (84).

7.2. Coarse-scale residual vector

We move now to the subdomain equilibrium equation (72); solving this equation for $\hat{\boldsymbol{r}}^e$, we obtain:

$$\hat{\boldsymbol{r}}^e = -\widehat{\boldsymbol{G}}^{e-T} \widehat{\boldsymbol{\Phi}}^{eT} \boldsymbol{F}_{\boldsymbol{ext}}^e, \qquad e = 1, 2 \dots M. \tag{85}$$

Replacing both the above equation and Eq. (76) into Eqs. (71) and (75), we get, upon rearrangement:

$$\widetilde{\boldsymbol{\Phi}}^{eT} \boldsymbol{F}_{\boldsymbol{int}}^e(\boldsymbol{a}^e) - \left(\widetilde{\boldsymbol{\Phi}}^{eT} - \widehat{\boldsymbol{H}}^{eT} \widehat{\boldsymbol{G}}^{e-T} \widehat{\boldsymbol{\Phi}}^{eT}\right) \boldsymbol{F}_{\boldsymbol{ext}}^e - \boldsymbol{H}^{eT} \tilde{\boldsymbol{r}}^e = 0, \qquad e = 1, 2 \dots M \tag{86}$$

$$\delta \boldsymbol{a}^T \left(\sum_{e=1}^{M} \boldsymbol{L}^{eT} \left(\boldsymbol{T}^{eT} \tilde{\boldsymbol{r}}^e - (\widehat{\boldsymbol{T}}^{eT} \widehat{\boldsymbol{G}}^{e-T} \widehat{\boldsymbol{\Phi}}^{eT}) \boldsymbol{F}_{\boldsymbol{ext}}^e \right) - \sum_{I \in j_I} \bar{\boldsymbol{L}}_I^T \boldsymbol{V}_I^T \bar{\boldsymbol{F}}_I \right) = 0, \qquad \forall\, \delta \boldsymbol{a} \in \mathcal{V}. \tag{87}$$

The above system of equations only depends on the amplitude of the self-equilibrated modes $\tilde{\boldsymbol{r}}^e$ ($e = 1, 2 \dots M$) and on the coarse-scale DOFs vector $\boldsymbol{a}$. Thus, to arrive at the desired coarse-scale equilibrium equation in terms solely of $\boldsymbol{a}$, we have to eliminate $\tilde{\boldsymbol{r}}^e$ from the above system of equations. This can be done by firstly solving Eq. (86) for $\tilde{\boldsymbol{r}}^e$, and then inserting the resulting expression into Eq. (87). By using the definitions of the downscaling operators $\boldsymbol{U}^e$ and $\widetilde{\boldsymbol{U}}^e$, given previously in Eqs. (80) and (81), and after some straightforward (but lengthy) manipulation, it can be shown that the coarse-scale variational equilibrium equation can be written as

$$\delta \boldsymbol{a}^T \boldsymbol{R}^*(\boldsymbol{a}) = 0, \qquad \forall\, \delta \boldsymbol{a} \in \mathcal{V}, \tag{88}$$

where the *coarse-scale residual vector* $\boldsymbol{R}^* \in \mathbb{R}^s$ is given by

$$\boldsymbol{R}^*(\boldsymbol{a}) := \overbrace{\boldsymbol{F}_{\boldsymbol{int}}^*(\boldsymbol{a})}^{\text{Coarse-scale internal forces}} - \overbrace{(\boldsymbol{F}_{\boldsymbol{ext}}^* + \bar{\boldsymbol{F}}^*)}^{\text{Coarse-scale external forces}}. \tag{89}$$

For the reader's convenience, the definitions of the coarse-scale internal forces ($\boldsymbol{F}_{\boldsymbol{int}}^*$) and the coarse-scale external forces ($\boldsymbol{F}_{\boldsymbol{ext}}^*$ and $\bar{\boldsymbol{F}}^*$) appearing in the above equation are given in Box 7.1.

1. Coarse-scale vector of internal forces

$$\boldsymbol{F}^{*}_{\boldsymbol{int}}(\boldsymbol{a}) = \sum_{e=1}^{M} \boldsymbol{L}^{eT} \boldsymbol{F}^{*e}_{\boldsymbol{int}}(\boldsymbol{a}^{e}) \tag{90}$$

where $\boldsymbol{L}^{e}$ is the Boolean (assembly) operator defined in Eq. (50), while $\boldsymbol{F}^{*e}_{\boldsymbol{int}}$ is the contribution to $\boldsymbol{F}^{*}_{\boldsymbol{int}}$ of domain Ω^{e}, which in turn is given by

$$\boldsymbol{F}^{*e}_{\boldsymbol{int}} := \widetilde{\boldsymbol{U}}^{eT} \boldsymbol{F}^{e}_{\boldsymbol{int}} = \widetilde{\boldsymbol{P}}^{eT} \boldsymbol{\mathcal{F}}^{e}_{int} = \begin{bmatrix} \widetilde{\boldsymbol{P}}^{eT}_{1} \boldsymbol{\mathcal{F}}^{e}_{int} \\ \widetilde{\boldsymbol{P}}^{eT}_{2} \boldsymbol{\mathcal{F}}^{e}_{int} \end{bmatrix}, \qquad e = 1, 2 \dots M, \tag{91}$$

where

$$\boldsymbol{\mathcal{F}}^{e}_{int} := \widetilde{\boldsymbol{\Phi}}^{eT} \boldsymbol{F}^{e}_{\boldsymbol{int}}, \qquad e = 1, 2 \dots M \tag{92}$$

($\widetilde{\boldsymbol{P}}^{eT}$ was defined in Eq.(83)).

2. Coarse-scale vector of body/lateral forces

$$\boldsymbol{F}^{*}_{\boldsymbol{ext}} = \sum_{e=1}^{M} \boldsymbol{L}^{eT} \boldsymbol{F}^{*e}_{\boldsymbol{ext}} \tag{93}$$

where

$$\boldsymbol{F}^{*e}_{\boldsymbol{ext}} := \boldsymbol{U}^{eT} \boldsymbol{F}^{e}_{\boldsymbol{ext}} = \begin{bmatrix} \widetilde{\boldsymbol{P}}^{eT}_{1} \widetilde{\boldsymbol{\mathcal{F}}}^{e}_{ext} \\ \widetilde{\boldsymbol{P}}^{eT}_{2} \widetilde{\boldsymbol{\mathcal{F}}}^{e}_{ext} \end{bmatrix} + \begin{bmatrix} \widehat{\boldsymbol{P}}^{eT}_{1} \widehat{\boldsymbol{\mathcal{F}}}^{e}_{ext} \\ \widehat{\boldsymbol{P}}^{eT}_{2} \widehat{\boldsymbol{\mathcal{F}}}^{e}_{ext} \end{bmatrix}, \qquad e = 1, 2 \dots M \tag{94}$$

and

$$\widetilde{\boldsymbol{\mathcal{F}}}^{e}_{ext} := \widetilde{\boldsymbol{\Phi}}^{eT} \boldsymbol{F}^{e}_{\boldsymbol{ext}}; \qquad \widehat{\boldsymbol{\mathcal{F}}}^{e}_{ext} := \widehat{\boldsymbol{\Phi}}^{eT} \boldsymbol{F}^{e}_{\boldsymbol{ext}}, \qquad e = 1, 2 \dots M \tag{95}$$

($\widehat{\boldsymbol{\mathcal{F}}}^{e}_{ext} \in \mathbb{R}^{6}$ is thus the vector of resultants and moment resultants, with respect to the centroid of the domain, of the FE external forces $\boldsymbol{F}^{e}_{\boldsymbol{ext}}$).

3. Coarse-scale vector of traction loads (which is only nonzero at the DOFs of the fictitious interface Γ_{I}, $I \in \boldsymbol{j}_{\boldsymbol{I}}$, where surface traction loads are imposed):

$$\bar{\boldsymbol{F}}^{*} = \sum_{I \in \boldsymbol{j}_{\boldsymbol{I}}} \bar{\boldsymbol{L}}^{T}_{I} \bar{\boldsymbol{F}}^{*}_{I}, \qquad \text{where} \qquad \bar{\boldsymbol{F}}^{*}_{I} := \boldsymbol{V}_{I}{}^{T} \bar{\boldsymbol{F}}_{I}. \tag{96}$$

Notice that the first 6 entries of $\bar{\boldsymbol{F}}^{*}_{I}$ are the resultants and moment resultants of the nodal forces applied on the boundary interface Γ_{I}.

Box 7.1: Coarse-scale nodal forces in terms of its fine-scale counterparts.

Remark 7.1. Inspection of Eq. (91) and Eq. (94) in Box 7.1 reveal that the transpose of the displacement downscaling operators $\widetilde{\boldsymbol{U}}^{e}$ and $\boldsymbol{U}^{e}$ play the role of upscaling (fine-to-coarse) operators for the nodal internal forces and body/lateral external forces, respectively.

7.3. Dirichlet boundary conditions

The coarse-scale prescribed displacements $\boldsymbol{a}_{I} \in \mathbb{R}^{s_{I}}$ at the end node $I \in \boldsymbol{j}_{\boldsymbol{r}}$ may be determined from its fine-scale counterpart $\bar{\boldsymbol{v}}_{I}$ (specified in the parameterization of the problem, see expression (11)) by solving the least-squares problem $\min_{\boldsymbol{a}_{I}} \|\boldsymbol{V}_{I}\boldsymbol{a}_{I} - \bar{\boldsymbol{v}}_{I}\|_{\bar{\boldsymbol{M}}_{I}}$; the solution of this problem reads

$$\boldsymbol{a}_{I} = (\boldsymbol{V}_{I}^{T} \bar{\boldsymbol{M}}_{I} \boldsymbol{V}_{I})^{-1} \boldsymbol{V}_{I}^{T} \bar{\boldsymbol{M}}_{I} \bar{\boldsymbol{v}}_{I}, \qquad I \in \boldsymbol{j}_{\boldsymbol{r}}. \tag{97}$$

If the prescribed displacement is of the form $\bar{\boldsymbol{v}}_I = \widehat{\boldsymbol{V}}_I \boldsymbol{\alpha}_I$, with $\boldsymbol{\alpha}_I \in \mathbb{R}^6$, then, by virtue of the orthogonality between rigid-body modes $\widehat{\boldsymbol{V}}_I$ and fluctuation modes $\widetilde{\boldsymbol{V}}_I$ (see Eq. (29)), it follows from Eq. (97) that

$$\boldsymbol{a}_I = \begin{bmatrix} \widehat{\boldsymbol{a}}_I \\ \widetilde{\boldsymbol{a}}_I \end{bmatrix} = \begin{bmatrix} \boldsymbol{\alpha}_I \\ \boldsymbol{0} \end{bmatrix}, \qquad I \in \boldsymbol{j}_{\boldsymbol{r}}. \tag{98}$$

Denoting by $\mathbf{r} \subset \{1, 2 \dots s\}$ the list of prescribed coarse-scale DOFs, and by $\mathbf{l}$ its complementary set, we can state that the space of test displacements $\mathcal{V}$ appearing in the variational equation (88) is given by all $\delta\boldsymbol{a} \in \mathbb{R}^s$ of the form $\delta\boldsymbol{a}_{\mathbf{r}} = \boldsymbol{0}$ and $\delta\boldsymbol{a}_{\mathbf{l}}$ arbitrary. The nonlinear coarse-scale equilibrium problem may thus be formulated as follows: given the input parameter $\boldsymbol{\mu} \in \mathcal{D}$, find $\boldsymbol{a} \in \mathbb{R}^s$, with $\boldsymbol{a}_{\mathbf{r}}(\boldsymbol{\mu}) = \boldsymbol{\alpha}(\boldsymbol{\mu})$, such that

$$\boldsymbol{R}^*_{\mathbf{l}}(\boldsymbol{a}; \boldsymbol{\mu}) = \boldsymbol{0}. \tag{99}$$

7.4. Tangent stiffness matrix

The expression for the coarse-scale, tangent stiffness matrix may be deduced from Eqs. (79) and Eq. (90) as follows:

$$\boldsymbol{K}^* := \frac{\partial \boldsymbol{F}^*_{int}}{\partial \boldsymbol{a}} = \sum_{e=1}^{M} \boldsymbol{L}^{e^T} \boldsymbol{K}^{*e} \boldsymbol{L}^e \tag{100}$$

where

$$\boldsymbol{K}^{*e} := \frac{\partial \boldsymbol{F}^{*e}_{int}}{\partial \boldsymbol{a}^e} = \widetilde{\boldsymbol{U}}^{e^T} \boldsymbol{K}^e \widetilde{\boldsymbol{U}}^e, \qquad e = 1, 2 \dots M, \tag{101}$$

$\boldsymbol{K}^e$ being the standard FE tangent stiffness matrix of domain Ω^e:

$$\boldsymbol{K}^e := \frac{\partial \boldsymbol{F}^e_{int}}{\partial \boldsymbol{d}^e}, \qquad e = 1, 2 \dots M. \tag{102}$$

This expression can be further expanded by using Eq. (91); this leads to

$$\boldsymbol{K}^{*e} = \begin{bmatrix} \widetilde{\boldsymbol{P}}^{e^T}_1 \mathcal{K}^e \widetilde{\boldsymbol{P}}^e_1 & \widetilde{\boldsymbol{P}}^{e^T}_1 \mathcal{K}^e \widetilde{\boldsymbol{P}}^e_2 \\ \widetilde{\boldsymbol{P}}^{e^T}_2 \mathcal{K}^e \widetilde{\boldsymbol{P}}^e_1 & \widetilde{\boldsymbol{P}}^{e^T}_2 \mathcal{K}^e \widetilde{\boldsymbol{P}}^e_2 \end{bmatrix}, \qquad e = 1, 2 \dots M, \tag{103}$$

where

$$\mathcal{K}^e := \widetilde{\boldsymbol{\Phi}}^{e^T} \boldsymbol{K}^e \widetilde{\boldsymbol{\Phi}}^e, \qquad e = 1, 2 \dots M. \tag{104}$$

It should be noticed that the sub-matrices in Eq. (103) have by construction full rank. Indeed, by using Eq. (83), we can write the sub-matrices in Eq. (103) as

$$\boldsymbol{K}^{*e}_{ij} = \widetilde{\boldsymbol{P}}^{e^T}_i \mathcal{K}^e \widetilde{\boldsymbol{P}}^e_j = \boldsymbol{T}^{e^T}_i (\boldsymbol{H}^{e^{-T}} \mathcal{K}^e \boldsymbol{H}^{e^{-1}}) \boldsymbol{T}^e_j, \qquad e = 1, 2 \dots M; \quad i = 1, 2; \quad j = 1, 2. \tag{105}$$

The parenthetical term has full rank because both $\mathcal{K}^e \in \mathbb{R}^{p^e \times p^e}$ and $\boldsymbol{H}^e \in \mathbb{R}^{p^e \times p^e}$ are full rank — the former thanks to the deformational character of the basis matrices $\widetilde{\boldsymbol{\Phi}}^e$, and the latter because by construction, see Box 5.1, it is an invertible matrix. On the other hand, $\boldsymbol{T}^e_i \in \mathbb{R}^{p^e \times s^e_i}$, whose expression is given in Eq. (69), is also a full rank matrix by virtue of condition (60).

7.5. Hyperreduction

Examination of the coarse-scale nodal force vectors defined in Box 7.1 indicates that the computational complexity of the problem still scales with the size of the underlying finite element mesh. More specifically, the computational bottlenecks are present in the evaluation of $\boldsymbol{\mathcal{F}}^e_{int}$ in Eq. (92), which is involved in the construction of the coarse-scale internal forces, and the terms $\widetilde{\boldsymbol{\mathcal{F}}}^e_{ext}$, $\widehat{\boldsymbol{\mathcal{F}}}^e_{ext}$ in Eq. (95); and $\bar{\boldsymbol{F}}^*_I$ in Eq. (96), which are involved in the construction of the coarse-scale external forces.

In the latter case, since $\widetilde{\boldsymbol{\mathcal{F}}}^e_{ext}$, $\widehat{\boldsymbol{\mathcal{F}}}^e_{ext}$ and $\bar{\boldsymbol{F}}^*_I$ are by hypothesis independent of the nodal displacements, one can overcome the bottleneck by introducing a separate parametric representation of the corresponding nodal force vector,

and then precomputing the projection of the corresponding spatial patterns. For instance, if we express the vector of fine-scale external/lateral nodal forces as

$$\boldsymbol{F}^e_{\boldsymbol{ext}}(\boldsymbol{\mu}) = \boldsymbol{\Lambda}^e\,\boldsymbol{\beta}(\boldsymbol{\mu}), \qquad e = 1, 2 \dots M, \tag{106}$$

(here $\boldsymbol{\Lambda}^e$ is the matrix of force patterns), and then insert the above into Eq. (95), we get

$$\widetilde{\boldsymbol{\mathcal{F}}}^e_{ext} = (\widetilde{\boldsymbol{\Phi}}^{e^T}\boldsymbol{\Lambda}^e)\boldsymbol{\beta}(\boldsymbol{\mu}); \qquad \widehat{\boldsymbol{\mathcal{F}}}^e_{ext} = (\widehat{\boldsymbol{\Phi}}^{e^T}\boldsymbol{\Lambda}^e)\boldsymbol{\beta}(\boldsymbol{\mu}), \qquad e = 1, 2 \dots M. \tag{107}$$

The matrices $\widetilde{\boldsymbol{\Phi}}^{e^T}\boldsymbol{\Lambda}^e$ and $\widehat{\boldsymbol{\Phi}}^{e^T}\boldsymbol{\Lambda}^e$ may be precomputed in the offline stage, and, in doing so, the operation count for the evaluation of the coarse-scale vector $\boldsymbol{F}^*_{\boldsymbol{ext}}$ in the online stage becomes independent of the size of the finite element mesh of each subdomain Ω^e.

The above described methodology, however, cannot be used for the internal force term $\boldsymbol{\mathcal{F}}^e_{int}$, since the vector of FE nodal internal forces $\boldsymbol{F}^e_{\boldsymbol{int}}$ bears in general a nonlinear relationship to the nodal displacements $\boldsymbol{d}^e$ (and therefore to the input parameter $\boldsymbol{\mu}$). To evaluate the term $\boldsymbol{\mathcal{F}}^e_{int}$ in an efficient, mesh-independent manner, we shall use the *hyperreduction* approach proposed by the second author in Ref. [27], which essentially consists in finding an optimal cubature (i.e., 3-dimensional quadrature) for the projected internal forces. Indeed, the expression for the projected internal forces $\boldsymbol{\mathcal{F}}^e_{int}$ in terms of the Cauchy stress vector $\boldsymbol{\sigma} \in \mathbb{R}^6$ is given by

$$\boldsymbol{\mathcal{F}}^e_{int} = \widetilde{\boldsymbol{\Phi}}^{e^T}\boldsymbol{F}^e_{\boldsymbol{int}} = \widetilde{\boldsymbol{\Phi}}^{e^T}\int_{\Omega^e}\boldsymbol{B}^{e^T}\boldsymbol{\sigma}\;d\Omega = \int_{\Omega^e}(\boldsymbol{B}^e\widetilde{\boldsymbol{\Phi}}^e)^T\boldsymbol{\sigma}\;d\Omega, \qquad e = 1, 2 \dots M, \tag{108}$$

where $\boldsymbol{B}^e : \Omega^e \times \mathbb{R}^{6\times 3n^e}$ denotes the global FE strain–displacement matrix relating the (infinitesimal) strain vector $\boldsymbol{\varepsilon} \in \mathbb{R}^6$ to the vector of nodal displacements $\boldsymbol{d}^e$ (i.e: $\boldsymbol{\varepsilon} = \boldsymbol{B}^e\boldsymbol{d}^e$). Thus, the integrand in Eq. (108) is the product of two functions: $\boldsymbol{B}\,\widetilde{\boldsymbol{\Phi}}^e$, which lies in a subspace of dimension equal to the number of deformational modes, p^e, and the Cauchy stresses, which if the constitutive relationship is moderately nonlinear, lives in a subspace of dimension $\gamma^e \sim \mathcal{O}(p^e)$. This implies that the integrand resides in a subspace of dimension $\mathcal{O}(p^{e^2})$, and therefore, $c^e \sim \mathcal{O}(p^{e^2})$ points should suffice for accurately evaluating the integral. For instance, it is shown in Ref. [27] that, if the problem is linear, and therefore, $\gamma^e = p^e$, $\boldsymbol{\mathcal{F}}^e_{int}$ can be exactly evaluated using a cubature rule with $c^e = (p^e+1)p^e/2$ points.

The selection of the integration points (among the set of Gauss points of the mesh of each domain) is carried out here by the[7] *Empirical Cubature Method* (ECM), proposed by the second author in Ref. [30], and further refined in [27]. The method takes as inputs the matrix of stress snapshots $\boldsymbol{A}^e_{\boldsymbol{\sigma}}$ defined in Eq. (22) — from which it determines a basis matrix for stresses $\boldsymbol{\Theta}^e \in \mathbb{R}^{6m^e_{gs}\times\gamma^e}$ using the SVD —, the deformational basis matrix $\widetilde{\boldsymbol{\Phi}}^e$, as well as information of the underlying FE mesh of each subdomain Ω^e (such as the Gauss weights); and returns a reduced set of integration points (with indexes $\boldsymbol{Z}^e \subset \{1, 2 \dots m^e_{gs}\}$), along with their associated *positive* weights $\{\omega_g\}_{g=1}^{c^e}$. The reader interested in the details of the selection procedure is referred to Ref. [27], appendix A. It should be pointed that the determination of the points and positive weights may be also conducted by the Empirical Quadrature Method proposed by Patera and co-workers in [36] (Patera's method is based on linear programming, while the ECM relies on sequential least-squares minimization steps).

Once the set of points and positive weights have been computed for each subdomain (in the offline stage), the vector of coarse-scale internal forces at the ith node ($i = 1, 2$) of element e, see Eq. (91), can be efficiently calculated in the online stage by as a weighted sum of the integrand at the selected points $\boldsymbol{Z}^e$, i.e.:

$$\boldsymbol{F}^{*e}_{\boldsymbol{int}\,i} = \sum_{g=1}^{c^e}\omega^e_g(\boldsymbol{B}^{*e^T}_i\boldsymbol{\sigma})_{\boldsymbol{Z}^e(g)}, \qquad i = 1, 2; \quad e = 1, 2 \dots M, \tag{109}$$

where the notation $(\bullet)_{\boldsymbol{Z}^e(g)}$ means that the variable is evaluated at the $\boldsymbol{Z}^e(g)$-th Gauss point of the mesh, whereas

$$\boldsymbol{B}^{*e}_i := \boldsymbol{B}^e\widetilde{\boldsymbol{U}}^e_i, \qquad e = 1, 2 \dots M, \quad i = 1, 2. \tag{110}$$

This matrix may be regarded as an "inter-scale" strain–displacement matrix, for it maps the *coarse-scale* nodal displacements of node i ($\boldsymbol{a}^e_i$) onto the *fine-scale* strains $\boldsymbol{\varepsilon}$ at a given point of the domain. Likewise, for the

[7] Conceptually, the ECM is akin to the Discrete Empirical Interpolation Method (DEIM) [35]. In fact, the DEIM may be used as well to approximate the vector of internal forces. However, we favor the ECM because, as argued in [30], it ensures that the resulting reduced-order stiffness matrix inherits the spectral properties (positive definiteness) of its full-order counterpart.

coarse-scale tangent stiffness matrix (see Eq. (103)), we can write

$$\boldsymbol{K}^{*e}_{ij} = \sum_{g=1}^{c^e} \omega^e_g (\boldsymbol{B}^{*e^T}_i \boldsymbol{C}^e \boldsymbol{B}^{*e})_{\boldsymbol{Z}^e(g)}, \qquad i, j = 1, 2; \quad e = 1, 2 \dots M, \tag{111}$$

where $\boldsymbol{C}^e \in \mathbb{R}^{6\times 6}$ denotes the constitutive tangent matrix.

Remark 7.2. It is worth noting that this way of computing the coarse-scale internal force vector and stiffness matrices is formally identical to that employed in the evaluation of internal forces in a standard FE method with solid elements, the only difference being that, on the one hand, the strain–displacement matrices are no longer the gradient of the FE shape functions (but the inter-scale matrices given in Eq. (110)) and on the other hand, the weights are not the element Jacobians times the Gauss weights (but are determined by the ECM). This greatly facilitates the implementation of this type of coarse-scale element in a standard 3D FE code, and, furthermore, allows one to use existing 3D stress–strain constitutive laws. This latter aspect is specially advantageous when confronted with the analysis of composite beams, for one need not worry about introducing homogenization hypotheses in order to derive a "generalized" constitutive matrix (as done in standard composite beam theories, see for instance Ref. [37], pag. 166).

Remark 7.3. In using this hyperreduced-order approach, the Cauchy stresses are only calculated at the set $\boldsymbol{Z}^e$ of selected Gauss points ($\boldsymbol{S}^e_{\boldsymbol{Z}}$). For post-processing purposes, however, one can recover the stresses at all the Gauss points of the mesh ($\boldsymbol{S}^e$) by least-squares fitting (using the stress basis matrix $\boldsymbol{\Theta}^e$), i.e.:

$$\boldsymbol{S}^e = \boldsymbol{\Theta}^e (\boldsymbol{\Theta}^{e^T}_{\boldsymbol{Z}} \boldsymbol{\Theta}^e_{\boldsymbol{Z}})^{-1} \boldsymbol{\Theta}^{e^T}_{\boldsymbol{Z}} \boldsymbol{S}^e_{\boldsymbol{Z}}. \tag{112}$$

8. Consistency analysis

We begin the numerical assessment of the proposed HROM by examining its *consistency*,[8] i.e., its ability to reproduce, in the limit of no data compression, the same solutions used for training it.

8.1. Case with 6 training tests

To this end, we study two distinct prismatic structures, made up by repeating $M = 100$ times along the global x-axis the "slices" shown in Fig. 4 (rectangular and U-shaped cross-sections). The material in both cases is isotropic and behaves linearly, with Young's Modulus $E = 70000$ MPa, and Poisson's ratio $\nu = 0.3$. We carry out $\mathrm{d}_\mu = 6$ FE training tests, characterized by the following boundary conditions: no external forces, zero displacements on one of the end of the beam ($\bar{\boldsymbol{v}}_1 = \boldsymbol{0}$), while the other end[9] is subjected to rigid-body displacements of the form $\bar{\boldsymbol{v}}^j_N = \widehat{\boldsymbol{V}}_N \boldsymbol{\mu}^j$ ($j = 1, 2 \dots 6$), where $\boldsymbol{\mu}^j \in \mathbb{R}^6$ is given by $[\boldsymbol{\mu}^j]_i = 10^{-2}\delta_{ij}$, δ_{ij} being the Kronecker delta. Thus, in the first three tests ($j = 1, 2, 3$), the end cross-section undergoes translations of magnitude 10^{-2} m along the reference axes (we shall refer to these tests as axial, shear-y and shear-z tests); the remaining three tests ($j = 4, 5, 6$), on the other hand, correspond to rotations of the end cross-section, of magnitude 10^{-2} rad, around its centroid (we shall call these tests torsion, bending-y and bending-z tests). The deformed shapes (amplified so as to facilitate the visualization) of these 6 training tests are shown in Figs. 4c to 4.h.

8.1.1. Coarse-scale model

Since the problem is linear, and there is no truncation on the SVDs at subdomain level, these $\mathrm{d}_\mu = 6$ training tests give rise to $p^e = 6$ self-equilibrated and deformational modes for each subdomain Ω^e ($e = 1, 2 \dots M$). For illustration purposes, we show in Fig. 5 the deformed shapes corresponding to the 6 deformational modes[10] of

[8] Consistency here is to be understood in the terms established in Ref. [38], according to which "an approximation is said to be consistent if, when implemented without data compression, it introduces no additional error in the solution of the same problem for which data were acquired".

[9] We are tacitly here assuming that the nodes are consecutively numbered.

[10] Mode 1 is clearly the axial tension/compression mode; mode 2 displays the typical out-of-plane warping caused by torsion; modes 3 and 4 may be identified as pure bending modes, while modes 5 and 6 exhibit the characteristic cubic warping of shear deformation.

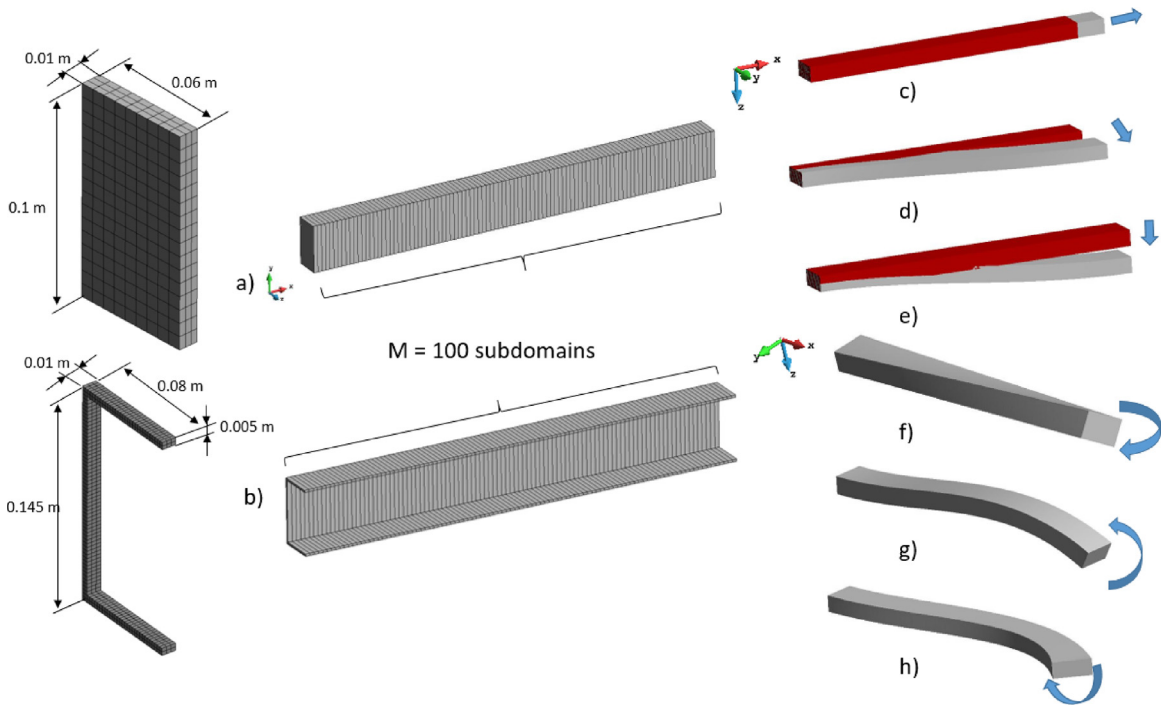

Fig. 4. Prismatic structures employed for assessing the consistency of the proposed multiscale HROM technique. (a) Rectangular cross-section subdomains discretized into 432 trilinear hexahedral elements. (b) U-shaped cross-section subdomains discretized into 708 trilinear hexahedral elements. (c) to (h) (Amplified) deformed shapes of the FE tests employed for training (prescribed displacements on both ends). (c) Axial test. (d) Shear-y test. (e) Shear-z test. (f) Torsion test. (g) Bending-y test. (h) Bending-z test.

the subdomain at the middle, $\Omega^{(50)}$, for the rectangular cross-section. In regards to the interface modes, the well-posedness considerations encapsulated in expression (60) dictate that the fictitious interfaces can only move as rigid bodies, with no fluctuations; therefore, each coarse-scale node has 6 DOFs (three translations and three infinitesimal rotations, as in a standard beam element formulation). Lastly, concerning the hyperreduction stage (reduction in the number of integration points, described in Section 7.5), the ECM chooses among the FE Gauss points of each subdomain a total of 21 integration points for each subdomain.[11] In summary, the coarse-scale representation of the prismatic beams depicted in Fig. 4 is formed by $M = 100$ (2-node) elements of equal length, featuring 6 DOFs per node and 21 integration points per element. Imposition of displacement boundary conditions in the coarse-scale model is trivial: $\boldsymbol{a}_1 = \boldsymbol{0} \in \mathbb{R}^6$, and $\boldsymbol{a}_N = \boldsymbol{\mu}^j \in \mathbb{R}^6$ $(j = 1, 2 \dots 6)$. Once the coarse-scale problem is solved for the global vector of DOFs $\boldsymbol{a}$, the associated rigid-body and deformational fine-scale displacements (denoted by $\hat{\boldsymbol{d}}^e$ and $\tilde{\boldsymbol{d}}^e$, respectively) are recovered by means of the coarse-to-fine operators defined in Eq. (79), namely $\tilde{\boldsymbol{d}}^e = \widetilde{\boldsymbol{U}}^e \boldsymbol{a}^e$ and $\hat{\boldsymbol{d}}^e = \widehat{\boldsymbol{U}}^e \boldsymbol{a}^e$ $(e = 1, 2 \dots M)$.

8.1.2. Deformational and rigid-body displacement errors

The relative L_2 error measures employed here for comparing HROM and FE solutions are given by

$$e^{def} = \sqrt{\frac{\sum_{e=1}^{M} (\tilde{\boldsymbol{d}}_{\boldsymbol{FE}}^e - \tilde{\boldsymbol{d}}^e)^T \boldsymbol{M}^e (\tilde{\boldsymbol{d}}_{\boldsymbol{FE}}^e - \tilde{\boldsymbol{d}}^e)}{\sum_{e=1}^{M} \tilde{\boldsymbol{d}}_{\boldsymbol{FE}}^{eT} \boldsymbol{M}^e \tilde{\boldsymbol{d}}_{\boldsymbol{FE}}^e}}, \tag{113}$$

[11] As noted by the second author in Ref. [27], in a linear elastic problem, the number of points required for exactly integrating the internal forces is equal to the number of independent entries of the reduced stiffness matrix (see Eq. (104)), which in this case, as the matrix is symmetric, is $(6 + 1)6/2 = 21$ points.

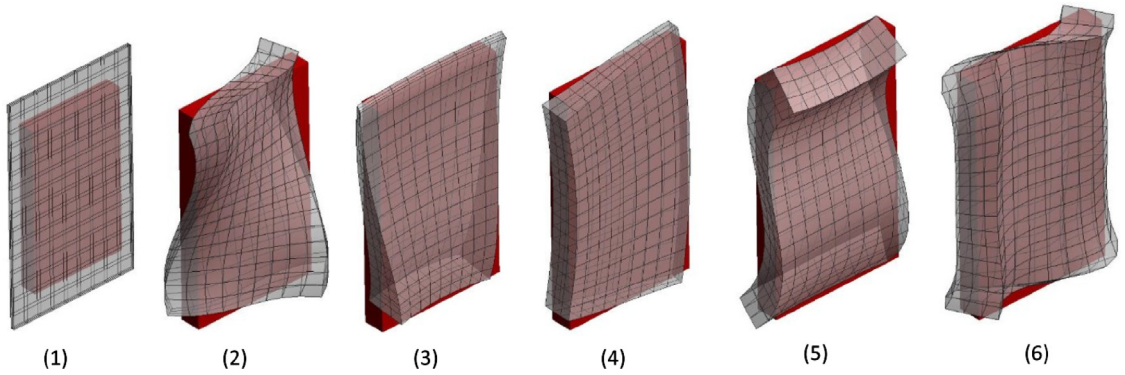

Fig. 5. Deformed shapes of the deformational modes corresponding to the subdomain Ω^{50} (located at the middle of the beam) for the case of rectangular-cross section.

Table 1
Rectangular cross-section beam. Deformational, rigid-body and total displacement errors defined in Eqs. (113), (114) and (115), respectively, for the 6 training tests with rigid-body displacements prescribed one end while the other end remains fixed.

	Axial	Shear-y	Shear-z	Torsion	Bending-y	Bending z
Deformational error (e^{def})	$2.96 \cdot 10^{-12}$	$1.43 \cdot 10^{-10}$	$1.30 \cdot 10^{-11}$	$1.71 \cdot 10^{-12}$	$4.46 \cdot 10^{-12}$	$5.53 \cdot 10^{-11}$
Rigid-body error (e^{rb})	$9.61 \cdot 10^{-5}$	$2.71 \cdot 10^{-4}$	$2.51 \cdot 10^{-4}$	$1.08 \cdot 10^{-3}$	$9.23 \cdot 10^{-4}$	$9.90 \cdot 10^{-4}$
Total error (e^{tot})	$9.61 \cdot 10^{-5}$	$2.71 \cdot 10^{-4}$	$2.51 \cdot 10^{-4}$	$1.08 \cdot 10^{-3}$	$9.23 \cdot 10^{-4}$	$9.90 \cdot 10^{-4}$

Table 2
U-shaped cross-section beam. Deformational, rigid-body and total displacement errors defined in Eqs. (113), (114) and (115), respectively, for the 6 training tests, for the 6 training tests with rigid-body displacements prescribed one end while the other end remains fixed.

	Axial	Shear-y	Shear-z	Torsion	Bending-y	Bending z
Deformational error (e^{def})	$2.33 \cdot 10^{-11}$	$2.38 \cdot 10^{-10}$	$6.87 \cdot 10^{-10}$	$2.56 \cdot 10^{-11}$	$1.28 \cdot 10^{-10}$	$4.58 \cdot 10^{-11}$
Rigid-body error (e^{rb})	$1.74 \cdot 10^{-2}$	$2.04 \cdot 10^{-2}$	$1.36 \cdot 10^{-3}$	0.34	$5.62 \cdot 10^{-3}$	$6.34 \cdot 10^{-2}$
Total error (e^{tot})	$1.74 \cdot 10^{-2}$	$2.04 \cdot 10^{-2}$	$1.36 \cdot 10^{-3}$	0.34	$5.62 \cdot 10^{-3}$	$6.34 \cdot 10^{-2}$

$$e^{rb} = \sqrt{\frac{\sum_{e=1}^{M} (\hat{\boldsymbol{d}}_{\boldsymbol{FE}}^{e} - \hat{\boldsymbol{d}}^{e})^{T} \boldsymbol{M}^{e} (\hat{\boldsymbol{d}}_{\boldsymbol{FE}}^{e} - \hat{\boldsymbol{d}}^{e})}{\sum_{e=1}^{M} \hat{\boldsymbol{d}}_{\boldsymbol{FE}}^{eT} \boldsymbol{M}^{e} \hat{\boldsymbol{d}}_{\boldsymbol{FE}}^{e}}}, \tag{114}$$

and

$$e^{tot} = \sqrt{\frac{\sum_{e=1}^{M} (\boldsymbol{d}_{\boldsymbol{FE}}^{e} - \boldsymbol{d}^{e})^{T} \boldsymbol{M}^{e} (\boldsymbol{d}_{\boldsymbol{FE}}^{e} - \boldsymbol{d}^{e})}{\sum_{e=1}^{M} \boldsymbol{d}_{\boldsymbol{FE}}^{eT} \boldsymbol{M}^{e} \boldsymbol{d}_{\boldsymbol{FE}}^{e}}}. \tag{115}$$

Here $\tilde{\boldsymbol{d}}_{\boldsymbol{FE}}^{e}$, $\hat{\boldsymbol{d}}_{\boldsymbol{FE}}^{e}$ and $\boldsymbol{d}_{\boldsymbol{FE}}^{e} = \tilde{\boldsymbol{d}}_{\boldsymbol{FE}}^{e} + \hat{\boldsymbol{d}}_{\boldsymbol{FE}}^{e}$ are the deformational, rigid-body and total FE nodal displacements of subdomain Ω^{e}. Thus, e^{def} in Eq. (113) conveys how accurate is the HROM in capturing the deformational part of the displacements of all the M domains (and therefore the stresses), whereas e^{rb} in Eq. (114) gives information on the quality of the approximation in terms of rigid-body displacements — which does not affect the stresses. The other error measure, e^{tot} includes both contributions.

In Tables 1 and 2 we display these error measures for the 6 training tests for the rectangular and U-shaped cross-section beams, respectively. A glance at the values of the total displacement error e^{tot} in both tables indicates that, in terms of fine-scale, nodal displacements, the *proposed multiscale HROM is not consistent with the FE model used for training it*. Indeed, even though we have not truncated either the SVDs for interaction forces nor the SVDs for stresses in the hyperreduction stage, the HROM fails to recover the same fine-scale, nodal displacements used for training it. In the case of the rectangular cross-section problem (Table 1), these errors are all below 0.1%, yet in the U-shaped profile case (Table 2) they attain values up to 34% (torsion test).

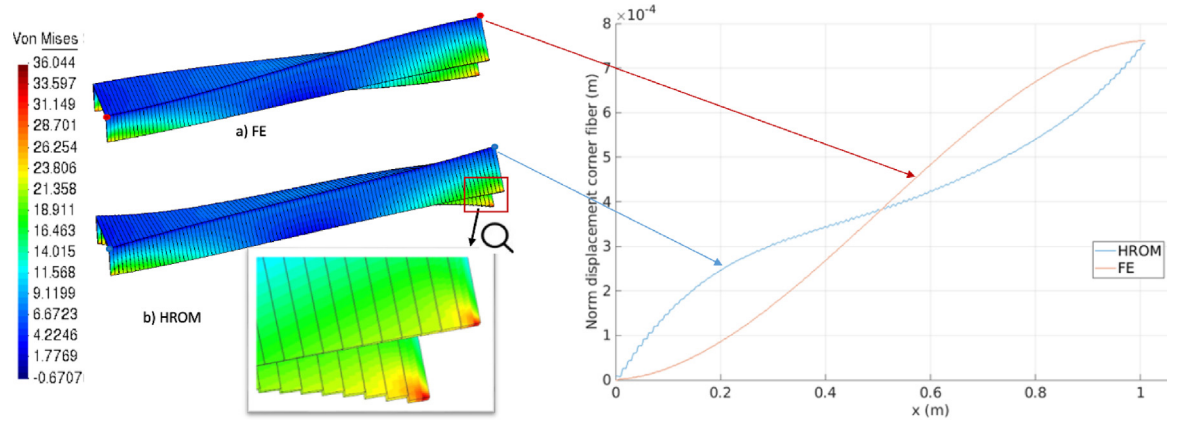

Fig. 6. (a) FE and (b)HROM deformed shapes (amplified by 100) corresponding to the torsion test, along with the corresponding Von Mises stress contour plot. Total number of DOFs and integration points in the FE model: $4.32 \cdot 10^5$ and $8 \cdot 101 \cdot 708 = 572064$. Total number of DOFs and integration points in the HROM: $6 \cdot 102 = 612$ and $21 \cdot 101 = 2121$. Rightmost graph: norm of the displacement of the longitudinal fiber located at the intersection between the flange and the web. Results computed with the FE model and the HROM.

On the other hand, inspection of the other error values e^{def} and e^{rb} reveals that this lack of consistency is to be exclusively attributed to *errors in capturing the rigid-body component*, for the deformational error e^{def} is negligible in all cases (it ranges between $1.5 \cdot 10^{-9}$ and $3 \cdot 10^{-12}$). In other words, we can assert that, at least for this particular training set, our *HROM is consistent in terms of deformational displacements, and therefore, in terms of stresses* — yet it errs in predicting rigid-body displacements. The situation is illustrated in Fig. 6, where we display the deformed shapes (amplified by a factor of 100) corresponding to the U-shaped cross-section torsion test for the FE model and the HROM, along with their corresponding Von Mises contour plots.[12] The deviations in terms of rigid body displacements can be appreciated in both the gaps between subdomains in the HROM plot (see enlarged view of the end with prescribed rotations), but most importantly, in the "inverted convexity" of the graph of the deflection of the longitudinal fiber located at the intersection between the flange and the web, displayed in the rightmost graph in Fig. 6. It should be emphasized that, despite these gross displacement errors, the Von Mises stress contour plots provided by the FE model and the HROM are identical.

8.1.3. Discussion

The fact that the proposed HROM multiscale scheme is not fully consistent with the full-order model used to train is to be attributed to the kinematical constraints dictated by the well-posedness considerations discussed in Section 6.3.1. Indeed, in the case at hand, these constraints translate in the fictitious interfaces only undergoing rigid-body displacements. This is in sharp contrast with what occurs with the interface boundaries of the subdomains, which do experience straining of one or other type, as evidenced by the warped and distorted shapes of the deformational modes depicted in Fig. 5. This inevitably introduces a gap between fictitious interfaces and subdomain boundaries, and as a consequence, the interface potential in the energy functional given in Eq. (12) cannot be driven to zero for all the subdomains — as it does occur in the FE model, where there is node-to-node compatibility and therefore the gap between subdomains is zero.

Less obvious is the reason why these unavoidable inter-domain gaps are due almost exclusively to errors in capturing the rigid-body component of the nodal displacements. A plausible rationale is that the strain potential Π^e_{int} in Eq. (12) depends only on the deformational component, while the interface potential π^e depends on both deformational and rigid-body components. Thus, an inaccurate description of the deformational part would be taxing in both terms, whereas inaccuracies in the rigid-body part only affects the interface potential. This might explain why the method tends to furnish accurate prediction in terms of deformational displacements (and thus stresses), but not rigid-body displacements.

[12] The Cauchy stresses at the Gauss points are recovered from the stresses at the selected 21 integration points by least-squares fitting (see Eq. (112)).

Table 3
Rectangular cross-section beam. Deformational, rigid-body and total displacement errors defined in Eqs. (113), (114) and (115), respectively, for the case with 7 training tests.

	Axial	Shear-y	Shear-z	Torsion	Bending-y	Bending z	Torque
Def. error (e^{def})	$1.39 \cdot 10^{-7}$	$2.93 \cdot 10^{-12}$	$1.43 \cdot 10^{-10}$	$1.64 \cdot 10^{-11}$	$5.53 \cdot 10^{-12}$	$5.52 \cdot 10^{-11}$	$1.00 \cdot 10^{-7}$
RB error (e^{rb})	$1.89 \cdot 10^{-3}$	$9.61 \cdot 10^{-5}$	$2.71 \cdot 10^{-4}$	$2.51 \cdot 10^{-4}$	$9.23 \cdot 10^{-4}$	$9.90 \cdot 10^{-4}$	$1.91 \cdot 10^{-3}$
Total (e^{tot})	$1.89 \cdot 10^{-3}$	$9.61 \cdot 10^{-5}$	$2.71 \cdot 10^{-4}$	$2.51 \cdot 10^{-4}$	$9.23 \cdot 10^{-4}$	$9.90 \cdot 10^{-4}$	$1.91 \cdot 10^{-3}$

Table 4
U-shaped cross-section beam. Deformational, rigid-body and total displacement errors defined in Eqs. (113), (114) and (115), respectively, for the case with 7 training tests.

	Axial	Shear-y	Shear-z	Torsion	Bending-y	Bending z	Torque
Def. error (e^{def})	$3.45 \cdot 10^{-11}$	$7.30 \cdot 10^{-11}$	$5.42 \cdot 10^{-10}$	$1.87 \cdot 10^{-9}$	$3.57 \cdot 10^{-10}$	$8.98 \cdot 10^{-11}$	$8.92 \cdot 10^{-11}$
RB error (e^{rb})	$2.22 \cdot 10^{-3}$	$1.74 \cdot 10^{-2}$	$1.39 \cdot 10^{-3}$	$1.36 \cdot 10^{-3}$	$5.62 \cdot 10^{-3}$	$5.36 \cdot 10^{-3}$	$2.95 \cdot 10^{-3}$
Total (e^{tot})	$2.22 \cdot 10^{-3}$	$1.74 \cdot 10^{-2}$	$1.39 \cdot 10^{-3}$	$1.36 \cdot 10^{-3}$	$5.62 \cdot 10^{-3}$	$5.36 \cdot 10^{-3}$	$2.95 \cdot 10^{-3}$

8.2. Case with 7 training tests

Let us examine now what occurs in terms of consistency when the number of deformational modes per subdomain is greater than 6. To this end, we incorporate in the training set used in the preceding consistency analysis an additional test in which one of the ends is fixed ($\bar{\boldsymbol{v}}_1 = \boldsymbol{0}$) while the other end is subjected to a torque applied at the centroid of the cross section, of magnitude $T_{end} = 100$ Nm. In the FE model, this torque is represented by the vector of nodal forces $\bar{\boldsymbol{F}}_N = \bar{\boldsymbol{M}}_N \widehat{\boldsymbol{V}}_N (\widehat{\boldsymbol{V}}_N^T \bar{\boldsymbol{M}}_N \widehat{\boldsymbol{V}}_N)^{-1} \boldsymbol{\gamma}$, where

$$\boldsymbol{\gamma} = [0\ 0\ 0\ T_{end}\ 0\ 0]^T. \tag{116}$$

Note that, in imposing this system of nodal forces in the FE model, the vector of resultant forces and resultant moments becomes $\widehat{\boldsymbol{V}}_N^T \bar{\boldsymbol{F}}_N = \boldsymbol{\gamma}$, as required. Likewise, for the coarse-scale model, the first 6 entries of nodal force to be imposed on the free end ($\bar{\boldsymbol{F}}_N^*$) is, according to Eq. (96)b, equal to $\boldsymbol{\gamma}$. The remaining entries, if any, are to be set to zero, by virtue of the orthogonality between rigid-body and fluctuation modes (see Eq. (29)).

In the case of the rectangular cross-section beam, the incorporation of this training test results in a variable number of deformational modes along the beam. From subdomain Ω^1 (which is the one on the fixed end) to subdomain Ω^{68}, the number of deformational modes remains equal to 6, while for the remaining subdomains, it increases up to 7 modes. This variability is reflected also in the number of coarse-scale DOFs per node. Indeed, coarse-scale elements from $e = 1$ to $e = 68$ has 6 DOFs per node, and from $e = 70$ to $e = 100$ 7 DOFs per node; element $e = 69$, on the other hand, is a "transition" element, with 6 DOFs in one node, and 7 DOFs in the other. This seventh DOF is the amplitude of the fluctuation mode automatically selected by Algorithm 3 from within the space spanned by what we have called the displacement fluctuation candidates.

In the case of the U-shaped cross-section beam, on the other hand, the number of deformational modes turns out to be equal to $p^e = 7$ for all domains ($e = 1, 2 \ldots 100$). The number of DOFs per coarse-scale node is also equal to 7 for all nodes except for the one on the fixed end, which is equal to 6.

The L_2 error measures Eqs. (113) to (115) for these 7 tests, using the new kinematics are displayed in Tables 3 and 4, for the rectangular and U-shaped cross-section beams, respectively. Two things deserve notice in these Tables. Firstly, the accuracy in terms of deformational displacements is significantly higher (between 4 and 8 order of magnitudes more accurate) than the accuracy in capturing rigid-body counterpart. Note that this is the same trend observed in the 6-tests problem, and thus provides confirmation to the conjecture made in the discussion of Section 8.1.3. Secondly, in the case of the U-shaped cross-section beam, comparison of the rigid-body errors for the 6 tests with prescribed displacements in Tables 2 and 4 reveals that the enrichment of the coarse-scale kinematics with an additional DOF has notably increased the quality of the coarse-scale approximations in terms of rigid-body displacements. For instance, in the test with prescribed rotation around the axis of the beam (test labeled "torsion"), e^{rb} has dropped from 34% to 0.136%. This increase of accuracy can be further appreciated in Fig. 7, where we show the same plots displayed previously in Fig. 6, but now with the new kinematics — indeed, the gaps between

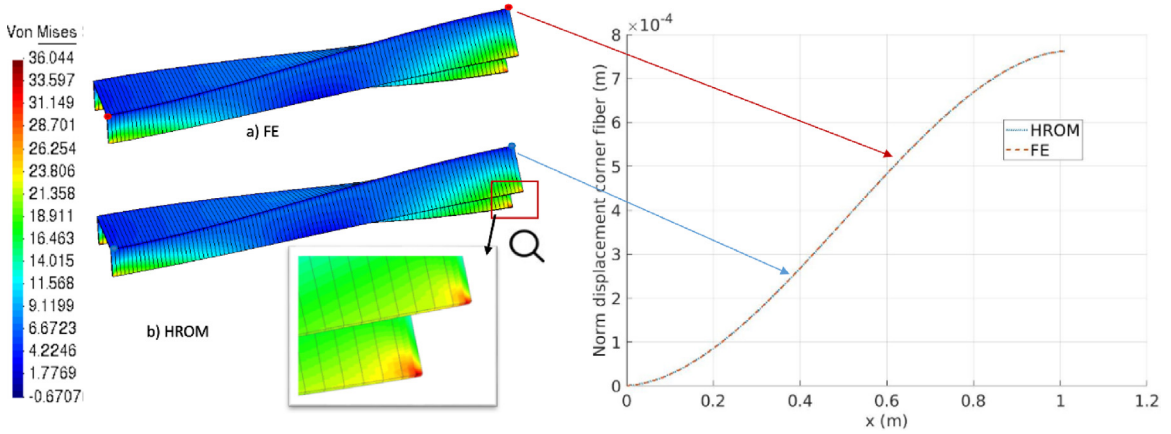

Fig. 7. (a) FE and (b)HROM deformed shapes (amplified by 100) corresponding to the torsion test, along with the corresponding Von Mises stress contour plot. Total number of DOFs and integration points in the HROM: $6 + 7 \cdot 102 = 720$ and $28 \cdot 101 = 2828$. Rightmost graph: norm of the displacement of the longitudinal fiber located at the intersection between the flange and the web. Results computed with the FE model and the HROM.

subdomains are now imperceptible, and besides, the convexity of the graph of the displacement of the corner fiber does coincide with that predicted by the FE model.

9. "Characteristic" coarse-scale elements

9.1. Definition

The deformational and interaction force modes computed from the training tests discussed in the foregoing encode information regarding, not only how loads applied on one end are transmitted through the prism to the other end, but also the local effects caused by the particular way these loads are applied (in the case at hand, as prescribed translations and rotations of the end cross-sections). Now we are interested in extracting the modal information that solely concerns the transmission of loads, thus ignoring local effects. The coarse-scale element resulting from these modes will be referred to as the "characteristic or representative" element, and will be akin to the 1D finite elements derived from classical beam theories — in the sense that it will depend only on the geometry and material composition of the subdomain it intends to represent. Later on, in Section 9.3.4, we shall see how to enrich the kinematics of this coarse-scale element to account also for local effects.

To quantify how accurate is a given coarse-scale element in transmitting loads, we shall examine the error incurred by the coarse-scale model in predicting the resultants and moment resultants at each interface; to this end, we define the global error measure:

$$\epsilon^f = \sqrt{\frac{\sum_{I=1}^{N} \| \widehat{\boldsymbol{V}}_I^T \boldsymbol{\lambda}_{\mathbf{f}_i}^{FE,e} - \boldsymbol{F}_{int\,i}^{*e}(1:6) \|^2}{\sum_{I=1}^{N} \| \widehat{\boldsymbol{V}}_I^T \boldsymbol{\lambda}_{\mathbf{f}_i}^{FE,e} \|^2}}, \qquad (I = \boldsymbol{\mathcal{T}}(e,i)). \tag{117}$$

Here $\boldsymbol{F}_{int\,i}^{*e}(1:6)$ denotes the first 6 entries of the coarse-scale internal forces at the ith node ($i = 1, 2$) of element e, defined in Eq. (91) (these entries are the resultants and moment resultants computed by the coarse-scale model). Likewise, $\widehat{\boldsymbol{V}}_I^T \boldsymbol{\lambda}_{\mathbf{f}_i}^{FE,e}$ stands for the resultants and moment resultants computed from the FE interaction force vector $\boldsymbol{\lambda}_{\mathbf{f}_i}^{FE,e}$. For completeness, we define a similar measure in terms of displacements:

$$\epsilon^a = \sqrt{\frac{\sum_{I=1}^{N} \| \widehat{\boldsymbol{\mathcal{P}}}_I \boldsymbol{d}_{\mathbf{f}_i}^{FE,e} - \widehat{\boldsymbol{a}}_I \|^2}{\sum_{I=1}^{N} \| \widehat{\boldsymbol{\mathcal{P}}}_I \boldsymbol{d}_{\mathbf{f}_i}^{FE,e} \|^2}}, \qquad (I = \boldsymbol{\mathcal{T}}(e,i)), \tag{118}$$

where $\widehat{\boldsymbol{\mathcal{P}}}_I \boldsymbol{d}_{\mathbf{f}_i}^{FE,e}$ denotes the translations and rotations of the Ith interface computed from the vector of FE displacements $\boldsymbol{d}^{FE,e}$ (the operator $\widehat{\boldsymbol{\mathcal{P}}}_I$ was defined in Eq. (53)), while $\widehat{\boldsymbol{a}}_I$ are its counterpart in the coarse-scale

Table 5
Rectangular cross-section beam. Error measures defined in Eqs. (117) (ϵ^f, for the resultants and moment resultants) and (118) (ϵ^a, for the cross-section translations and rotations), for the 6 training tests described in Section 8.1 (see Fig. 4). The coarse-scale model is constructed using the same basis matrices for all slices — more specifically, the modes of subdomain Ω^{50} determined in the consistency analysis of Section 8.1.

	Axial	Shear-y	Shear-z	Torsion	Bending-y	Bending z
Resultants (ϵ^f)	$0.49 \cdot 10^{-2}$	$1.04 \cdot 10^{-2}$	$1.38 \cdot 10^{-2}$	$1.47 \cdot 10^{-2}$	$1.37 \cdot 10^{-2}$	$1.03 \cdot 10^{-2}$
RB disp. (ϵ^a)	$0.24 \cdot 10^{-2}$	$0.36 \cdot 10^{-2}$	$0.44 \cdot 10^{-2}$	$0.65 \cdot 10^{-2}$	$0.79 \cdot 10^{-2}$	$0.63 \cdot 10^{-2}$

model. Another prerequisite for a coarse-scale element to be regarded as "representative" is its ability to capture the stress distribution sufficiently away from the regions where loads are applied. To examine this aspect of the model, we introduce the following stress error estimation:

$$E^e_{vm} = \sqrt{\frac{\int_{\Omega^e} \Delta\tau^2 \, d\Omega}{\int_{\Omega^e} \tau^{FE^2} \, d\Omega}}, \qquad e = 1, 2 \dots M. \tag{119}$$

Here $\tau^{FE} : \Omega^e \to \mathbb{R}$ stands for the Von Mises stress computed by the FE model, while $\Delta\tau$ is the Von Mises stress that results from the difference between the stresses computed by the FE model and the coarse-scale HROM.

9.2. Rectangular cross-section

We begin our study with the rectangular cross-section beam. The slices which are less tainted with local effects are that located further from the ends, in this case Ω^{50} and Ω^{51}. Accordingly, we tentatively take the deformational and interface force modes determined for subdomain Ω^{50} in the 6 training tests described in Section 8.1 — the deformed shapes of such deformational modes were displayed in Fig. 5 — as the characteristic modes of the subdomain. Then we construct a coarse-scale model of the prism using these modes for all the $M = 100$ subdomains, and evaluate the error indicators presented in Eqs. (117) and (118). The results are presented in Table 5. Observe that all values are below 1.5%, a figure that may be deemed low for engineering standards. Thus, we may claim that the employed deformational and interaction force modes are indeed "characteristic" of the subdomain,[13] in the sense defined above.

To further corroborate this claim, we examine the extent to which our coarse-scale element is able to predict the distribution of stresses sufficiently away from the ends of the prism — in this case, "sufficiently away" means approximately at a distance equal to the height of the cross-section, $l = 0.1$ m, in accordance to the Principle of Saint Venant [39]. To this end, in Fig. 8, we plot the Von Mises stress error E^e_{vm} ($e = 1, 2 \dots M$), defined in Eq. (119), for the 6 training tests. It can be seen that the error is maximum at the ends of the prism (around 50%), and decays gradually as we move from the ends. From slices 10 to 90 the stress error for all the 6 tests is indeed relatively low — between 0.5%, in the axial test, and 5 %, in the y-bending test —, a fact that confirms the representative nature of the employed coarse-scale element.

Further insight into the quality of the stress approximations can be gained by inspecting in Fig. 9 the contour plots of Von Mises stress computed by the full-order FE model and the HROM at domain Ω^{33}, in the y-bending test — according to Fig. 8, this is where the maximum stress error of all tests and subdomains takes place. It can be appreciated that the stress patterns are qualitatively identical, the only difference being the maximum values attained in each case — the HROM underpredicts the maximum Von Mises by 1.5%, which is again a relatively low error for engineering practice.

[13] We explore the performance of the modes obtained from neighboring slices, as well as mixing the information of various slices, and the result was essentially the same in all cases.

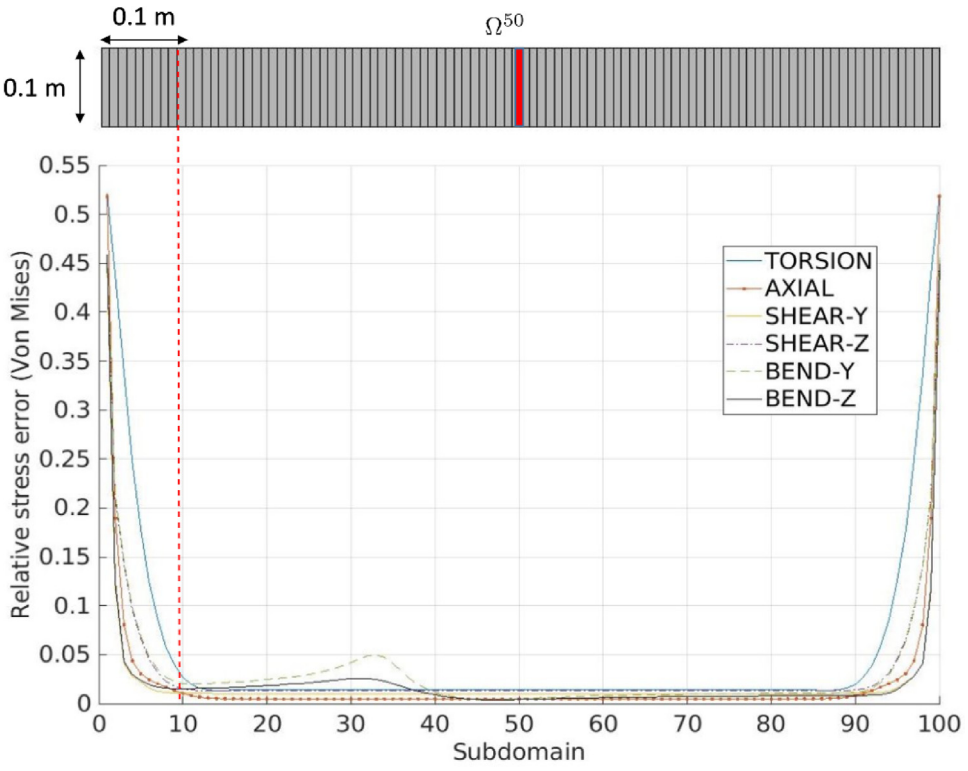

Fig. 8. Rectangular cross-section beam. Von Mises error measure (defined in (119)), for the 6 training tests depicted in Fig. 4. The basis matrices of all subdomains are equal to the basis matrices obtained for the subdomain at the middle (subdomain Ω^{50}, highlighted in red in the top of the figure). (For interpretation of the references to color in this figure legend, the reader is referred to the web version of this article.)

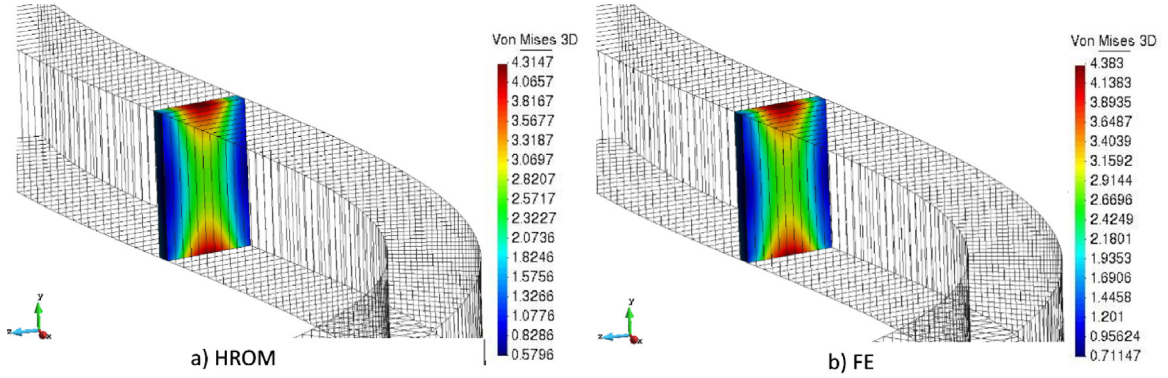

Fig. 9. Y-bending test. Deformed shape (x 100) and contour plot of Von Mises stress for subdomain Ω^{33}, in MPa. (a) Coarse-scale HROM results, using the same "characteristic" modes for all the subdomains. (b) Results computed with the full-order FE method.

9.2.1. Comparison with Timoshenko's "exact" theory

The stresses at the subdomain studied in the foregoing are caused mainly by shear forces[14] (in this case in the z-direction). An immediate implication of this observation is that our beam element is apparently not afflicted by

[14] From beam theory considerations, we know that bending moments are zero at a distance from the fixed end equal to 1/3 of the length of the beam subjected to a prescribed rotation on one end.

any of the shortcomings that typically beset other classical 1D FE beam formulations with the same kinematics (6 DOFs per node), such as shear locking in standard Timoshenko-based beam elements [37]. This desirable feature may be attributed to the fact that, in contrast to this classical formulation, in our coarse-scale model the interface boundaries are not forced to remain planes — recall that it is the fictitious interfaces which remain unstrained. Thus, our formulation is more in line with the sometimes called "exact" Timoshenko's beam theory [40] for rectangular cross-sectional beams, which allows the cross-sections to freely warp when sheared. The resemblance becomes apparent when comparing the stiffness matrices arising from this Timoshenko's formulation, and the one provided by our coarse-scale model. For the sake of brevity, we compare in what follows only the first block matrix of the diagonal of the element stiffness matrix; for the exact Timoshenko's beam theory, the expression for this (symmetric) matrix reads (see Chapter 5 of Ref. [41]):

$$\boldsymbol{K}_{\mathbf{11}}^{e,timosh} = E \begin{bmatrix} \frac{A}{L} & 0 & 0 & 0 & 0 & 0 \\ & \frac{12I_z}{(1+\Phi_z)L^3} & 0 & 0 & 0 & \frac{6I_z}{(1+\Phi_z)L^2} \\ & & \frac{12I_y}{(1+\Phi_y)L^3} & 0 & \frac{6I_y}{(1+\Phi_y)L^2} & 0 \\ & & & \frac{GJ}{L} & 0 & 0 \\ & & & & \frac{(4+\Phi_y)I_y}{(1+\Phi_y)L} & 0 \\ & \text{(sym.)} & & & & \frac{(4+\Phi_z)I_z}{(1+\Phi_z)L} \end{bmatrix}$$

$$= 10^2 \begin{bmatrix} 420 & 0 & 0 & 0 & 0 & 0 \\ & 134.2 & 0 & 0 & 0 & 0.6709 \\ & & 133.4 & 0 & 0.6671 & 0 \\ & & & 0.1214 & 0 & 0 \\ & & & & 0.1293 & 0 \\ & \text{(sym.)} & & & & 0.3534 \end{bmatrix}. \tag{120}$$

Here, $A = 6 \cdot 10^{-3}$ m^2 is the area of the cross-section; $L = 0.01$ is the width of the slice; $I_y = 1.8 \cdot 10^{-6}$ m^4 and $I_z = 5 \cdot 10^{-6}$ m^3 are the moments of inertia of the cross section; $G = E/(2(1+\nu)) = 2.69 \cdot 10^5$ MPa is the shear modulus; $J = 4.51 \cdot 10^{-6}$ m^4 is the torsion constant[15]; and $\Phi_y = 12EI_y/(GA_sL^2) = 312.0$ and $\Phi_z = 12EI_z/(GA_sL^2) = 112.3$ are dimensionless parameters depending on the cross-sectional area in shear, which here is set, as customary in rectangular cross-sections [43], to $A_s = \frac{5}{6}A$. On the other hand, the stiffness matrix computed by our coarse-scale model is given by (see Eq. (103)):

$$\boldsymbol{K}_{\mathbf{11}}^{*e} = \widetilde{\boldsymbol{P}}_1^{e^T} \boldsymbol{\mathcal{K}}^e \widetilde{\boldsymbol{P}}_1^e = 10^2 \begin{bmatrix} 420 & 0 & 0 & 0 & 0 & 0 \\ & 134.6 & 0 & 0 & 0 & 0.6728 \\ & & 130.3 & 0 & 0.6516 & 0 \\ & & & 0.1220 & 0 & 0 \\ & & & & 0.1293 & 0 \\ & \text{(sym.)} & & & & 0.3537 \end{bmatrix}. \tag{121}$$

The difference between these two matrices is equal to (in %)

$$\begin{bmatrix} 0.0\% & & & & & \\ & 0.28\% & & & & 0.28\% \\ & & 2.38\% & & 2.38\% & \\ & & & 0.52\% & & \\ & \text{(sym.)} & & & 0.24\% & \\ & & & & & 0.11\% \end{bmatrix} \tag{122}$$

which proves the point made above (all values are below 2.5%).

Given the similarity between the stiffness matrix based on Timoshenko's theory and the one based on the proposed multiscale scheme, it is natural to wonder which is more accurate — in comparison with the FE solution, which is taken as the "exact" solution.[16] To resolve this question, we have computed the counterpart of Table 5 when using the Timoshenko's stiffness matrix; the results are displayed in Table 6. Comparison of both tables indicate that, while in displacements they furnish the same level of accuracy, in terms of resultants and moments resultants, the proposed approach is slightly more accurate; for instance, in the torsion test, our model gives an error of 1.47%, while the analytical one furnishes 1.96%.

[15] We have used the formula $J = \beta ab^3$, where $\beta = (1/3 - 0.21b/a(1 - b^4/(12a^4)))$, $a = 0.1$ m and $b = 0.06$ m, see Ref. [42], Table 3.1.

[16] We performed mesh refinement analyses to assure that this FE solution is "sufficiently exact".

Table 6
Rectangular cross-section beam. Error measures defined in Eqs. (117) (ϵ^f, for the resultants and moment resultants) and (118) (ϵ^a, for the cross-section translations and rotations), for the 6 training tests described in Section 8.1. The coarse-scale model is constructed using the element stiffness matrix derived from the "exact" Timoshenko's theory, displayed in Eq. (120).

	Axial	Shear-y	Shear-z	Torsion	Bending-y	Bending z
Resultants (ϵ^f)	$0.49 \cdot 10^{-2}$	$1.15 \cdot 10^{-2}$	$1.66 \cdot 10^{-2}$	$1.96 \cdot 10^{-2}$	$1.64 \cdot 10^{-2}$	$1.14 \cdot 10^{-2}$
RB disp. (ϵ^a)	$0.24 \cdot 10^{-2}$	$0.36 \cdot 10^{-2}$	$0.43 \cdot 10^{-2}$	$0.65 \cdot 10^{-2}$	$0.77 \cdot 10^{-2}$	$0.63 \cdot 10^{-2}$

Table 7
U-shaped cross-section beam. Error measures defined in Eqs. (117) (ϵ^f, for the resultants and moment resultants) and (118) (ϵ^a, for the cross-section translations and rotations), for the 6 training tests described in Section 8.1. The coarse-scale model is constructed using the same basis matrices for all slices — more specifically, the 6 modes of subdomain Ω^{50} determined in the consistency analysis of Section 8.1. Thus, the resulting coarse-scale element has 6 DOFs per node.

	Axial	Shear-y	Shear-z	Torsion	Bending-y	Bending z
Resultants (ϵ^f)	$0.34 \cdot 10^{-2}$	$0.58 \cdot 10^{-2}$	$1.05 \cdot 10^{-2}$	$7.33 \cdot 10^{-2}$	$1.17 \cdot 10^{-2}$	$0.57 \cdot 10^{-2}$
RB disp. (ϵ^a)	$1.67 \cdot 10^{-2}$	$5.54 \cdot 10^{-2}$	$0.36 \cdot 10^{-2}$	$10.20 \cdot 10^{-2}$	$0.6 \cdot 10^{-2}$	$7.83 \cdot 10^{-2}$

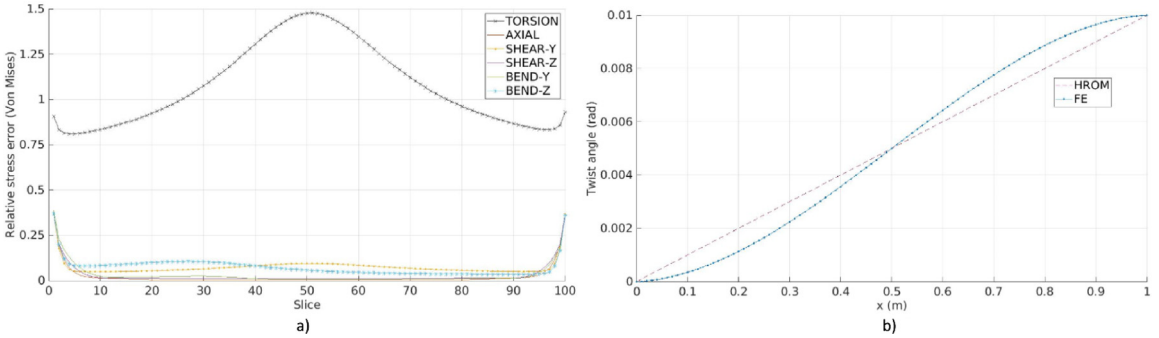

Fig. 10. U-shaped cross-section. Von Mises error measure (defined in Eq. (119)), for the 6 training tests described in Section 8.1. The basis matrices of all subdomains are equal to the basis matrices obtained for the subdomain at the middle (subdomain Ω^{50}).

9.3. U-shaped cross-section

9.3.1. Training with 6 tests and one sampled subdomain

To determine the characteristic coarse-scale element associated to the U-shaped cross-section slice, we follow the same steps described in the foregoing for the rectangular cross-section slice. Firstly, we tentatively select the 6 deformational and interaction force modes obtained for subdomain Ω^{50} in the 6 training tests described in Section 8.1, construct the coarse-scale model of the prism using these modes (resulting in a 2-nodes element with 6 DOFs per node, as in the case of the rectangular cross-section), and then evaluate the error indicators presented in Eqs. (117) and (118), as well as the Von Mises stress error defined in Eq. (119), for the 6 training tests. Results are shown in Table 7 and Fig. 10a, respectively.

Inspection of these results immediately reveals that, as opposed to the case of the rectangular cross-section case, the coarse-scale model constructed using the 6 deformational and force modes of the central subdomain Ω^{50} is not able to accurately transmit loads from one end of the beam to the other in all the 6 training tests. Errors are more pronounced in the case of the torsion test, specially in terms of Von Mises stresses, where deviations with respect to the FE results reach values up to 150%, see Fig. 10a. To shed light on the cause of the misperformance, we display in Fig. 10b the evolution along the beam of the twist angle computed from the FE results and from the HROM.

Observe that the 6-DOFs coarse-scale model predicts a linear evolution along the beam (i.e., constant twist angle), whereas the "correct" result (based on FE calculations) is that the curve should exhibit a cubic profile.[17]

9.3.2. Augmenting the training set (or the analyzed subdomains)

It becomes apparent from the above results that the modal information of the central subdomain Ω^{50} retrieved from the 6 training tests with prescribed displacements on both ends, described in Section 8.1, is not sufficient to capture the torsional behavior of the beam. It is necessary, thus, to enrich the basis matrices with additional information on how the beam behaves in torsion. The simplest route from the implementational point to view is to carry out additional (judiciously chosen) training tests, and progressively enrich the modal bases with the snapshots coming from these tests until meeting the error criteria defined in Section 9.1. For instance, in this case, we have found that augmenting the training set with two FE tests in which a torque is applied on each of the ends (while the other end is fixed, as done in the consistency analysis discussed in Section 8.2, see Eq. (116)) leads to a coarse-scale element that is representative in the sense defined previously. The 8 self-equilibrated and deformational modes obtained from the corresponding snapshots of slice Ω^{50}, for the 8 training tests (the 6 tests with prescribed displacements, plus these two tests with prescribed forces), are displayed in Figs. 11a and 11b, respectively.

Nevertheless, it should be pointed out that it is possible to arrive at the same set of modes solely from the information contained in the 6 training tests with prescribed displacements. This strategy capitalizes on the fact that the structure we are analyzing is made by tiling copies of the same subdomain along the x-axis, and therefore, the missing information can be obtained from the snapshots of a group of contiguous subdomains, located in the central portion of the beam — rather than focusing on just one slice, as done in the approach described above. The strategy goes as follows. We begin by selecting a set of subdomains pertaining to the central region of the beam. Here we have taken 11 subdomains, from Ω^{45} to Ω^{55}, but we have empirically found that sets with either less (up to 4) or more subdomains (provided they are sufficiently far from the ends) furnishes essentially the same coarse-scale model. The interface forces and displacement snapshots of these 11 slices for the 6 training tests are stored in the snapshot matrices $\boldsymbol{A}_{\boldsymbol{\lambda}}$ and $\boldsymbol{A}_{\boldsymbol{d}}$, respectively. The next step is the determination of the self-equilibrated modes $\widetilde{\boldsymbol{\Psi}}_{\mathbf{f}}$, by first computing the self-equilibrated component of[18] $\boldsymbol{A}_{\boldsymbol{\lambda}}$ ($\tilde{\boldsymbol{A}}_{\boldsymbol{\lambda}} = \widetilde{\boldsymbol{\mathcal{H}}}\boldsymbol{A}_{\boldsymbol{\lambda}}$, see Eq. (37)). As explained in Section 5.3, the desired modes $\widetilde{\boldsymbol{\Psi}}_{\mathbf{f}}$ are an (approximated) basis for the column space of $\tilde{\boldsymbol{A}}_{\boldsymbol{\lambda}}$. The level of approximation is determined by a truncation tolerance ϵ_λ, which we set here to $\epsilon_\lambda = 10^{-3}$ (introducing this truncation is of crucial importance, because otherwise the resulting basis may contain inessential modes representing negligible local effects, or the effect of round-off errors). To ensure this level of approximation for all the 6 tests, we separately apply the weighted SVD (see Eq. (40)) to the block matrices of $\tilde{\boldsymbol{A}}_{\boldsymbol{\lambda}}$ associated to each of the 6 tests. This produces 3 modes for the torsion test, 1 mode for the axial test, and 2 modes for each of the remaining tests. The deformed shapes of the deformational modes which are work conjugate to these set of self-equilibrated modes (obtained through the procedure outlined in Box 5.1) are displayed in Fig. 12. The set of resulting self-equilibrated modes (in this case a total number of 12), is then subjected to an additional SVD in order to eliminate redundancies. This finally furnishes 8 dominant self-equilibrated modes,[19] which turn out to span the same subspace as the one engendered by the modes shown in Fig. 11a — hence the equivalence.

Remark 9.1. Although admittedly more elaborate than the one involving one single subdomain, the above explained methodology allows the systematization of the determination of the representative modes of each type of subdomain, for it does not require to find which are the "correct" boundary conditions for the additional tests.

Remark 9.2. To alleviate the computational burden associated to the (offline) FE training analyses, subdomains of different geometry can be processed at the same time in the same prismatic structure. Likewise, manifold interpolation techniques can be exploited to derive the basis matrices of a given subdomain from the basis matrices of

[17] Least-squares fitting gives the cubic equation (with practically zero error): $\widehat{\boldsymbol{a}}_4(x) = -0.018x^3 + 0.02699x^2 + 0.001011x$..

[18] It should be noted that in this case this step may be skipped, since there are no external forces applied on the selected subdomains, and therefore, the nodal interaction forces of each subdomain forms already a system of self-equilibrated forces.

[19] A more detailed analysis reveals that the cause of the existence of 4 redundant modes is that the modes of the shear-y and bending-z, on the one hand, and the shear-z and bending-y tests, span practically the same subspace. In turn, this suggest that, as a rule, it suffices to perform 4 training tests for determining the characteristic modes of straight beams: 1 for the axial mode(s), 1 for the torsion mode(s), and 2 either shear or bending tests in both transversal directions.

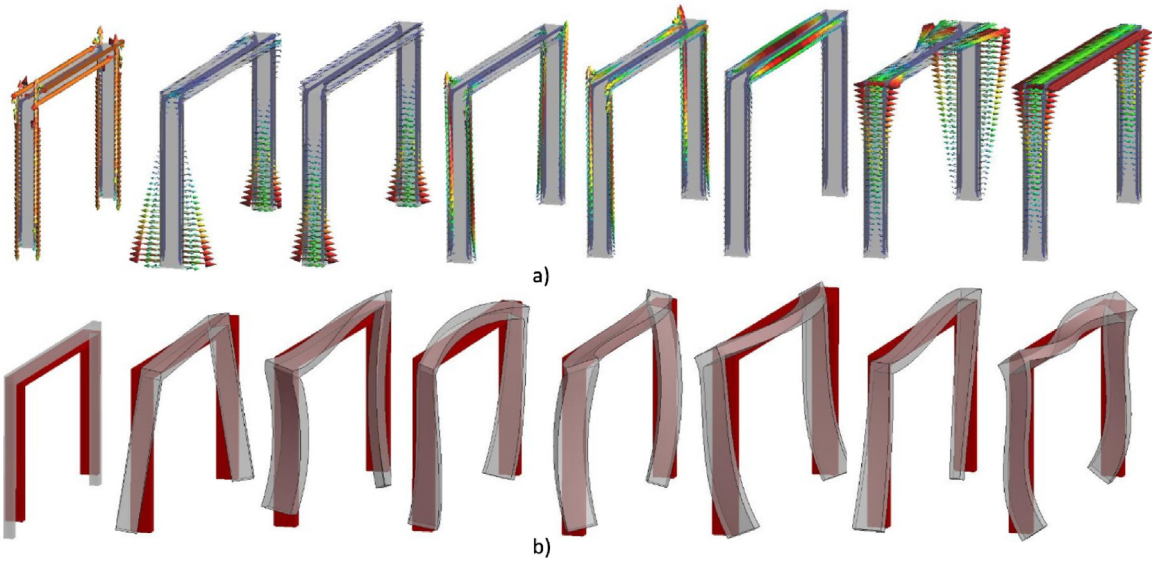

Fig. 11. (a) Self-equilibrated modes ($\widetilde{\boldsymbol{\Psi}}_{\mathbf{f}}$) obtained from orthogonalization of the FE interaction nodal forces of subdomain Ω^{50} in 8 different training tests, namely the 6 training tests with prescribed displacements described in Section 8.1, plus two tests with prescribed torque in each of the ends of the prism. (b) Deformed shapes of the associated deformational modes ($\widetilde{\boldsymbol{\Phi}}$).

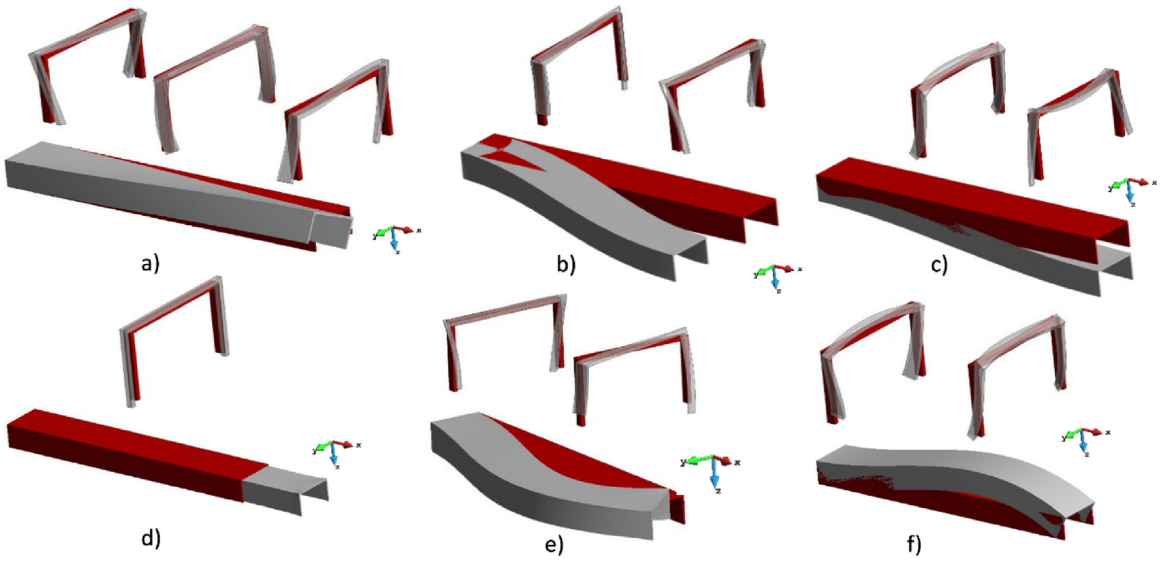

Fig. 12. Deformed shapes of the 6 training tests, along with the deformed shapes of the deformational modes obtained from the snapshots of subdomains from Ω^{45} to Ω^{55}. Truncation tolerance $\epsilon_\lambda = 10^{-3}$. (a) Torsion test (3 modes). (b) Shear-y test (2 modes). (c) Shear-z test (2 modes). (d) Axial test (1 mode). (e) Bending-z test (2 modes). (f) Bending-y test (2 modes).

subdomains with similar geometries (without the need of additional FE analyses). These two strategies are discussed more in detail in Appendix B.

Once we have at our disposal the self-equilibrated ($\widetilde{\boldsymbol{\Psi}}_{\mathbf{f}}$) and deformational modes ($\widetilde{\boldsymbol{\Phi}}$), either calculated from one single subdomain and 8 tests, or several subdomains and only 6 tests, we can proceed with the determination of the fluctuation modes of the fictious interface, by following the steps outlined in Algorithm 3. The deformed shapes of the candidate fluctuation modes $\widetilde{\boldsymbol{W}}$, computed in step 3, are displayed in Fig. 13b. On the other hand, the intersection of the column space of the interaction forces of the two interface boundaries (step 4 in Algorithm

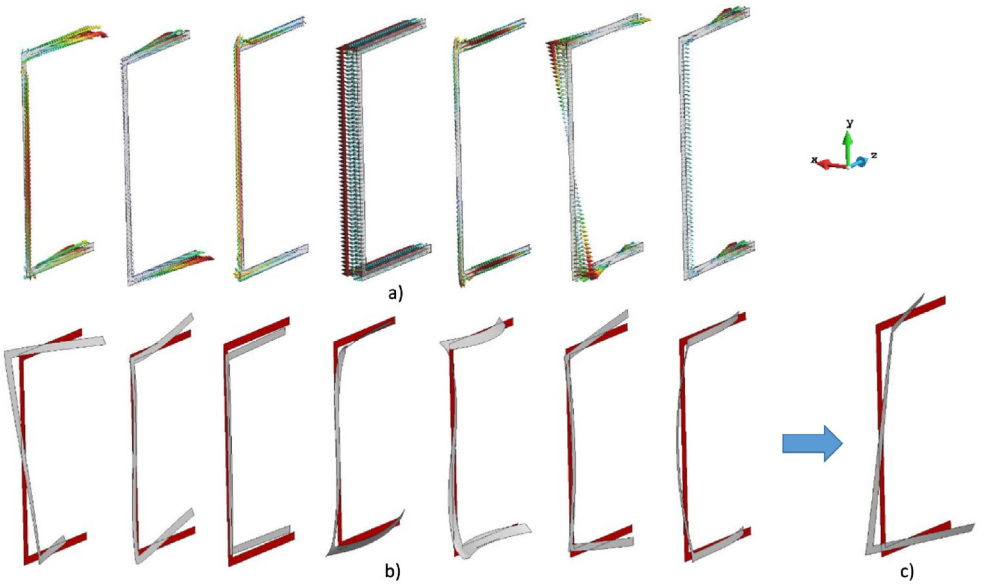

Fig. 13. (a) Interface force modes obtained from the self-equilibrated modes shown in Fig. 11a (through step 4 of Algorithm 3.) (b) Deformed shapes of the candidate fluctuation modes ($\widetilde{\boldsymbol{W}}$), obtained from the deformational modes displayed in Fig. 11b (through step 3 of Algorithm 3.). (c) Fluctuation mode ($\widetilde{\boldsymbol{V}}$) selected from the subspace spanned by the candidate fluctuation modes.

Table 8
U-shaped cross-section beam. Error measures defined in Eqs. (117) (ϵ^f, for the resultants and moment resultants) and (118) (ϵ^a, for the cross-section translations and rotations), for the 6 training tests with prescribed displacements plus the 2 tests with applied torque (labeled torque-1 and torque-2). The coarse-scale model is constructed using the same basis matrices for all slices — more specifically, the 8 modes of subdomain Ω^{50} determined from these training tests. The resulting coarse-scale element has 7 DOFs per node.

	Axial	Shear-y	Shear-z	Torsion	Bending-y	Bending z	Torque-1	Torque-2
Resultants (ϵ^f)	$0.34 \cdot 10^{-2}$	$0.19 \cdot 10^{-2}$	$1.05 \cdot 10^{-2}$	$0.01 \cdot 10^{-2}$	$1.17 \cdot 10^{-2}$	$0.19 \cdot 10^{-2}$	$7.24 \cdot 10^{-11}$	$5.08 \cdot 10^{-11}$
RB disp. (ϵ^a)	$1.67 \cdot 10^{-2}$	$0.50 \cdot 10^{-2}$	$0.36 \cdot 10^{-2}$	$0.06 \cdot 10^{-2}$	$0.6 \cdot 10^{-2}$	$1.0 \cdot 10^{-2}$	$0.46 \cdot 10^{-2}$	$0.66 \cdot 10^{-2}$

3), using a tolerance $\epsilon_f = 10^{-8}$ gives[20] the 7 force patterns shown in Fig. 13a. This means that there can be only $7 - 6 = 1$ fluctuation mode; this fluctuation mode is to be determined from within the subspace spanned by the candidate modes in Fig. 13b, see step 8 in Algorithm 3. The deformed shape of the mode resulting from this step is shown in Fig. 13c. The resulting coarse-scale element has, thus 7-DOFs per node, the 7th DOF being precisely the amplitude of this fluctuation mode. For completeness, we display in Eq. (123) the 7×7 block matrix $\boldsymbol{K}_{\mathbf{11}}^{*e}$ of the coarse-scale element derived from this kinematics:

$$\boldsymbol{K}_{\mathbf{11}}^{*e} = \widetilde{\boldsymbol{P}}_1^{e^T} \mathcal{K}^e \widetilde{\boldsymbol{P}}_1^e = 10^2 \begin{bmatrix} 103.25 & 0 & 0 & 0 & 0 & 0 & 0 \\ & 17.61 & 0 & -0.45 & 0 & 0.09 & -36.60 \\ & & 13.80 & 0 & 0.07 & 0 & 0 \\ & & & 0.096 & 0 & -0.0022 & -6.383 \\ & & & & 0.066 & 0 & 0 \\ & (\text{sym.}) & & & & 0.35 & -0.20 \\ & & & & & & 70676.1 \end{bmatrix}. \tag{123}$$

[20] Higher tolerances gives rise to 8 force patterns, and therefore, kinematics with 8 DOFs. However, we have found that the kinematics with 8 DOFs per node in tests with free ends tends to give higher errors. This may be due to an imbalance between the number of admissible configurations of the fictitious interfaces and the subdomain. Indeed, if we use 7 DOFs per node, the number of independent motions of the fictitious interfaces is equal to 7 + 7 = 14, which is the same number of possible independent configurations of the subdomain (6 rigid-body modes + 8 deformational modes). However, with 8 DOFs per node, there are more DOFs than possible configurations of the subdomain.

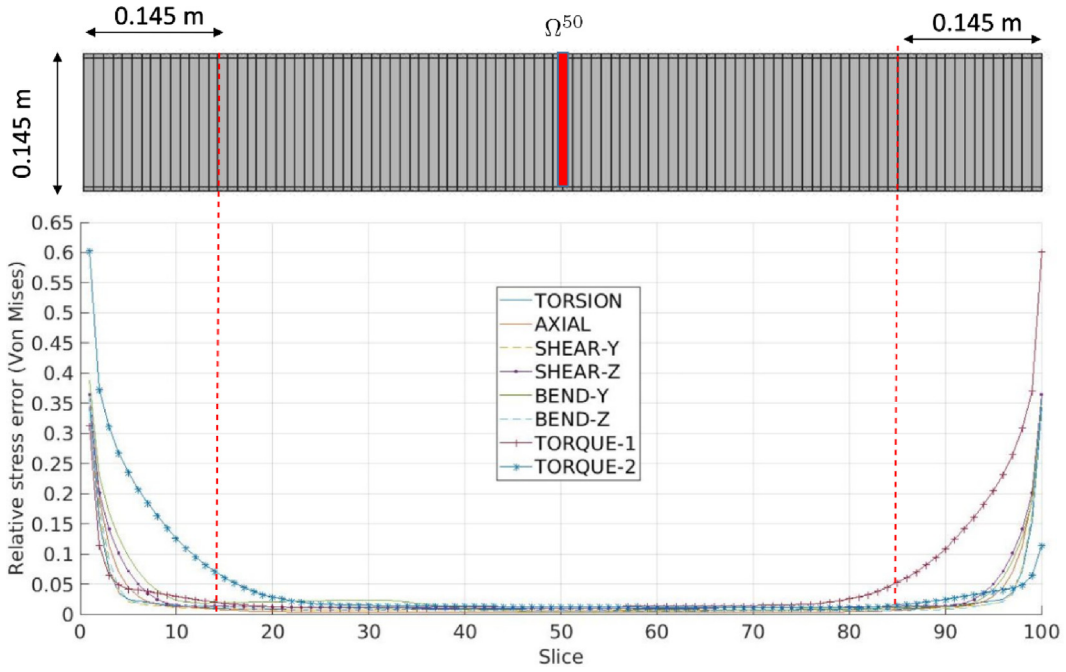

Fig. 14. U-shaped cross-section beam. Von Mises error measure (defined in Eq. (119)), for the 6 training tests with prescribed displacements plus the 2 tests with applied torque (labeled torque-1 and torque-2). The basis matrices of all subdomains are equal to the basis matrices obtained from the subdomain at the middle (subdomain Ω^{50}, highlighted in the top of the figure).

Remark 9.3. The reader familiar with the so-called Vlasov torsion theory for thin-walled cross-section beams (see e.g. Ref. [37], page 205) may notice the qualitatively resemblance between the fluctuation mode displayed in Fig. 13c — in which the flanges appear to rotate in opposite directions around the axis of the web — and the warping mode employed in such a theory. In the light of this resemblance, the 7th DOF in our coarse-scale element may be interpreted as a warping DOF; likewise, the 7th generalized internal force $\boldsymbol{F}^{*e}_{int\,i}(7)$ may be identified with the "bimoment" appearing in Vlasov theory.

Finally, to demonstrate that this new coarse-scale element with 7-DOFs per node is indeed representative of the beam behavior of this U-shaped cross-section prism, we present in Table 8 the error indicators given in Eqs. (117) and (118). Notice that now all values are below 1%. The increase of accuracy in the case of the torsion test with prescribed displacements is particularly noteworthy: from 7.33% and 10.2% when using the kinematics with 6 DOFs (see Table 7), to 0.01% and 0.06% with this new kinematics using 7 DOFs. A similar increase in quality is observed in terms of stresses, as can be appreciated in Fig. 14, where we plot the Von Mises stress error defined in Eq. (119) for the 8 training tests. At a distance from the ends equal to the height of the cross-section, the Von Mises error of the 6 tests with prescribed displacements is below 5%. The decay length in the case of the tests with prescribed forces is slightly higher (the error goes down to 5% at a distance equal to 120% the height of the cross-section).

9.3.3. Longer beam under self-weight

We move now to the assessment of the performance of the representative coarse-scale element derived in the foregoing in scenarios with different geometry (longer beam) and different external conditions. To this end, we construct a coarse-scale model of a U-shaped cross-section beam made up of 400 elements (4 m long) fixed on one end, and subjected to its own weight. Density is taking uniform and equal to $\rho = 2700$ Kg/m^3, and gravity is assumed to act along the y-axis. Since density is uniform, the vector of fine-scale nodal forces is expressible as $\boldsymbol{F}^e_{\boldsymbol{ext}} = -\boldsymbol{M}^e\,\widehat{\boldsymbol{\Phi}}^e_2 g\rho$, $g = 9.81$ m/s^2 being the acceleration of gravity, and $\widehat{\boldsymbol{\Phi}}^e_2$ the rigid body mode corresponding to translations in the direction of the y-axis (see (31)). Its coarse-scale counterpart $\boldsymbol{F}^{*e}_{\boldsymbol{ext}}$, on the other hand, is determined by Eq. Eq. (94). The work done by $\boldsymbol{F}^e_{\boldsymbol{ext}}$ over the deformational modes $\widetilde{\boldsymbol{\Phi}}^e$ ($\widetilde{\boldsymbol{\mathcal{F}}}^e_{ext}$ in Eq. Eq. (95)) vanishes by virtue of the orthogonality between rigid body and deformational modes (see Eq. (27)). This means

that $\boldsymbol{F}^{*e}_{\boldsymbol{ext}}$ only depends in this case on the resultant and moment resultant with respect to the centroid of each subdomain, which in this case is simply given by

$$\widehat{\boldsymbol{\mathcal{F}}}^{e}_{ext} = \widehat{\boldsymbol{\Phi}}^{e^T} \boldsymbol{F}^{e}_{\boldsymbol{ext}} = \begin{bmatrix} 0 & -\rho g V^e & 0 & 0 & 0 & 0 \end{bmatrix}^T, \tag{124}$$

$V^e = 1.475 \cdot 10^{-5}$ m^3 being the volume of the subdomain. Premultiplication of the above by the upscaling matrices $\widehat{\boldsymbol{P}}^{e^T}_1, \widehat{\boldsymbol{P}}^{e^T}_2 \in \mathbb{R}^{7\times 6}$ (defined in Eq. (84)) finally furnishes the desired generalized forces at the two nodes of our coarse-scale element:

$$\boldsymbol{F}^{*e}_{\boldsymbol{ext\,1}} = W^e \begin{bmatrix} 0 \\ -0.5 \\ 0 \\ 0 \\ 0 \\ 7.405 \cdot 10^{-4} \\ -0.6484 \end{bmatrix}; \qquad \boldsymbol{F}^{*e}_{\boldsymbol{ext\,2}} = W^e \begin{bmatrix} 0 \\ -0.5 \\ 0 \\ 0 \\ 0 \\ -7.405 \cdot 10^{-4} \\ +0.6484 \end{bmatrix} \tag{125}$$

(here $W^e = V^e \rho g$ is the weight of the subdomain). The equivalence between these two vectors and the fine-scale forces (self-weight) becomes apparent when inspecting the second entry of these vectors (forces in the y-direction) — they are half the weight of the subdomain. Likewise, the 6th entry represents the equivalent moment with respect to the z-axis caused by the weight with respect to the interface centroids; the obtained value ($7.405 \cdot 10^{-4} W^e$) is 11% lower than the value predicted by the standard Euler–Bernoulli beam formulation (which is $W L^e/12 = 8.33 \cdot 10^{-4} W$). The other nonzero entry is the 7th generalized force (the "bimoment" alluded to earlier). This bimoment is responsible of provoking twisting of the cross-section along the beam — the coupling follows from the fact that the (4, 7) entry of the stiffness matrix shown in Eq. (123) is nonzero.

The quality of the approximation afforded by this 7-DOFs coarse-scale element can be appreciated in Figs. 15c and 15d, where we show the (amplified) deformed shapes, along with the contour plot of the norm of nodal displacements, provided by the FE model and the HROM. Notice that the maximum displacement predicted by the coarse-scale HROM is only 0.122% below of that given by the "exact" FE analysis. The accuracy of the approximation can be further appreciated in Figs. 15a and 15b, where we plot the evolution along the beam of the nonzero generalized displacement and generalized forces, respectively, computed by the HROM, along with its FE counterparts. Observe that both sets of curves are practically indistinguishable (the average error in the case of displacements is 0.16%, and in the case of generalized forces, $7.5 \cdot 10^{-4}$ %).

9.3.4. Characteristic modes enriched with "local" modes

Next we address a case in which the ability of the proposed multiscale framework for capturing local effects in structures distinct from the training structures is showcased — provided of course that these local effects are present in any of the training scenarios. The structure to be studied is a U-shaped prismatic beam of length 2 m (200 subdomains) subjected to the same boundary conditions used in the training shear-y test (in which one end is fixed, and the other undergoes a translation in the direction of the y-axis, see Fig. 12b). The goal is to accurately determine the Von Mises stress distribution on the ends of the structure, with special emphasis on stress concentrations. The deformed shape and Von Mises stress contour plot computed by the FE model are shown in Fig. 16a, and the detailed view of the Von Mises stresses in the first subdomain (the one on the fixed end) in Fig. 16b.

As may be surmised, the characteristic 7-DOFs coarse-scale element described in Section 9.3.2 is not sufficient to achieve this goal — by construction, the corresponding basis matrices, hereafter denoted by $\widetilde{\boldsymbol{\Phi}}^{beam}$ and $\widetilde{\boldsymbol{\Psi}}^{beam}_{\mathbf{f}}$, do not contain information about any local effects. This is corroborated in Fig. 16e, where we plot the Von Mises error measure given in Eq. (119) obtained when this coarse-scale element is used for all the $M = 200$ subdomains (observe that the average error on the ends is around 35%); and in Fig. 16c, where we show the distribution of Von Mises stresses on the first subdomain (the coarse-scale model clearly fails to detect the stress concentrations at the corners).

Due to the local character of boundary effects, it is reasonable to assume that the deformational and force patterns adopted by the subdomains close to the ends are essentially the same as on the shear-y test with 100 subdomains (the one used for training). Accordingly, we can increase the quality of the approximation by *enriching* the characteristic deformational and force basis matrices of the subdomains close to the ends (here we have taken the 20 closest

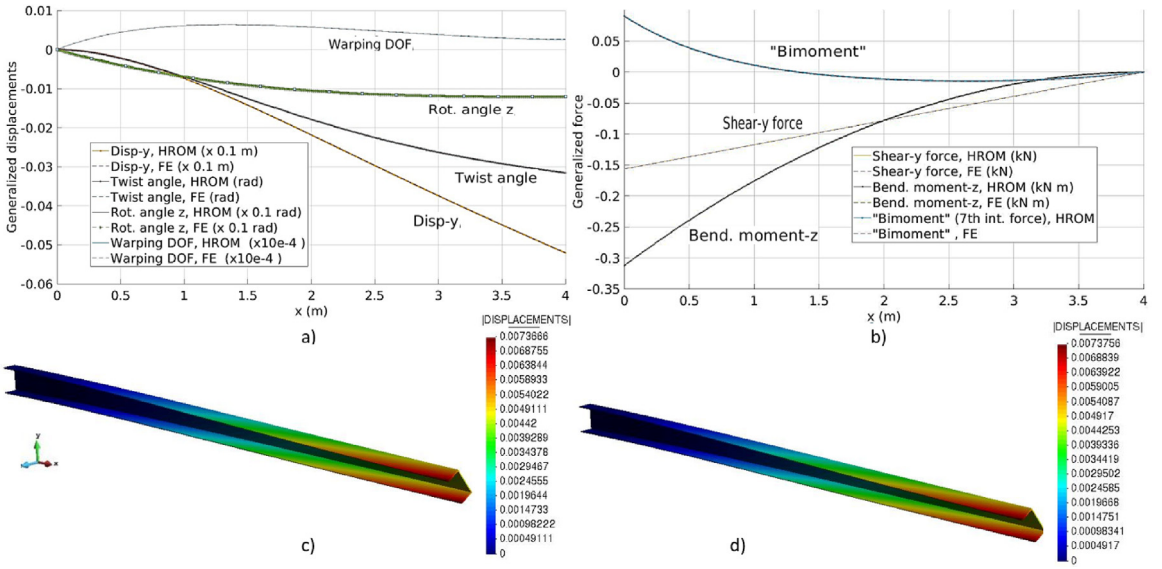

Fig. 15. 4 m long (400 subdomains) U-shaped cross-section beam fixed on one end and subject to its own weight. The coarse-scale HROM is constructed using the characteristic element of 7 DOFs per node described in Section 9.3.2. (a) Nonzero coarse-scale DOFs computed by the FE method and the HROM; more specifically, $\boldsymbol{a}_I(2)$ (translation of the interface centroid in the y-direction), $\boldsymbol{a}_I(4)$ (twist angle), $\boldsymbol{a}_I(6)$ (rotation angle around the z-axis); and $\boldsymbol{a}_I(7)$ (the "warping DOF", which is the amplitude of the mode shown in Fig. 13c.). (b) Nonzero generalized forces computed by the FE method and the HROM. (c) Deformed shape (amplified) and contour plot of the norm of nodal displacements computed by the FE method. (d) Deformed shape (amplified) and contour plot of the norm of nodal displacements computed by the HROM.

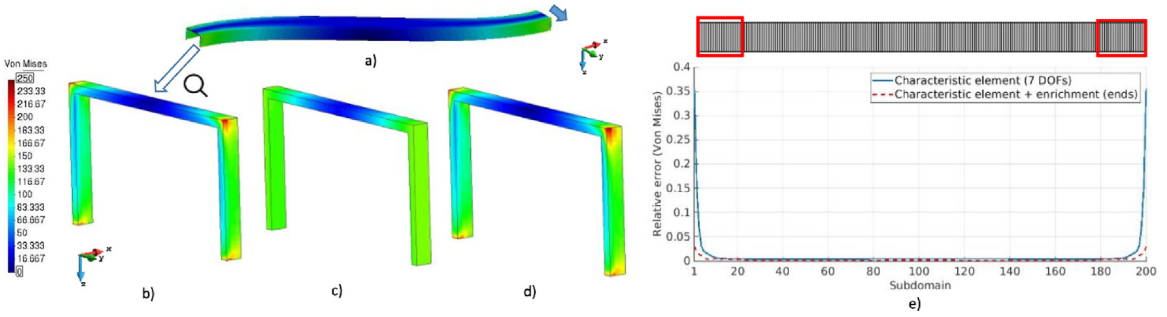

Fig. 16. U-shaped prismatic beam of length $l = 2$ m (200 subdomains), fixed on one end and with a prescribed translation of 0.01 m on the other end (in the direction of axis y). (a) Deformed shape ($\times$ 50) along with the contour plot of Von Mises stresses (MPa) computed by the FE model. (b) Detailed view of the Von Mises stresses on the first subdomain (in contact with the fixed end). (c) Same as in (b), but computed by a coarse-scale model that employs the characteristic element (8 deformational modes and 7 DOFs per node) determined in Section 9.3.2 (from a beam of length $l = 1$ m). (d) Same as in (b) and (c), but computed by an "enriched" coarse-scale model. (e) Von Mises error measure defined in Eq. (119) for all the $M = 200$ subdomains, for both coarse-scale models (without and with enrichment). The subdomains with enriched basis matrices are highlighted in the top of the Figure (subdomains 1 to 20, and 181 to 200).

domains to each end, as depicted at the top of Fig. 16e) with the snapshots coming from this very training test. The enrichment procedure goes as follows. For each Ω^e ($e \in \{1, 2 \dots 20, 181, 182 \dots 200\}$), construct snapshots matrices of the form $\boldsymbol{A}^e_{\boldsymbol{d}} = [\widetilde{\boldsymbol{\Phi}}^{beam}, \boldsymbol{d}^{e',sheary}]$ and $\boldsymbol{A}^e_{\boldsymbol{\lambda}} = [\widetilde{\boldsymbol{\Psi}}^{beam}_{\mathbf{f}}, \boldsymbol{\lambda}^{e',sheary}_{\mathbf{f}}]$, where $\boldsymbol{d}^{e',sheary}$ and $\boldsymbol{\lambda}^{e',sheary}_{\mathbf{f}}$ stand for the FE nodal displacement and interaction force nodal vectors at the domain $\Omega^{e'}$ in the training structure corresponding to Ω^e (for instance, for $e = 199$, we have $e' = 99$). Then apply the steps outlined in Section 5 for determining the deformational and interaction force basis for these 40 subdomains. As for the subdomains located on the central region, simply set $\widetilde{\boldsymbol{\Phi}}^e = \widetilde{\boldsymbol{\Phi}}^{beam}$ and $\widetilde{\boldsymbol{\Psi}}^e_{\mathbf{f}} = \widetilde{\boldsymbol{\Psi}}^{beam}_{\mathbf{f}}$ ($e \in \{21, 22 \dots 180\}$). The Von Mises error measure (see Eq. (119)) obtained when this enriched coarse-scale model is used is shown in Fig. 16e. Observe that the enrichment

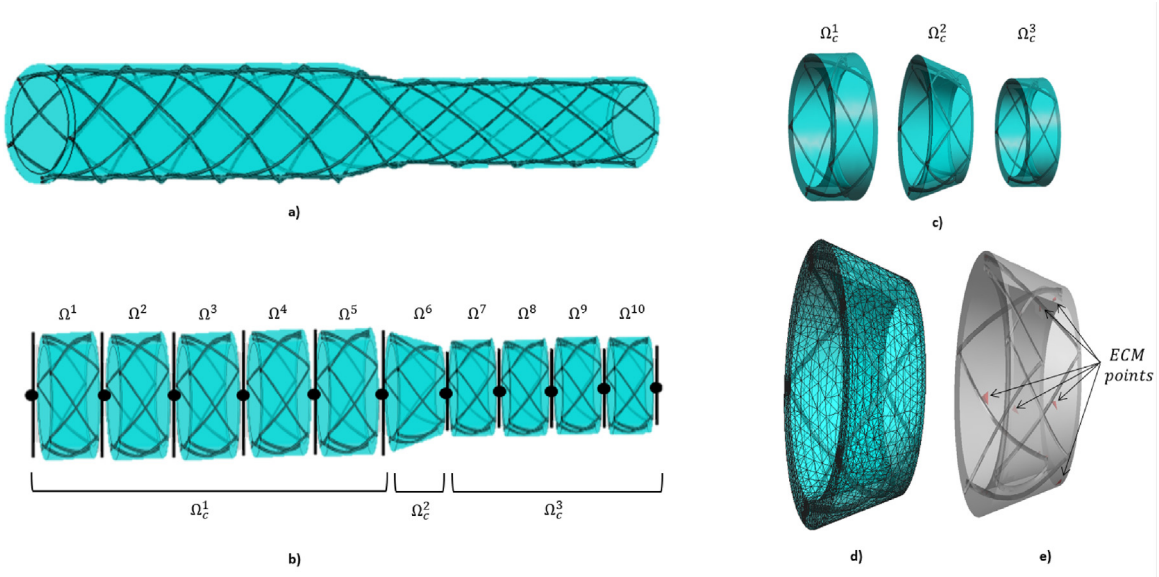

Fig. 17. (a) Fiber-reinforced tubular structure. (b) Domain partition into 10 slices. (c) Three different fiber-reinforced "characteristic" slices resulting from the domain decomposition. (d) FE mesh of subdomain Ω_c^2. (e) Elements highlighted in red contain the Gauss points selected by the ECM for subdomain Ω_c^2. (For interpretation of the references to color in this figure legend, the reader is referred to the web version of this article.)

has produced an error decrease from 35% to around 3% on the ends, while maintaining the same accuracy level on the central portion. The increase of quality on the first domain can be qualitatively appreciated by comparing the stress distributions computed by the FE and the enriched coarse-scale models (Figs. 16b and 16d, respectively); quantitatively, the maximum stress predicted by the FE analysis is 242.8 MPa, while the enriched coarse-scale model furnishes 248.0 MPa (only 2.14% above). In terms of computational cost, the number of unknowns in the coarse-scale model is approximately 450 times less than in the FE model ($8 \cdot 40 + 7 \cdot 160 = 1440$ DOFs in the 1D coarse-scale HROM against the $3 \cdot 214\,000 = 640\,000$ DOFs of the 3D FE analysis).

10. Cases with heterogeneous composition, cross-section changes and curvature

We conclude the numerical assessment of the proposed methodology by demonstrating its ability to deal with prismatic structures displaying several materials, abrupt changes of cross-section and/or curved midlines.

10.1. Fiber-reinforced tubular structure

In this section, we shall analyze the bending behavior, in the small strain regime, of a fiber-reinforced tubular structure (more specifically, a polymer-covered braided medical "stent", see e.g. [44]), by developing different HROMs with customized coarse-scale 1D FE. For this purpose, the domain depicted in Fig. 17a is decomposed into M=10 slices (see Fig. 17b), resulting in three geometrically different (or "characteristic") subdomains $\Omega_c^{e_g}$ ($e_g \in \{1, 2, 3\}$), as shown in Fig. 17c; their cross-section dimensions are described in Table 9. Each subdomain is composed by 10 interweaved fibers of diameter $d_f = 0.075$ mm, whose material is isotropic and behaves linearly, with Young Modulus $E_f = 80000$ MPa and Poisson's ratio $\nu_f = 0.33$; these fibers are embedded in an isotropic material with Young Modulus $E_m = 5$ MPa and Poisson's ratio $\nu_m = 0.4$. The FE discretization of each subdomain results in $n = 9601$ nodes and $m = 48292$ tetrahedral elements, as depicted in Fig. 17d for Ω_c^2.

Following the procedure described in Section 9, we are interested now in extracting a "characteristic" coarse-scale element for each distinct subdomain $\Omega_c^{e_g}$. Note that, in this case, due to the geometric difference between slices, the rigid body, deformational and force patterns will not be the same for distinct geometric configurations. In order

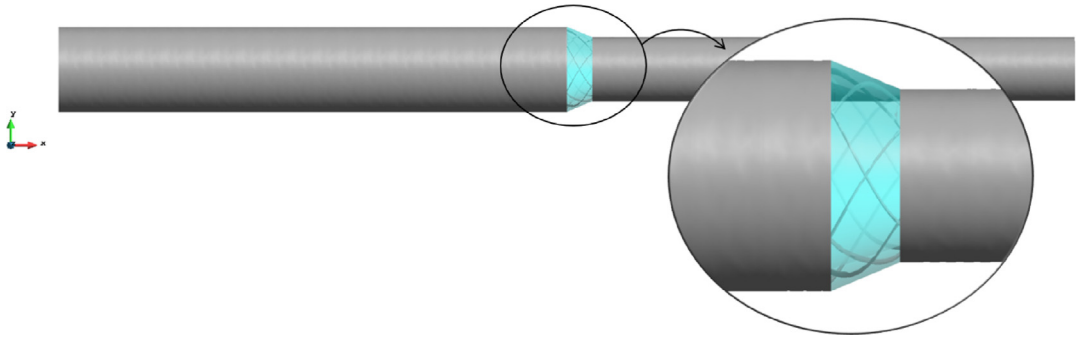

Fig. 18. Prismatic structure used for the training stage of the "characteristic" subdomain Ω_c^2.

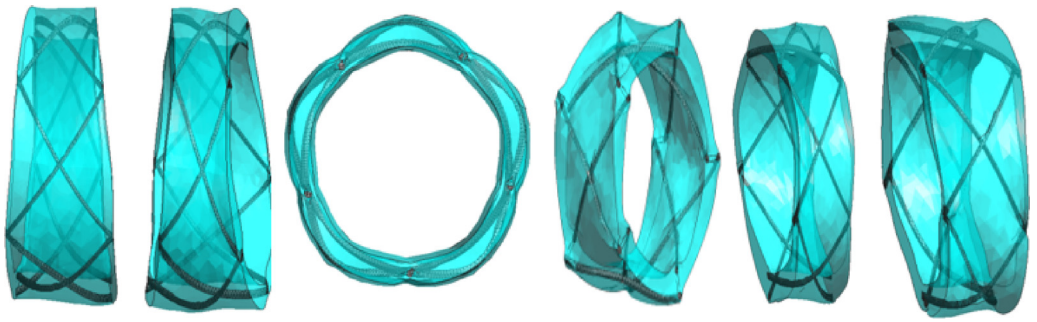

Fig. 19. Deformed shapes (amplified) of the characteristic deformational modes corresponding to Ω_c^1.

Table 9
Cross-section dimensions of the three fiber-reinforced tubular slices. d_{out}^m: minimum outer diameter, d_{out}^M: maximum outer diameter, t_{out}^m: minimum tubular thickness, t_{out}^M: maximum tubular thickness, and, l: slice length.

	d_{out}^m [mm]	d_{out}^M [mm]	t_{out}^m [mm]	t_{out}^M [mm]	l [mm]
Ω_c^1	2.625	2.625	0.25	0.25	0.785
Ω_c^2	1.970	2.625	0.1875	0.25	0.785
Ω_c^3	1.970	1.970	0.1875	0.1875	0.785

to exclude local effects induced by the imposition of boundary conditions, a prismatic structure composed of M=40 subdomains is built for each "characteristic" slice $\Omega_c^{e_g}$, and, separately for each case $e_g = 1, 2, 3$, we compute the deformational and interface force modes for the middle subdomain (Ω^{20}) in the 6 training tests described in Section 8.1, namely axial, shear-y, shear-z, torsion, bending-y and bending-z tests. Fig. 18 shows, for instance, the training structure designed for Ω_c^2. Moreover, Fig. 19 illustrates the deformed shapes of the characteristic deformational modes corresponding to Ω_c^1. To complete the description, in Fig. 17e we plot the elements which contain the set of Gauss points ($\boldsymbol{Z}^e$) selected by the ECM for subdomain Ω_c^2, as indicated in Section 7.5.

Note that, as stated in Section 9, since the information is extracted uniquely from subdomain Ω^{20}, the corresponding basis matrices, denoted by $\widetilde{\boldsymbol{\Phi}}^{e_g,beam}$ and $\widetilde{\boldsymbol{\Psi}}^{e_g,beam}$, do not contain information about any local effects. After completing the offline stage, we construct a coarse-scale model of each training structure assigning the corresponding modes to each "characteristic" element ($\Omega_c^{e_g}$), and evaluate the error comparing the HROM against the FE results. We found that the error does not exceed 5.5% in any case, which may allow us to claim that the employed deformational and interaction force modes are indeed "characteristic" of each subdomain configuration. Notice that, if one aims at improving the performance of this HROM, any of the strategies to enrich the basis matrices with additional information (see Section 9.3.2) can be followed.

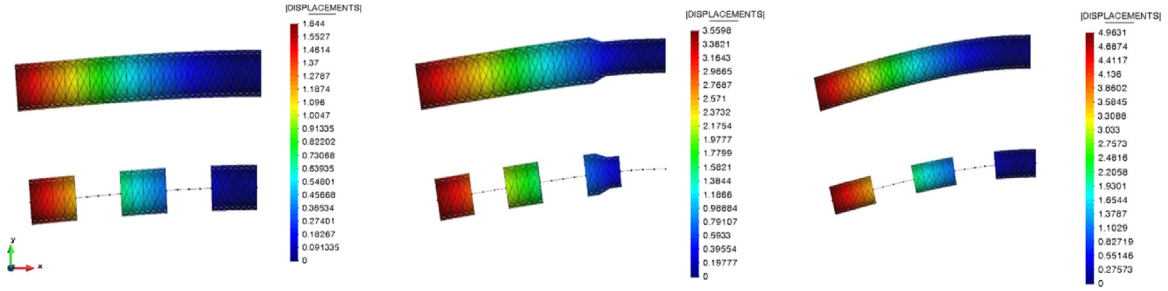

Fig. 20. Deform shape and norm of displacements computed by the FE method (top) and HROM (bottom) on three fiber-reinforced tubular structures. The right end is fixed, while the left end is prescribed with a force acting in the y-axis ($F_y = -0.01$ N).

Due to the versatility of our approach, the three "characteristic" coarse-scale elements derived in the foregoing can be used in scenarios with different geometries and different external conditions. Therefore, to assess the performance of the HROM in unseen scenarios, we construct three coarse-scale models of fiber-reinforced tubular structures, each of them made up of M=20 slices, as depicted in Fig. 20. The first beam is uniquely composed of 20 repetitions of subdomain Ω_c^1; the second one is composed by 14 repetitions of Ω_c^1, followed by 1 subdomain Ω_c^2, and then, 5 repetitions of Ω_c^3 at the right end; the third beam is composed by 20 repetitions of Ω_c^3. For each distinct subdomain, we use the corresponding basis matrices $\widetilde{\boldsymbol{\Phi}}^{e_g,beam}$ and $\widetilde{\boldsymbol{\Psi}}^{e_g,beam}$ ($e_g = 1, 2, 3$). We apply the same boundary conditions to all of them: the right end is fixed, while the left end is prescribed with a force acting in the y-axis ($F_y = -0.01$ N). The resulting deformed shapes given by both the FE method and HROMs are compared in Fig. 20, plotting the norm of the displacements on each case. In order to highlight the coarse-scale character of our HROM, we reconstruct the fine-scale results only in a few selected subdomains. Note that the reconstructed (fine-scale) displacements given by the HROM are in good agreement to the FE solutions, even given the fact that the training geometries were different, and they were not trained under external forces. It should be pointed out that, in this case, the number of DOFs is reduced from $M \cdot n \cdot 3 = 576\,060$ to $(M+1) \cdot 6 = 126$, yielding a notorious reduction factor[21] of 4571.

10.2. Helical structure with variable cross-section

Finally, we propose to build a coarse-scale model for the linear elastic behavior of a helix with circular cross-section. As shown in Fig. 21, the global domain is decomposed into M=600 subdomains, resulting in 10 "characteristic" slices $\Omega_c^{e_g}$ ($e_g = 1, 2, \ldots, 10$) with equal length $l = 10$ mm and varying cross-section diameter "d" (such that 40 mm $\leq d \leq$ 50 mm). The material is isotropic, with Young's Modulus $E = 70$ GPa and Poisson's ratio of $\nu = 0.3$. All subdomains are discretized using eight-nodes hexahedral elements, resulting in $m = 384$ elements and $n = 627$ nodes.

For each "characteristic" slice $\Omega_c^{e_g}$, we create a training geometry composed by a single subdomain $\Omega_c^{e_g}$ in the middle of a beam filled with straight segments at the ends, allowing us to neglect local effects. In Fig. 22, for instance, we show the training geometry designed for subdomain Ω_c^2. Separately for each case $e_g = 1, 2, \ldots, 10$, the snapshot matrices collect the results on the central slice $\Omega_c^{e_g}$ of the six training test described in Section 8.1. As outlined in Section 9, we now compute the deformational and interface force modes for each subdomain $\Omega_c^{e_g}$, which act as the "characteristic" modes of the coarse-scale elements in the HROM. Then we construct the coarse-scale counterpart of each training test and evaluate the results against those computed by the FE method. Similar to the previous case, the HROM/FE results show discrepancies below 5% in all the tests.

During the online stage, the derived coarse-scale elements are to be used to construct the HROM corresponding to the case shown in Fig. 21 with M=600 subdomains. Boundary conditions are imposed as follows: displacements

[21] In this particular case, the entire offline stage took 75 min in the computer at hand. However, as stated in the introduction, this cost is amply repaid by the low cost associated to the online stage, which is reduced from 12 min for the standard FE to 12 s for the HROM. Note that, we might now build many different coarse-scale models (changing the geometry or boundary confitions) and rapidly analyze them.

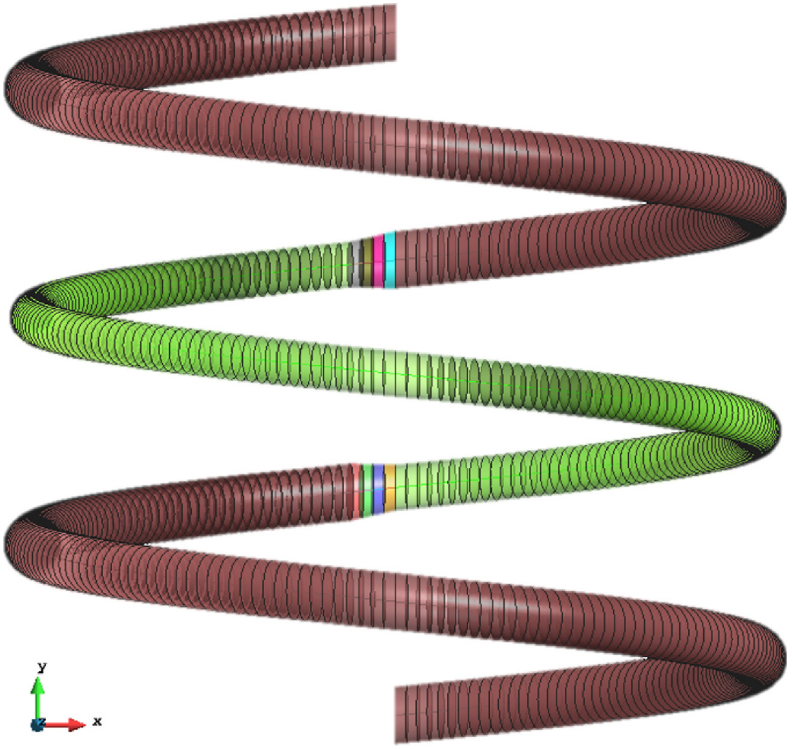

Fig. 21. Partitioning of helix into M=600 subdomains, resulting in ten "characteristic" slices $\Omega_c^{e_g}$ $(e_g = 1, 2, \ldots, 10)$ distinguished by distinct colors.

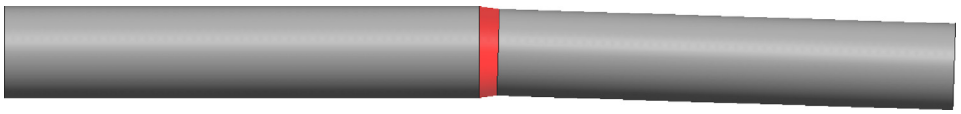

Fig. 22. Prismatic structure designed for running the six FE tests in the training stage for slice Ω_c^2.

in the x and z directions are prescribed at the top end of the beam ($\boldsymbol{a}_N(1) = 0.01$, $\boldsymbol{a}_N(3) = 0.01$), while the bottom end is fixed. Fig. 23 plots the Von Mises stress distributions obtained by both the FE method and the HROM, in which there are no discernible differences. Once again, aiming at highlight the coarse-scale character of our HROM, the fine-scale results are only reconstructed in selected subdomains. Notice that, by using the proposed approach, the high computational cost associated to the FE model can be largely reduced, decreasing in this case the number of DOFs from $M \cdot n \cdot 3 = 1\,128\,600$ to $(M + 1) \cdot 6 = 3606$ (reduction factor of 312).

11. Concluding remarks

- We have demonstrated that the partitioned variational framework originally put forward in Ref. [27] for periodic structures is generalizable to any prismatic structure, provided that each subdomain is allowed to

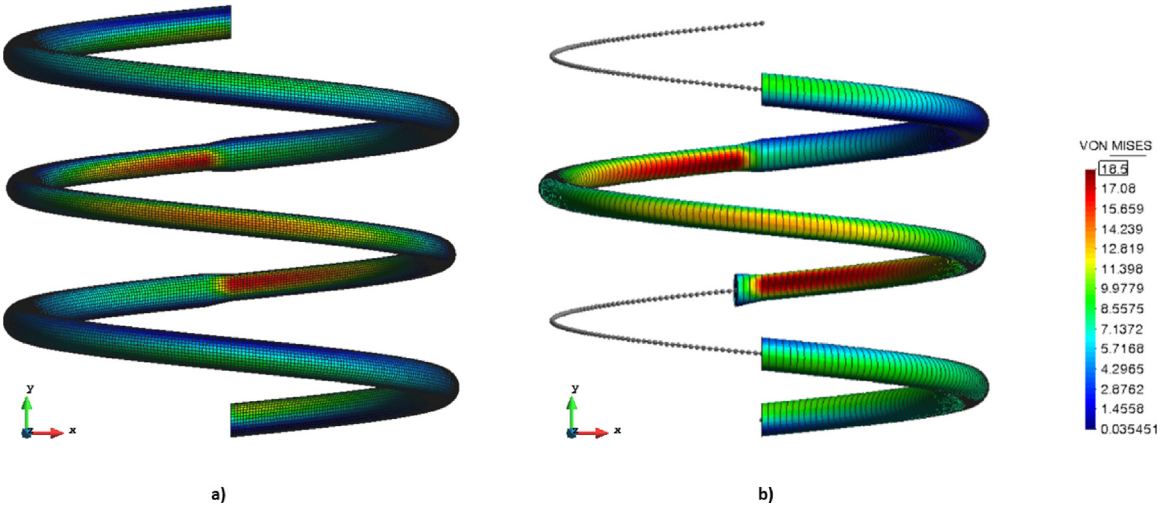

Fig. 23. Contour plot of Von Mises stress distributions computed by (a) the FE method and (b) the HROM. The results in the coarse-scale model were only reconstructed in a subset of selected subdomains.

have its own set of basis matrices, tailored to capture the displacement and stresses present in the FE results used for training the coarse-scale model.

- We have formalized the notion of "representative" or "characteristic" coarse-scale element (the equivalent of a 1D element in FE beam formulation) of a given 3D subdomain (see Section 9), by providing a rigorous definition in terms of its ability to transmit loads throughout the prismatic beam (Eqs. (117) and (118)), and a systematic "data-driven" procedure for determining the basis matrices required for constructing the coarse-scale model. Furthermore, with the aid of the interpolation procedure described in Appendix B, elements of different length, or other geometric variations, can be derived from an existing database without the need of running additional FE training analyses.
- Aside from the typical applications of standard FE beam elements, the proposed partitioned framework offers the possibility of modeling aspects which are outside the scope of such standard elements, namely: accurate representations of structures with abrupt changes in cross-section, for both straight (Section 10.1) and curved midlines (Section 10.2); local enrichment for capturing boundary effects (Section 9.3.4); even the possibility of recovering, almost exactly, the same 3D FE results used for training the model (Section 8).
- We have shown that it is possible to derive pre-computable downscaling (coarse-to-fine) operators for displacements (see Eq. (79) and Fig. 3); furthermore, the transpose of this downscaling matrices turn out to be the upscaling operators for nodal forces. In terms of computational implementation, the existence of such downscaling operators, along with the hyperreduction scheme based on the ECM for integration of internal forces (see Section 7.5), allow one to easily accommodate this type of element in existing 3D FE codes for solid elements. Consequently, the user need not worry about deriving "generalized" constitutive equations relating generalized forces and generalized strains (as in standard FE beam implementations), simply because there is no such a thing as generalized strains in our theory: rather, generalized forces are directly related with the Cauchy stresses at the ECM points (see Eq. (109)), and Cauchy stresses to infinitesimal strains through the pertinent standard 3D constitutive equations. Lastly, infinitesimal strains at the ECM points are connected to the coarse-scale DOFs (generalized displacements) by the "inter-scale" strain–displacements defined in Eq. (110) (which are actually the standard "B"-matrices of 3D solid elements multiplied by the aforementioned downscaling operator).
- Last but not least, we have seen in Section 8 that the method is not strictly consistent from the "machine learning" perspective, in the sense that, even if one does introduce any type of truncation in the modal representations of each subdomain, the fine-scale values recovered from the HROM do not coincide exactly with the fine-scale results used to train the model. Although the loss of accuracy is insignificant from the engineering point of view in most cases — stresses are exactly captured, the error lies in the representation of

rigid-body displacements —, it would be interesting in future research to delve deeper in this aspect, and try to develop an entirely consistent hyperreduced-order multiscale formulation. We have argued that the loss of information is due to the fact that incorporating all the fluctuation modes of the interface to ensure perfect compatibility leads to a coarse-scale problem with more unknowns than equations — that is why, for instance, we are forced to have 6 DOFs per node for the case of the rectangular cross-section, even though we know from the FE simulations that such interfaces do strain during the deformation. The challenge is to find complementary equations able to improve the accuracy without ruining the well-posedness of the coarse-scale equations. Research in this front is in progress and will be reported in forthcoming publications.

Declaration of competing interest

The authors declare that they have no known competing financial interests or personal relationships that could have appeared to influence the work reported in this paper.

Data availability

Data will be made available on request.

Acknowledgments

This work has received support from the Spanish Ministry of Economy and Competitiveness, through the "Severo Ochoa Programme for Centres of Excellence in R&D" (CEX2018-000797-S)". A. Giuliodori also gratefully acknowledges the support of "Secretaria d'Universitats i Recerca de la Generalitat de Catalunya i del Fons Social Europeu" through the FI grant (00939/2020), and J.A. Hernández the support of, on the one hand, the European High-Performance Computing Joint Undertaking (JU) under grant agreement No. 955558 (the JU receives, in turn, support from the European Union's Horizon 2020 research and innovation program and from Spain, Germany, France, Italy, Poland, Switzerland, Norway), and the European Union's Horizon 2020 research and innovation program under Grant Agreement No. 952966 (project FIBREGY).

Appendix A. Orthogonality conditions

Proposition A.1. *Let $\boldsymbol{U}, \boldsymbol{U}' : \Omega^e \to \mathbb{R}^3$ be two displacement fields of the form $\boldsymbol{U} = \boldsymbol{N}^e \boldsymbol{d}$ and $\boldsymbol{U}' = \boldsymbol{N}^e \boldsymbol{d}'$, where $\boldsymbol{N}^e : \Omega^e \to \mathbb{R}^{3\times 3n^e}$ is the matrix of global shape functions. Then,*

$$\langle \boldsymbol{U}, \boldsymbol{U}' \rangle = \int_{\Omega^e} \boldsymbol{U}^T \boldsymbol{U}' \, d\Omega = \boldsymbol{d}^T \boldsymbol{M}^e \boldsymbol{d}' \tag{A.1}$$

where $\boldsymbol{M}^e$ is the geometric mass matrix:

$$\boldsymbol{M}^e := \int_{\Omega^e} \boldsymbol{N}^{e^T} \boldsymbol{N}^e \, d\Omega \tag{A.2}$$

Proof. The proof follows easily from replacing the nodal interpolations $\boldsymbol{U} = \boldsymbol{N}^e \boldsymbol{d}$ and $\boldsymbol{U}' = \boldsymbol{N}^e \boldsymbol{d}'$ in the integral in Eq. (A.1). □

Proposition A.2. *Let $\boldsymbol{\lambda}_i, \boldsymbol{\lambda}_i' \in \mathbb{R}^{3l_i^e}$ be two nodal interaction forces at the interface boundary $\partial\Omega_i^e$. Suppose that the associated surface tractions $\boldsymbol{t}, \boldsymbol{t}' : \partial\Omega_i^e \to \mathbb{R}^3$ can be exactly represented in terms of their nodal values using the same interpolation functions as for the displacements. Then, it can be asserted that*

$$\langle \boldsymbol{t}, \boldsymbol{t}' \rangle = \int_{\partial\Omega_i^e} \boldsymbol{t}^T \boldsymbol{t}' \, d\Gamma = \boldsymbol{\lambda}_i^T \boldsymbol{M}_{f_i f_i}^{e^{-1}} \boldsymbol{\lambda}_i' \tag{A.3}$$

where

$$\boldsymbol{M}_{f_i f_i}^e := \int_{\partial\Omega_i^e} \boldsymbol{N}_{f_i}^{e^T} \boldsymbol{N}_{f_i}^e \, d\Gamma \tag{A.4}$$

(here $\boldsymbol{N}_{f_i}^e$ is the column block of $\boldsymbol{N}^e$ corresponding to the boundary DOFs $\boldsymbol{f}_i^e$).

Proof. The definition of the FE nodal forces in terms of their associated traction vectors reads

$$\boldsymbol{\lambda}_i = \int_{\partial\Omega_i^e} \boldsymbol{N}_{f_i}^{e^T}\, \boldsymbol{t}\; d\Gamma; \qquad \boldsymbol{\lambda}_i^{'} = \int_{\partial\Omega_i^e} \boldsymbol{N}_{f_i}^{e^T}\, \boldsymbol{t}'\; d\Gamma. \tag{A.5}$$

Since we are assuming that tractions are amenable to approximation by the FE shape functions, i.e.: $\boldsymbol{t} = \boldsymbol{N}_{f_i}^e \boldsymbol{T}$ and $\boldsymbol{t}' = \boldsymbol{N}_{f_i}^e \boldsymbol{T}'$, $\boldsymbol{T}, \boldsymbol{T}' \in \mathbb{R}^{3l_i^e}$ being the nodal values corresponding to $\boldsymbol{t}, \boldsymbol{t}'$, it follows from these expressions and Eq. (A.5) that

$$\boldsymbol{\lambda}_i = \left(\int_{\partial\Omega_i^e} \boldsymbol{N}_{f_i}^{e^T}\, \boldsymbol{N}_{f_i}^e\; d\Gamma\right) \boldsymbol{T} = \boldsymbol{M}_{\mathbf{f_i f_i}}^e \boldsymbol{T}; \qquad \boldsymbol{\lambda}_i^{'} = \left(\int_{\partial\Omega_i^e} \boldsymbol{N}_{f_i}^{e^T}\, \boldsymbol{N}_{f_i}^e\; d\Gamma\right) \boldsymbol{T}' = \boldsymbol{M}_{\mathbf{f_i f_i}}^e \boldsymbol{T}'. \tag{A.6}$$

Therefore,

$$\begin{aligned} \langle \boldsymbol{t}, \boldsymbol{t}' \rangle &= \int_{\partial\Omega_i^e} \boldsymbol{t}^T \boldsymbol{t}'\; d\Gamma = \boldsymbol{T}^T \boldsymbol{M}_{\mathbf{f_i f_i}}^e \boldsymbol{T}' = \left(\boldsymbol{M}_{\mathbf{f_i f_i}}^{e^{-1}} \boldsymbol{\lambda}_i\right)^T \boldsymbol{M}_{\mathbf{f_i f_i}}^e \boldsymbol{M}_{\mathbf{f_i f_i}}^{e^{-1}} \boldsymbol{\lambda}_i^{'} \\ &= \boldsymbol{\lambda}_i^{'T} \boldsymbol{M}_{\mathbf{f_i f_i}}^{e^{-1}} \boldsymbol{\lambda}_i^{'} \end{aligned} \tag{A.7}$$

as stated. □

Appendix B. Interpolation of subdomain modes

The methodology presented in Section 9 for determining "characteristic" coarse-scale elements requires, in principle, specific FE training tests for each geometrically distinct subdomain. In some cases, it may be possible to concoct training structures in which several subdomains are processed at the same time, as illustrated in Fig. B.24a, thereby partially alleviating the computational burden associated to the corresponding 3D FE analyses.

However, even if such saving measures are adopted, the offline stage may still prove overly costly for routine structural analyses. This shortcoming is specially evident when we consider geometric variations such as the width of the subdomains in straight prismatic beams. Indeed, suppose we have determined the deformational basis matrix[22] $\widetilde{\boldsymbol{\Phi}}(l_0) \in \mathbb{R}^{3n\times p}$ of a representative coarse-scale element of width l_0. With this coarse-scale element at our disposal, we can model any prismatic beam of length $L = nl_0$ where n is some integer $n > 1$. However, if L is not a multiple of l_0, such that $L = nl_0 + l$, where $n > 1$ is an integer and $l_0 < l < 2l_0$, then the modeling of the prismatic beam would entail, in principle, an additional training campaign for determining the basis matrices of a subdomain of width equal to l. As may be surmised, repeating this operation for any possible value of l is simply impractical, and may render the proposed approach unattractive if compared with standard beam finite elements — which, after all, although demonstrably less accurate, do not require complicated 3D FE analyses to infer their shape functions.

Fortunately, as we argue in what follows, there is no need to perform a battery of FE analyses each time one is confronted with a subdomain whose geometry does not coincide exactly with any of the geometries existing in the offline database. The key ingredient to avoid such analyses is to perform a special type of *interpolation* among the pre-computed basis matrices. To illustrate this idea, we shall use the example mentioned above involving the width of the subdomains, more specifically the case of the rectangular cross-section prismatic, discussed in Section 9.2, where $l_0 = 0.01$ m. We take this value as the reference width, and then parameterize the coordinates of the mesh nodes of the subdomain as $x(\alpha) = (1+\alpha)X$, $y = Y$ and $z = Z$, where $\alpha = 1 - l/l_0$, and $0 \leq \alpha \leq 1$. Then we determine the characteristic deformational basis matrix $\widetilde{\boldsymbol{\Phi}}(\alpha_i)$ for m values of the dimensionless parameter α: $0 = \alpha_1 < \alpha_2 < \ldots < \alpha_{m-1} < \alpha_m = 1$. This can be done by either performing 6 FE analyses for each of the m samples separately, or by performing one single set of 6 tests with the configuration shown in Fig. B.24a. Empirically, we find[23] that all the matrices have the same number of columns as the reference one (i.e. 6 modes): $\widetilde{\boldsymbol{\Phi}}(\alpha_i) \in \mathbb{R}^{3n\times 6}$.

Now suppose we wish to determine the deformational matrix $\widetilde{\boldsymbol{\Phi}}(\alpha^*)$ for a width parameter $\alpha^* \neq \alpha_i$. This problem falls into the category of the so-called *manifold interpolation problems* (see e.g. Ref. [45], Chapter 7). The reason this problem is dubbed so is because the pre-computed basis matrices $\{\widetilde{\boldsymbol{\Phi}}(\alpha_i)\}_{i=1}^m$ pertain to a manifold, namely, the manifold of subspaces of dimension $p = 6$ of $\mathbb{R}^{3n}$ (formally, a *Grassmann* manifold). The interpolated matrix

[22] The same applies for the self-equilibrated basis matrix $\widetilde{\boldsymbol{\Psi}}_{\mathbf{f}}$, as well as the stress basis matrix, $\boldsymbol{\Theta}$.

[23] This may be explained by the fact that the variation of width (from 0.01 m to 0.02 m) is small in comparison with the transversal dimensions of the subdomains ($h = 0.1$ m).

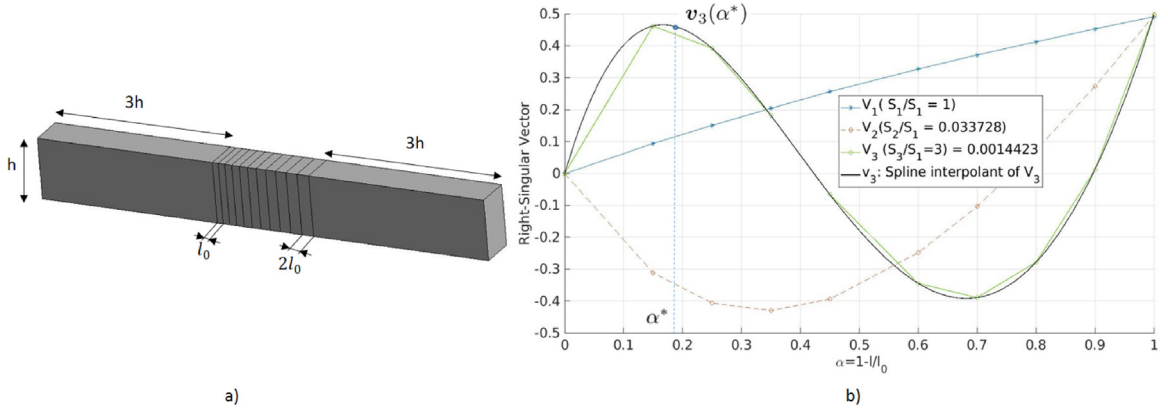

Fig. B.24. (a) "Training" structure containing subdomains, in its central portion, whose width ranges from l_0 to $2l_0$ ($l_0 = 0.01$ m). The two remaining subdomains (of width $3h$, h being the height of the cross-section) need not be processed — they act as "dummy" structures, in the sense that they only serve for keeping the studied subdomains sufficiently away from the ends so that their stress states are not significantly disturbed by local effects. (b) First three right-singular vectors ($\boldsymbol{V}_j$, j=1,2,3), computed in Step 2 of Box B.1, versus the width parameter α, for the case of $m = 11$ samples. In the case of $\boldsymbol{V}_3$, we show its spline interpolant $\boldsymbol{v}_3$. Given a new input parameter α^*, we evaluate $\boldsymbol{v}_j(\alpha^*)$, and then determine the interpolated matrix (reshaped as column vector) on the tangent space via Step 3 in Box B.1.

Algorithm 4: Logarithmic map on a Grassmann manifold (from Ref. [46])

1 **Function** $\boldsymbol{H}$ =GLog($\boldsymbol{X}, \boldsymbol{Y}$):
  Data: $\boldsymbol{X}, \boldsymbol{Y} \in \mathbb{R}^{n\times p}$, where $n \geq p$, $\boldsymbol{X}^T\boldsymbol{X} = \boldsymbol{Y}^T\boldsymbol{Y} = \boldsymbol{I}_{p\times p}$.
  Result: $\boldsymbol{H} \in \mathbb{R}^{n\times p}$ (the image of $\boldsymbol{Y}$ on the tangent space of the manifold at point $\boldsymbol{X}$).
2 $[\boldsymbol{U}, \boldsymbol{S}, \boldsymbol{V}] \leftarrow$ SVD$((\boldsymbol{Y} - \boldsymbol{X}(\boldsymbol{X}^T\boldsymbol{Y}))(\boldsymbol{X}^T\boldsymbol{Y})^{-1}, 0)$ // Here $\boldsymbol{S} \in \mathbb{R}^p$ is the vector of singular values
3 $\boldsymbol{\theta} \leftarrow$ atan($\boldsymbol{S}$)
4 $\boldsymbol{H} \leftarrow \boldsymbol{U}$diag$(\boldsymbol{\theta})\boldsymbol{V}^T$ // diag($\boldsymbol{\theta}$) is a diagonal matrix containing $\boldsymbol{\theta} \in \mathbb{R}^p$

must preserve this very property, i.e., it must have $p = 6$ linearly independent columns as well. The procedure (described in detail in Box B.1 [46]) for ensuring this is to map $\{\widetilde{\boldsymbol{\Phi}}(\alpha_i)\}_{i=1}^m$ from the manifold onto its *tangent space* at a reference point (we take here $\widetilde{\boldsymbol{\Phi}}(\alpha_1)$), perform the interpolation in such tangent space, and finally map the interpolated matrix back to the manifold (in differential geometry, the mappings that go from the manifold to the tangent space and viceversa are known as the *logarithmic* mapping and *exponential* mapping, respectively). It should be noticed that this procedural steps are similar to the ones advocated in Ref. [31], the only difference being that we employ here an SVD-based spline interpolant scheme (steps 2,3 and 4), rather than the entry-wise Lagrangian interpolant suggested in Ref. [31]. The idea of using this SVD-based interpolation scheme, in turn, is borrowed from Ref. [47]; its performance is illustrated in Fig. B.24b.

To assess the accuracy of this interpolation, we determine the basis matrices for $n = 21$ distinct widths, and then use a subset with m matrices ($2 < m < n - 1$) of such matrices for constructing the spline interpolants — and the remaining $q = n - m$ matrices for examining the error. Rather than measuring the interpolation error per se, which is of little interest from a practical point of view, we perform interpolation on the self-equilibrated modes $\widetilde{\boldsymbol{\Psi}}_{\mathbf{f}}$ as well, and then compute the coarse-scale stiffness matrix $\boldsymbol{K}^*(\alpha_i)$ via expression (103). For batches sizes $m = 2, 4, 8, 16$, the relative Frobenius error (between "exact and interpolated matrices) yields: 0.06% ($m = 2$), $3.5\cdot10^{-4}$ % ($m = 4$), $4.72 \cdot 10^{-5}$ % ($m = 8$) and $6.89 \cdot 10^{-6}$ % ($m = 16$). Note that with just two sets of basis matrices (obtained from subdomains of width l_0 and $2l_0$), the error (0.06%) is less than the error inherent to the use of characteristic elements (see Table 5). This suggests that, in principle, training with just two subdomains of length l_0 and $2l_0$ may suffice to deliver reasonably approximate stiffness values for any subdomain of length $l_0 \leq l \leq 2l_0$. Nevertheless, this conclusion may not be generalizable to other more complex cross-sections, and thus, it is better to carry out an error assessment like the one presented in the foregoing using, at least, 6 different widths.

Given the deformational basis matrices $\{\widetilde{\boldsymbol{\Phi}}(\alpha_i)\}_{i=1}^m$ ($\widetilde{\boldsymbol{\Phi}}(\alpha_i) \in \mathbb{R}^{3n\times p}$) of subdomains of width $l_i = (1+\alpha_i)l_0$, $0 = \alpha_1 < \alpha_2 \ldots < \alpha_{m-1} < \alpha_m < 1$, find $\widetilde{\boldsymbol{\Phi}}(\alpha^*)$ for a given $\alpha^* \neq \alpha_i$ by interpolation on the tangent space of the Grassmann manifold of p-dimensional subspaces of $\mathbb{R}^{3n}$, taking as reference point $\widetilde{\boldsymbol{\Phi}}(\alpha_1)$.

- **Pre-computation of spline interpolants** (just once for the given basis matrices $\{\widetilde{\boldsymbol{\Phi}}(\alpha_i)\}_{i=1}^m$)

  1) For all $i = 1, 2 \ldots m$, orthogonalize $\widetilde{\boldsymbol{\Phi}}(\alpha_i)$ in the Euclidean norm via the SVD: $[\boldsymbol{X}_i, \bullet, \bullet] = \mathrm{SVD}(\widetilde{\boldsymbol{\Phi}}(\alpha_i), 0)$. Then map each $\boldsymbol{X}_i$ onto the tangent space at $\boldsymbol{X}_1$ via Algorithm 4:

  $$\boldsymbol{H}_i = \mathrm{GLog}(\boldsymbol{X}_1, \boldsymbol{X}_i), \qquad i = 1, 2, 3 \ldots m. \tag{B.1}$$

  2) Reshape each $\boldsymbol{H}_i \in \mathbb{R}^{3n\times p}$ into a column vector $\boldsymbol{g}_i \in \mathbb{R}^{3n\cdot p}$ ($i = 1, 2 \ldots m$), and store the vectors in a matrix $\boldsymbol{G} = [\boldsymbol{g}_1, \boldsymbol{g}_2 \ldots \boldsymbol{g}_m]$. Then apply the SVD on $\boldsymbol{G}$:

  $$[\boldsymbol{U}, \boldsymbol{S}, \boldsymbol{V}] = \mathrm{SVD}(\boldsymbol{G}, 0). \tag{B.2}$$

  3) Construct spline interpolants (i.e., piecewise cubic polynomials) for each column $\boldsymbol{V}_j \in \mathbb{R}^m$ of the right-singular matrix $\boldsymbol{V} = [\boldsymbol{V}_1, \boldsymbol{V}_2 \ldots \boldsymbol{V}_m]$:

  $$\boldsymbol{v}_j = \mathrm{spline}(\boldsymbol{\alpha}, \boldsymbol{V}_j), \qquad j = 1, 2 \ldots m \tag{B.3}$$

  where $\boldsymbol{\alpha} = [\alpha_1, \alpha_2 \ldots \alpha_m]$.

- **Determination of basis matrix** $\widetilde{\boldsymbol{\Phi}}(\alpha^*)$

  4) Using the piecewise cubic polynomials $\boldsymbol{v}_j$ ($j = 1, 2 \ldots m$), determine the column vector $\boldsymbol{g}(a^*)$ corresponding to the point in the tangent space associated to α^*:

  $$\boldsymbol{g}(\alpha^*) = \sum_{j=1}^{m} \boldsymbol{U}_j S_j \boldsymbol{v}_j(\alpha^*). \tag{B.4}$$

  5) Reshape $\boldsymbol{g}(\alpha^*) \in \mathbb{R}^{3np}$ into a matrix $\boldsymbol{H}^* \in \mathbb{R}^{3n\times p}$, and then map $\boldsymbol{H}^*$ back to the manifold via Algorithm 5:

  $$\boldsymbol{X}^* = \mathrm{GExp}(\boldsymbol{X}_1, \boldsymbol{H}^*). \tag{B.5}$$

  6) Finally, apply operator (33) to $\boldsymbol{X}^*$ to convert it into a purely deformational mode for this geometric configuration. Then, use the weighted SVD (see Algorithm 1) to make it M-orthogonal; the resulting matrix will be the desired $\widetilde{\boldsymbol{\Phi}}(a^*)$.

Box B.1: Computation of characteristic deformational modes via manifold interpolation.

Algorithm 5: Exponential map on a Grassmann manifold (from Ref. [46])

Function $\boldsymbol{Y}$ =GExp($\boldsymbol{X}$, $\boldsymbol{H}$):
  Data: $\boldsymbol{X} \in \mathbb{R}^{n\times p}$, where $n \geq p$, $\boldsymbol{X}^T\boldsymbol{X} = \boldsymbol{I}_{p\times p}$; $\boldsymbol{H} \in \mathbb{R}^{n\times p}$ (point on the tangent space of the manifold at $\boldsymbol{X}$).
  Result: $\boldsymbol{Y} \in \mathbb{R}^{n\times p}$, where $\boldsymbol{Y}^T\boldsymbol{Y} = \boldsymbol{I}$ (the image of $\boldsymbol{H}$ on the manifold).
  $[\boldsymbol{U}, \boldsymbol{S}, \boldsymbol{V}] \leftarrow$ SVD($\boldsymbol{H}$,0)
  $\boldsymbol{Y} \leftarrow \boldsymbol{X}\boldsymbol{V}$ diag(cos($\boldsymbol{S}$)) + $\boldsymbol{U}$ diag(sin($\boldsymbol{S}$))

References

[1] P. Benner, S. Gugercin, K. Willcox, A survey of projection-based model reduction methods for parametric dynamical systems, SIAM Rev. 57 (4) (2015) 483–531.

[2] M. Loeve, Probability Theory, Courier Dover Publications, 2017.

[3] K. Fukunaga, Introduction to Statistical Pattern Recognition, Elsevier, 2013.

[4] D. Amsallem, C. Farhat, An online method for interpolating linear parametric reduced-order models, SIAM J. Sci. Comput. 33 (5) (2011) 2169–2198.
[5] M. Balajewicz, D. Amsallem, C. Farhat, Projection-based model reduction for contact problems, Internat. J. Numer. Methods Engrg. 106 (8) (2016) 644–663.
[6] A. Buhr, L. Iapichino, M. Ohlberger, S. Rave, F. Schindler, K. Smetana, Localized model reduction for parameterized problems, in: Model Order Reduction, Vol. 2, 2020, pp. 245–306.
[7] T.F. Chan, T.P. Mathew, Domain decomposition algorithms, Acta Numer. 3 (1994) 61–143.
[8] L. Hamandi, R. Lee, F. Ozguner, Review of domain-decomposition methods for the implementation of FEM on massively parallel computers, IEEE Antennas Propag. Mag. 37 (1) (1995) 93–98.
[9] W.C. Hurty, J.D. Collins, G.C. Hart, Dynamic analysis of large structures by modal synthesis techniques, Comput. Struct. 1 (4) (1971) 535–563.
[10] R.R. Craig Jr., M.C. Bampton, Coupling of substructures for dynamic analyses, AIAA J. 6 (7) (1968) 1313–1319.
[11] P. Kerfriden, J.C. Passieux, S.P.A. Bordas, Local/global model order reduction strategy for the simulation of quasi-brittle fracture, Internat. J. Numer. Methods Engrg. 89 (2) (2012) 154–179.
[12] J.L. Eftang, A.T. Patera, A port-reduced static condensation reduced basis element method for large component-synthesized structures: approximation and a posteriori error estimation, Adv. Model. Simul. Eng. Sci. 1 (1) (2014) 1–49.
[13] A. Radermacher, S. Reese, Model reduction in elastoplasticity: proper orthogonal decomposition combined with adaptive sub-structuring, Comput. Mech. 54 (3) (2014) 677–687.
[14] D.B.P. Huynh, D.J. Knezevic, A.T. Patera, A static condensation reduced basis element method: approximation and a posteriori error estimation, ESAIM Math. Model. Numer. Anal. 47 (1) (2013) 213–251.
[15] L. Zhou, J.W. Simon, S. Reese, Proper orthogonal decomposition for substructures in nonlinear finite element analysis: coupling by means of tied contact, Arch. Appl. Mech. 88 (11) (2018) 1975–2001.
[16] Y. Maday, E.M. Rønquist, A reduced-basis element method, J. Sci. Comput. 17 (1) (2002) 447–459.
[17] L. Iapichino, A. Quarteroni, G. Rozza, Reduced basis method and domain decomposition for elliptic problems in networks and complex parametrized geometries, Comput. Math. Appl. 71 (1) (2016) 408–430.
[18] J. Baiges, R. Codina, S. Idelsohn, A domain decomposition strategy for reduced order models. Application to the incompressible Navier–Stokes equations, Comput. Methods Appl. Mech. Engrg. 267 (2013) 23–42.
[19] J.A. Hernández, J. Oliver, A. Huespe, M. Caicedo, J. Cante, High-performance model reduction techniques in computational multiscale homogenization, Comput. Methods Appl. Mech. Engrg. 276 (2014) 149–189.
[20] L. Xia, P. Breitkopf, A reduced multiscale model for nonlinear structural topology optimization, Comput. Methods Appl. Mech. Engrg. 280 (2014) 117–134.
[21] J. Yvonnet, Q. He, The reduced model multiscale method (R3M) for the non-linear homogenization of hyperelastic media at finite strains, J. Comput. Phys. 223 (1) (2007) 341–368.
[22] N. Nguyen, A multiscale reduced-basis method for parametrized elliptic partial differential equations with multiple scales, J. Comput. Phys. 227 (23) (2008) 9807–9822.
[23] F. Albrecht, B. Haasdonk, S. Kaulmann, M. Ohlberger, The localized reduced basis multiscale method, in: Proceedings of ALGORITMY, 2012, pp. 9–14.
[24] S. Kaulmann, M. Ohlberger, B. Haasdonk, A new local reduced basis discontinuous Galerkin approach for heterogeneous multiscale problems, C. R. Math. 349 (23–24) (2011) 1233–1238.
[25] A. Abdulle, Y. Bai, Reduced basis finite element heterogeneous multiscale method for high-order discretizations of elliptic homogenization problems, J. Comput. Phys. 231 (21) (2012) 7014–7036.
[26] Y. Efendiev, J. Galvis, T.Y. Hou, Generalized multiscale finite element methods (GMsFEM), J. Comput. Phys. 251 (2013) 116–135.
[27] J.A. Hernández, A multiscale method for periodic structures using domain decomposition and ECM-hyperreduction, Comput. Methods Appl. Mech. Engrg. 368 (2020) 113192.
[28] K. Park, C.A. Felippa, A variational principle for the formulation of partitioned structural systems, Internat. J. Numer. Methods Engrg. 47 (1–3) (2000) 395–418.
[29] K. Park, Y.H. Park, Partitioned component mode synthesis via a flexibility approach, AIAA J. 42 (6) (2004) 1236–1245.
[30] J.A. Hernández, M.A. Caicedo, A. Ferrer, Dimensional hyper-reduction of nonlinear finite element models via empirical cubature, Comput. Methods Appl. Mech. Engrg. 313 (2017) 687–722.
[31] D. Amsallem, C. Farhat, Interpolation method for adapting reduced-order models and application to aeroelasticity, AIAA J. Am. Inst. Aeronaut. Astronaut. 46 (7) (2008) 1803–1813.
[32] R. Schardt, Generalized beam theory—an adequate method for coupled stability problems, Thin-Walled Struct. 19 (2–4) (1994) 161–180.
[33] K. Park, C.A. Felippa, A variational framework for solution method developments in structural mechanics, J. Appl. Mech. 65 (1) (1998) 242–249.
[34] G.H. Golub, C.F. Van Loan, Matrix Computations, Vol.3, JHU Press, 2012.
[35] S. Chaturantabut, D. Sorensen, Discrete empirical interpolation for nonlinear model reduction, in: Decision and Control, 2009 Held Jointly with the 2009 28th Chinese Control Conference. CDC/CCC 2009. Proceedings of the 48th IEEE Conference on, IEEE, 2010, pp. 4316–4321.
[36] M. Yano, A.T. Patera, An LP empirical quadrature procedure for reduced basis treatment of parametrized nonlinear PDEs, Comput. Methods Appl. Mech. Engrg. 344 (2019) 1104–1123.
[37] E. Oñate, Structural Analysis with the Finite Element Method. Linear Statics: Volume 2: Beams, Plates and Shells, Springer Science & Business Media, 2013.

[38] K. Carlberg, C. Bou-Mosleh, C. Farhat, Efficient non-linear model reduction via a least-squares Petrov–Galerkin projection and compressive tensor approximations, Internat. J. Numer. Methods Engrg. 86 (2) (2011) 155–181.
[39] R.A. Toupin, Saint–Venant's principle, Arch. Ration. Mech. Anal. 18 (2) (1965) 83–96.
[40] C.A. Felippa, The amusing history of shear flexible beam elements, Iacm Expr. 17 (5) (2005) 13–17.
[41] J.S. Przemieniecki, Theory of Matrix Structural Analysis, Courier Corporation, 1985.
[42] P. Roger Brockenbrough, F.S. Merritt, et al., Structural Steel Designer's Handbook, McGraw-Hill Education, 2011.
[43] J. Freund, A. Karakoc, Shear and torsion correction factors of Timoshenko beam model for generic cross sections, Res. Eng. Struct. Mater 2 (2016) 19–27.
[44] A. Giuliodori, J.A. Hernández, D. Fernandez-Sanchez, I. Galve, E. Soudah, Numerical modeling of bare and polymer-covered braided stents using torsional and tensile springs connectors, J. Biomech. 123 (2021) 110459.
[45] P. Benner, S. Grivet-Talocia, A. Quarteroni, G. Rozza, W. Schilders, L.M. Silveira, Model Order Reduction, Volume 1: System-And Data-Driven Methods and Algorithms, De Gruyter, 2021.
[46] E. Begelfor, M. Werman, Affine invariance revisited, in: 2006 IEEE Computer Society Conference on Computer Vision and Pattern Recognition, Vol. 2, CVPR'06, IEEE, 2006, pp. 2087–2094.
[47] A.E. Long, C.A. Long, Surface approximation and interpolation via matrix SVD, College Math. J. 32 (1) (2001) 20–25.